ATOMISTIC MODELING OF THE CHARGE PROCESS AND OPTIMIZATION OF CATALYSTS POSITIONING IN POROUS CATHODES OF LITHIUM/AIR BATTERIES

Vom Fachbereich Produktionstechnik

der

UNIVERSITÄT BREMEN

zur Erlangung des Grades
Doktor-Ingenieur
genehmigte

Dissertation

von

Dipl. Phys. Tatjana Dabrowski

Gutachter: Prof. Dr.-Ing. Matthias Busse

Prof. Dr. Michael Moseler, Albert-Ludwigs-Universität Freiburg

Tag der mündlichen Prüfung: 08. April 2016

Zusammenfassung

Die Reversibilität und die Kapazität der Lithium/Luft Akkumulatoren sind derzeit auf Grund des hohen Überpotentials zwischen dem Lade- und dem Entladevorgang und auf Grund des Verschlusses der porösen Struktur der aktiven Kathodenoberfläche durch die ungleichförmige Ablagerung des Entladeproduktes Li_2O_2 enorm limitiert. In der vorliegenden Arbeit analysieren wir diese kapazitätslimitierenden Probleme des Lithium/Luft Akkumulators in zwei separaten Teilen.

Im ersten Teil dieser Arbeit stellen wir eine kombinierte Methode aus klassischer und auf der Dichtefunktionaltheorie basierender, molekulardynamischer Analyse zur Untersuchung der zugrunde liegenden Sauerstoffentstehungsreaktion während des Ladevorgangs des Lithium/Luft Akkumulators vor. Als Modell des Li_2O_2 Materials an der Kathode verwenden wir kleine amorphe Cluster mit einer 2:2 Li:O Stöchiometrie, deren stabilste atomare Konfiguration sowohl O Atome als auch $O-O$ Paare mit gemischtem Peroxid/Superoxid-Charakter beinhalten. Dies wurde mit Hilfe ihrer Bindungslängen, Ladungen, Spinmomenten und Zustandsdichten aufgezeigt. Die Oxidation der Li_8O_8 Cluster wird in einer auf der Dichtefunktionaltheorie basierenden Molekulardynamik-Simulation über das Entfernen von einem bzw. zwei Elektronen untersucht. Dies erfolgt sowohl in Vakuum als auch in der Umgebung von Dimethylsulfoxid-Lösungsmittelmolekülen mit einer zuvor in einer klassischen Molekulardynamik-Simulation optimierten Struktur. Während das Entfernen von einem Elektron die Erhöhung des Superoxid-Charakters der $O-O$ Bindungen zur Folge hat, führt das Entfernen von zwei Elektronen zu einer spontanen Abscheidung von entweder eines O_2- oder eines LiO_2^+-Moleküls. Diese Resultate werden hinsichtlich eines zwei-Stufen-Prozesses interpretiert, in dem bei geringen Oxidationspotentialen ein Peroxid-zu-Superoxid-Übergang in amorphen Li_2O_2 Phasen stattfinden kann, gefolgt von einer Abscheidung von molekularem Sauerstoff und Li^+ Ionen bei höheren Potentialen.

Im zweiten Teil lösen wir numerisch eine Reaktions-Diffusionsgleichung zur Bestimmung des Li_2O_2-Ablagerungsprofils in porösen Modellkathoden in An- und Abwesenheit diskreter aktiver Katalysatoren unter Betrachtung von vier häufig verwendeten Elektrolyten. Wir implementieren einen *Greedy* Optimierungsalgorithmus zur Maximierung der Kathodenkapaziät vor dem Verschluss der Poren durch die optimale Positionierung diskreter Katalysatoren entlang der Pore. Die

Ergebnisse deuten darauf hin, dass die maximale Kapazität in Abwesenheit von Katalysatoren durch die Sauerstofflöslichkeit und -diffusivität limitiert ist und stark in den vier betrachteten Lösungsmitteln variiert. Die optimale Katalysatorverteilung kann diese Unterschiede jedoch effektiv kompensieren und einen sinnvollen Weg zur Konstruktion einer Kathodenstruktur mit einer hohen Leistungsfähigkeit entsprechend der benötigten Einsatzbedingungen aufzeigen.

Abstract

The reversibility and capacity of current lithium/air cells are severely limited by the high overpotential between the charge and discharge process and the occlusion of the pores of the active cathode surface due to non-uniform deposition of Li_2O_2 as the discharge product. In this thesis we present a study of these capacity-limiting issues on the lithium/air battery in two parts.

First we present a combined classical and density functional theory based molecular dynamics study of the mechanisms underlying the oxygen evolution reaction during the charging of lithium/air batteries. As models for the Li_2O_2 material at the cathode we employ small amorphous clusters with a 2:2 Li:O stoichiometry, whose energetically most stable atomic configurations comprise both O atoms and $O-O$ pairs with mixed peroxide/superoxide character, as revealed by their bond lengths, charges, spin moments, and densities of states. The oxidation of Li_8O_8 clusters is studied in unbiased density functional theory based molecular dynamics simulations upon removal of either one or two electrons, either in vacuo or immersed in dimethyl sulfoxide solvent molecules with a structure previously optimized by means of classical molecular dynamics. Whereas removal of one electron leads only to an enhancement of the superoxide character of $O-O$ bonds, removal of two electrons leads to the spontaneous dissolution of either an O_2 or a LiO_2^+ molecule. These results are interpreted in terms of a two-stage process in which a peroxide-to-superoxide transition can take place in amorphous Li_2O_2 phases at low oxidation potentials, later followed by the dissolution of dioxygen molecules and Li^+ ions at higher potentials.

In the second part we solve numerically a reaction-diffusion equation to determine the Li_2O_2 deposition profiles in a model porous cathode in the absence and presence of discrete catalytic sites, considering four commonly used electrolytes. We implement a Greedy optimization algorithm to maximize the cathode capacity before pore clogging by optimal positioning of the discrete catalysts along the pore. The results indicate that a maximal capacity is limited by the oxygen solubility and diffusivity in each electrolyte in the absence of catalysts and vary widely in the four cases considered. However, optimal catalyst distributions can effectively compensate for these differences, suggesting a rational way of designing cathode structures with high performances according to the required operation conditions.

Contents

List of Figures

List of Tables

Motivation

The energy transition and the consequent requirement for renewable and environmentally friendly alternatives to fossil fuels as well as the increasing demand for portable electronic devices motivates the investigation of efficient, cost-effective, and safe secondary batteries. Advanced energy storage devices are required for instance to provide intermediate energy storage between renewable but unsteady energy sources and end users, or to improve the distance range and thus the public acceptance of electric vehicles. The lithium/air battery is a promising candidate in this context, since its theoretical energy/mass (specific energy) and energy/volume (energy density) ratios are considerably higher than those of currently used lithium-ion batteries. A comparison of the increased driving range due to the high specific energy of lithium/air batteries in comparison to state-of-the-art and future Li-ion batteries is shown in Figure 1.1 (a). However, a number of critical issues have to be overcome before commercially viable lithium/air batteries can be realized.

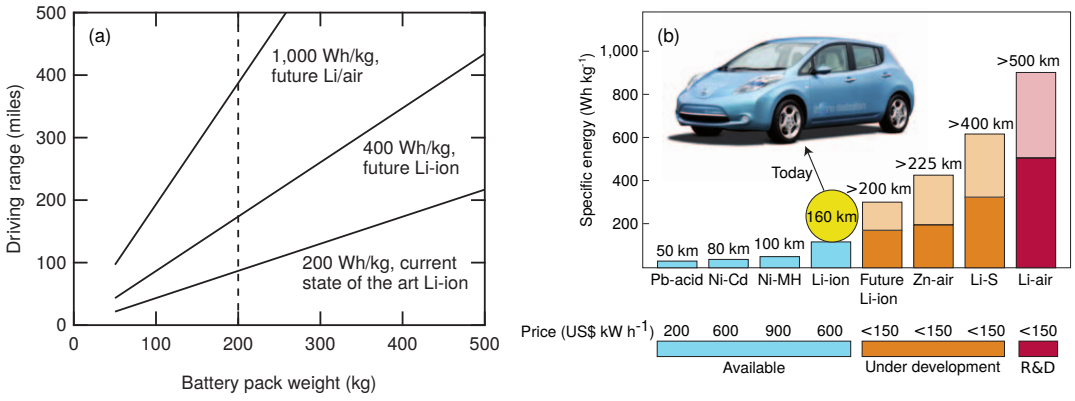

Figure 1.1.: (a) Driving range for the state-of-the-art Li-ion, future Li-ion, and Li/air battery with respect to the battery weight,[1] and (b) comparison of specific energies for different battery types.[2]

The basic reacting species in the lithium/air battery are lithium (Li) and molecular dioxygen (O_2). Li provides the highest electrode potential relative to the standard hydrogen electrode, which makes the light metal the strongest reducing agent. A combination with an also strong, non-toxic, and easily available oxidizing agent such as O_2 is the reason for the high specific energy and hence the attractiveness of the Li/air battery. Although other attempts are under consideration, such as Na/O_2 and Li/S batteries, both provide own challenging issues. While Na/O_2 cells show a lack of safety due to the high reactivity of sodium with air humidity, Li/S cells offer only a low capacity (electric charge that can be delivered) due to the insulating character of sulfur as well as fast capacity fading due to the solubility of polysulfide intermediates. Simultaneously, the theoretical specific energy for both battery types remains far below the expectations for Li/air batteries.[2,3]

Li/air cells based on non-aqueous electrolytes and lithium peroxide as the discharge product present a 4 times higher specific energy and 2 times higher energy density than lithium-ion batteries if the active materials alone are considered. If a whole practical cell is considered, still their specific energy as well as their capacity are more than twice as much as ion-based alternatives, provided an open-system battery, i. e., oxygen is assumed not to be stored on board in the charged state. A comparison of the specific energies for different state-of-the-art battery types as well as future concepts are shown in Figure 1.1 (b). Nonetheless, we should keep in mind that theoretical calculations of the specific energy, energy density, and capacity even for an estimated practical cell are only an upper limit and won't be achieved in a real working cell.

The setup and the mode of operation are in principle the same for all concepts of Li/air batteries. During the discharge process the metallic Li anode is oxidized releasing electrons into the external conductor, while the resulting lithium ions, Li^+, are dissolved in the electrolyte and transported to the cathode. On the porous, conducting cathode molecular dioxygen enters the cell and is reduced on the cathode surface receiving electrons from the external conductor. Both then react to form a discharge product depending on the applied electrolyte. During the charge process the reverse process takes place, releasing O_2 from the cell and Li^+ into the electrolyte, which form again the metallic lithium anode receiving an electron form the external conductor.

Two general types of Li/air batteries are distinguished based on aqueous or non-aqueous electrolytes. A standard overall reaction of the aqueous Li/air battery in a basic environment is given by[4]

$$4Li + 6H_2O + O_2 \rightleftarrows 4(LiOH \cdot H_2O) \ .$$

At different pH values the discharge product strongly depends on the electrolyte environment.[1] The aqueous Li/air battery provides the advantage that the discharge product of lithium salts is dissolved in the electrolyte, and hence pore clogging of the porous cathode is inhibited (see below).

However, the high chemical reactivity of alkali metals with water requires a reliable protection layer between the metallic lithium and the electrolyte, the so-called Solid Electrolyte Interface (SEI), which decreases the Li^+-conductivity significantly.[4] On the other hand, SEIs form naturally in most of the non-aqueous electrolytes, such that less attention has to be payed to the issue of anode protection for initial studies.[5] Nonetheless, a chemically and physically stable, Li^+-conductive, and flexible SEI that can deal with the high volume changes during the charge/discharge cycle of a Li/air battery is a challenging issue also in the case of non-aqueous electrolytes.[6] Since attempts to fabricate aqueous Li/air batteries have resulted in much lower specific energies, most of the literature concerning Li/air batteries as well as the present work focus on non-aqueous electrolytes. A detailed comparison of specific energies, energy densities, and capacities for aqueous and non-aqueous Li/air and Li-ion batteries as well as an assumption for practical cells can be found in ref. 1.

The overall reaction in non-aqueous Li/air batteries is given by

$$2Li + O_2 \rightleftarrows Li_2O_2 \ .$$

The oxygen reduction reaction during the discharge process is assumed to be a multi-step process starting with the oxidation of O_2 on the cathode surface. This is followed by the formation of lithium superoxide LiO_2 from Li^+ and the superoxide ion O_2^-. Finally, the superoxide is further reduced chemically and electrochemically to form lithium peroxide Li_2O_2 on the cathode surface.[7–9] In summary, the oxygen reduction reactions (ORR) are proposed as

$$\begin{aligned} O_2 + e^- &\longrightarrow O_2^- \\ O_2^- + Li^+ &\longrightarrow LiO_2 \\ 2LiO_2 \longrightarrow Li_2O_2 + O_2 \quad \text{and/or} \quad LiO_2 + Li^+ + e^- &\longrightarrow Li_2O_2 \ . \end{aligned} \tag{1.1}$$

The oxygen evolution reaction (OER) has been suggested to be a direct two-electron decomposition process according to[7–9]

$$Li_2O_2 \longrightarrow 2Li^+ + 2e^- + O_2 \ . \tag{1.2}$$

However, the complexity of the charge process via a multi-step process that strongly depends on the morphology of the electrochemically grown Li_2O_2 on discharge has been revealed only recently.[10–15]

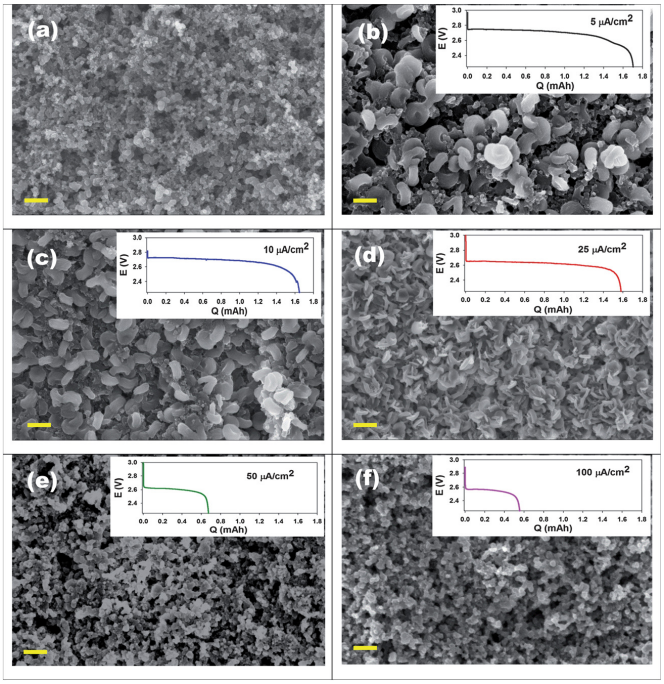

Figure 1.2.: FESEM images of the cathode (a) before and after discharge for current densities of (b) 5 mA cm^{-2}, (c) 10 mA cm^{-2}, (d) 25 mA cm^{-2},(e) 50 mA cm^{-2}, and (f) 100 mA cm^{-2}; scaling bar: 400 nm.[16]

The enormous influence of the operating conditions of the battery on the Li_2O_2 morphology of the discharge product can be seen in Figure 1.2 for a cathode discharged at different current densities, as investigated by Adams et al.[16] via Field Emission Scanning Electron Microscopy (FESEM). Starting from a pure porous carbon cathode in Figure 1.2 (a), the growth mechanism proceeds in the form of small (toroidal) particles at low current densities in Figure 1.2 (b) which decrease in size for increasing current densities to form an amorphous thin Li_2O_2 film on the carbon surface (Figure 1.2 (c)-(f)). The growth mechanism of the ORR, the corresponding morphology, and its impact on the OER process are discussed in detail in Part I, Chapter 2 of the thesis.

Understanding of the reaction mechanism on charge and discharge is crucial to enable a truly reversible process and to clarify the origin of the high overpotential between the ORR and the OER of more than 1 V[17] (see charge/discharge profile for the growth and decomposition of toroidal Li_2O_2 particles in Figure 1.3 (a)). The high overpotential indicates a high cell impedance as well as possible different chemical reactions on charge and discharge. The increasing impedance has been referred to the insulating character of Li_2O_2[18] and its effect of passivating the cathode surface.[10,19,20] However, the impact of vacancies and dopants as well as metallic Li_2O_2 surfaces[21] on conductivity have not been considered in the above studies. Furthermore, the mechanism and the morphology of electrochemically grown Li_2O_2 forming toroidal particles which contain bulk structures but also conductive shells, amorphous Li_2O_2 films,[16] and superoxide species[11–13] are not well understood and still the subject of ongoing studies. A Raman spectrum of a discharged cathode in Figure 1.3 (b) shows the composition of electrochemically grown discharge product in comparison to commercial Li_2O_2. A peak at the LiO_2 band confirms the existence of superoxide

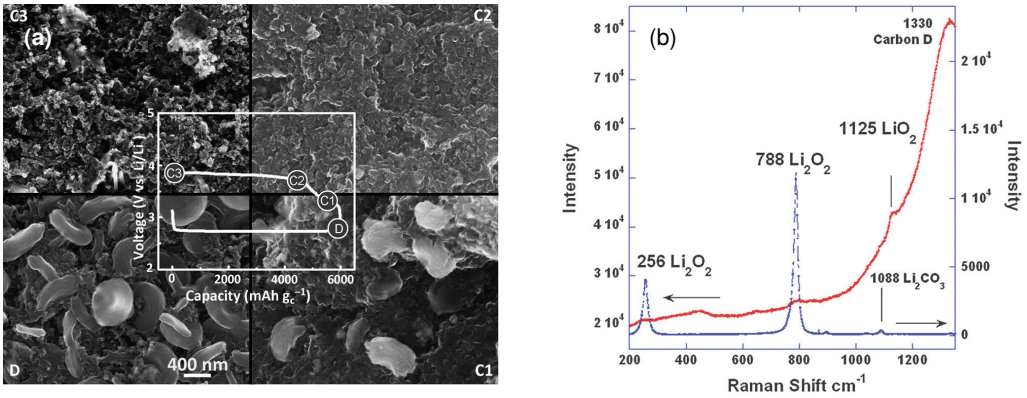

Figure 1.3.: (a) Charge/discharge profile of a Ketjen black cathode with corresponding SEM images at the indicated points[15], and (b) Raman spectra of a discharged carbon cathode (red) from the electrolyte/cathode separator side and commercial Li_2O_2 (blue).[14]

species in the peroxide, while the weak Li_2O_2 peak indicates only a small proportion of crystalline lithium peroxide. Their impact has to be clarified before passivation of Li_2O_2 can be assumed to be the only dominant effect.

Another potential reason for the poor reversibility and high impedance is the critical role of electrolyte stability. Many attempts to develop suitable non-aqueous electrolytes have been done, in order to gain the desired properties of electrochemical stability, high Li^+-conductivity, as well as a good oxygen solubility and diffusivity. Starting from carbonate-based solvents that have been shown to decompose during the discharge process,[23–27] newer attempts focus on ether-based electrolytes and sulfoxides.[15,28–33] The decomposition of carbonates and the improved stability of ethers have been shown by McCloskey et al.[22] in an analysis of electron consumption per oxygen during the charge process via a differential electrochemical mass spectrometry (DEMS) coupled with isotopic labeling of oxygen. As can be seen in Figure 1.4, carbonate-based electrolytes as well as mixtures consume more than $2e^-/O_2$, indicating parasitic side reactions equivalent to solvent degradation.

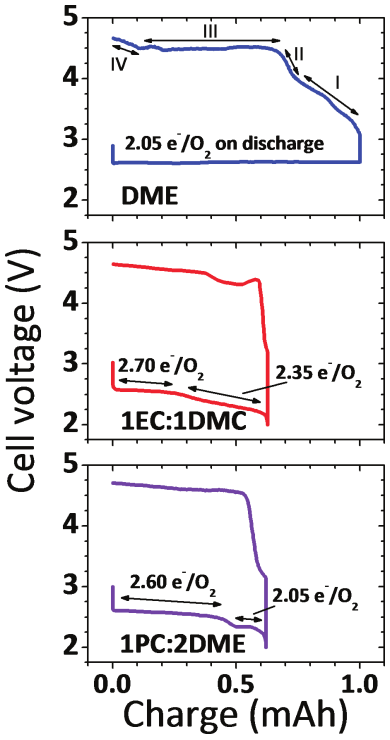

Figure 1.4.: Electron per oxygen consumption for the solvents 1,2-dimethoxyethane (DME), ethylene carbonate (EC) and dimethyl carbonate (DMC).[22]

Another category of feasible electrolytes is represented by ionic liquids (low temperature liquid salts). Analyzing ionic liquids as potential electrolytes, the project group for Electrical

Energy Storage from the Fraunhofer IFAM * could not find an advantage over the currently used dimethyl sulfoxide $(CH_3)_2SO$ (DMSO) and observed a good performance only in the case of mixtures of ionic liquids and DMSO. Reasons for this are supposed in the formation of complexes between Li^+ and the anions of the ionic liquid.

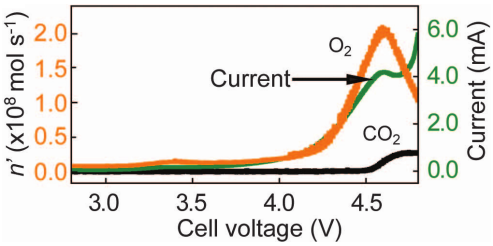

Figure 1.5.: DEMS during the charge process of a DMSO-based electrolyte, where n' is the gas generation rate.[33]

Thus far, none of the proposed solvents has shown a sufficient long-term and high-potential stability. Even the promising sulfoxides show degradation at high potentials evolving CO_2 in addition to O_2 (Figure 1.5)[33] and decompose in presence of superoxide species upon long terms.[34] Again the importance of understanding the exact reaction mechanism becomes clear, involving all intermediates to identify the reasons for decomposition processes of the applied solvent. The resulting solvent decomposition product lithium carbonate, Li_2CO_3, is also a candidate for passivation effects of the cathode and pore clogging of its porous structure due to its insolubility and insulating character. The permeability of the highly porous cathode has to be ensured to guarantee a sufficient oxygen supply ideally from ambient air. Since storage of the required oxygen in a tank on board decreases the specific energy of the Li/air battery back to the level of ion-based battery types,[1] an oxygen supply from ambient air is essential. However, the search for a flexible gas-selective membrane is quite challenging but inevitable to prevent electrolyte evaporation and contamination with air humidity, carbon dioxide, and nitrogen, which cause side reactions that yield the formation of Li_2CO_3 and gases such as H_2 and NH_3.

Apart from the purpose of a sufficient oxygen supply from outside the cell, the porous structure has to ensure oxygen transport into the cell. Furthermore, the cathode provides a storage for the discharge product as well as the active surface area for the ORR. Two main capacity-limiting factors occur due to requirements set by the porosity. A sufficiently large surface area at constant volume demands a highly porous structure (narrow pores) which results in a fast clogging of the pore entrances by discharge product. An exemplary SEM image of the highly porous structure (Super P carbon black on Ni-foam with MnO_2 catalysts) is shown in Figure 1.6 (a). The inefficient utilization of the pore volume and the low yield of discharge product result in an enormous capacity loss of the battery.[14,35] Furthermore, low oxygen solubilities and diffusivities of the applied non-aqueous electrolytes cause an oxygen concentration drop from the oxygen supplying side into the interior regions of the cathode and the single pores. Consequently, discharge product deposition (ideally Li_2O_2) proceeds at the open side of the cell, blocking further oxygen transport into the

*Fraunhofer Institute for Manufacturing Technology and Advanced Materials, Project Group for Electrical Energy Storage, Oldenburg, Germany

cathode.[36] Thus, the electrode design is another challenging issue towards the feasibility of Li/air batteries and has to be considered along with the search for a suitable electrolyte to achieve a large active surface area, prevent pore clogging, and ensure a uniform deposition of discharge product to avoid passivation effects. A possible route to achieve a more uniform discharge product deposition is a non-uniform distribution of catalytically active sites in order to counteract the oxygen transport limitation and clogging. Many studies have been devoted to catalysis in Li/air batteries.[37–43] Initially they solely aimed at the speeding up of the kinetically slow ORR and OER to reduce the high overpotential between the charge and the discharge process via α-MnO_2, Pd, Pt, and Au nanoparticles. Figure 1.6 (b) shows the successful decrease of charge potential and increase of discharge potential for a combined Pt/Au catalyst in comparison with an uncatalyzed carbon cathode.[42] The stability of the discharge potential over several charge/discharge cycles is demonstrated in Figure 1.6 (c) for Pt, Au, and Pd catalysts in different electrolytes. In terms of a catalyzing effect and stability this is particularly successful for the electrolyte DMSO.[30] The application of adequate catalysts distribution along the transport tunnel to counteract pore clogging provides the potential of inhibiting a fast oxygen starvation of the porous cathode structure. Furthermore, a smart catalyst distribution and hence a more uniform discharge product deposition diminishes the effect of passivation and increases the pore volume utilization that yields a significant increase in battery capacity.

In this work we focus on two issues which we assume to be highly capacity-limiting and/or of fundamental importance for the understanding of the elementary processes in Li/air batteries. Nonetheless, all issues concerning Li/air batteries are not stand-alone problems but interrelate in a complex manner of mutual influence. The choice of analyzing tools is a purely computational multi-scale approach. Due to the different nature of the applied computational methods, assets and drawbacks of both approaches are discussed separately in the relevant parts.

In Part I of the present thesis our attention is focused on the reaction mechanisms of Li/air batteries. In particular, we study the charge process on small amorphous Li_nO_n clusters which we assume to be a good representative model of the amorphous discharge product. The method of choice is based on first principles using Car-Parrinello molecular dynamics and density functional theory (DFT). DFT-based simulations offer a quantum-mechanical accuracy that is necessary to gain information about structural stability, electronic properties as well as dynamical processes without preconditions based on empirical assumptions. Concomitant with experiments, this technique provides the opportunity of a thorough understanding of the charge/discharge cycle in Li/air batteries. In particular, in operando measurements of lithium-based battery cells are challenging due to the high reactivity of the involved species and often reduced to an analysis after a

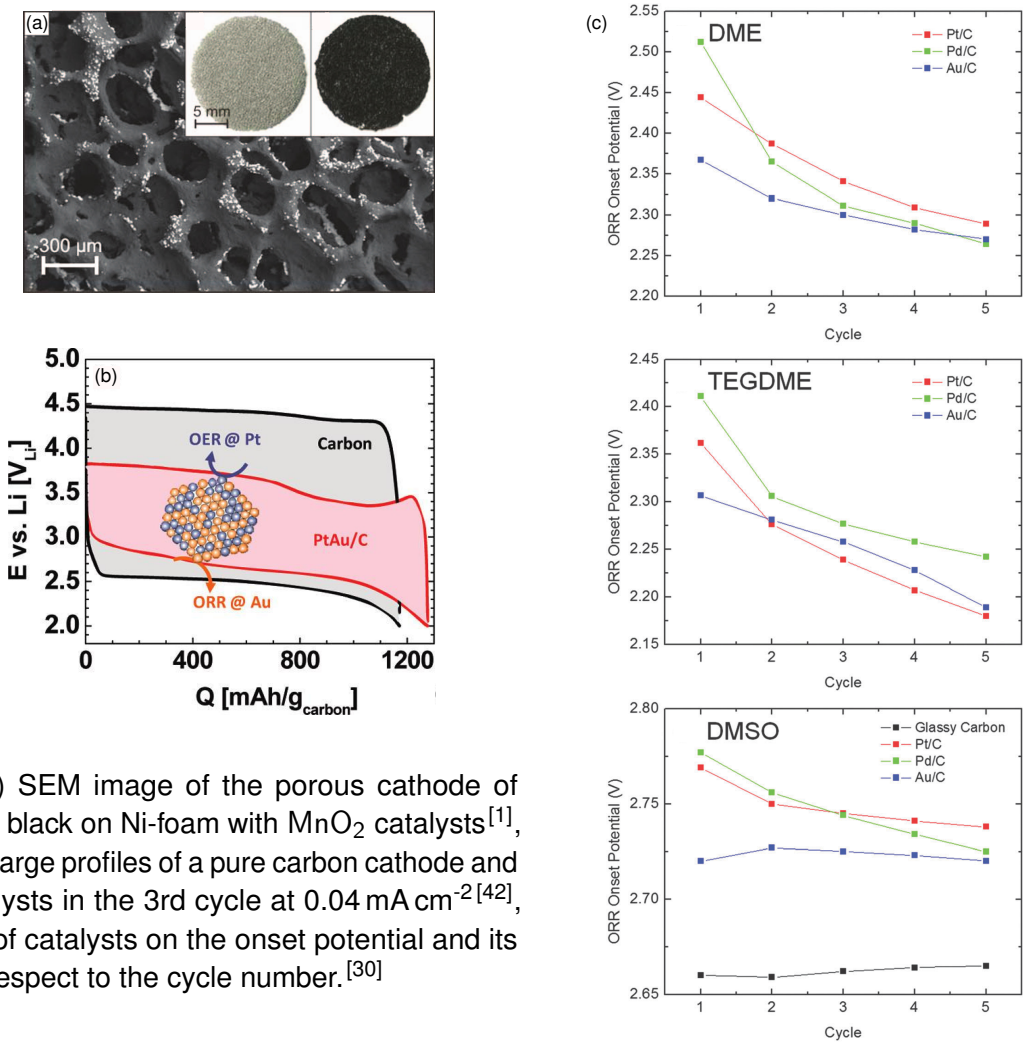

Figure 1.6.: (a) SEM image of the porous cathode of Super P carbon black on Ni-foam with MnO_2 catalysts[1], (b) charge/discharge profiles of a pure carbon cathode and with Pt/Au catalysts in the 3rd cycle at 0.04 mA cm^{-2} [42], and (c) impact of catalysts on the onset potential and its decrease with respect to the cycle number.[30]

charge/discharge process. The advantage of a computational approach based on DFT is an insight into dynamical processes of chemical reaction mechanisms even on time scales of femtoseconds to picoseconds. By this means, we can identify intermediates that are too short-lived to be observed experimentally but can cause other (side) reactions, and thus obtain an overall description of the multi-step charge process. Moreover, owning an insight onto the atomistic scale, we can study the impact of morphology of the discharge product on the decomposition process, since we possess full knowledge and control of the Li_2O_2 structure. However, due to these restrictions in system size and in simulation time, our effort has to be focused on the essential processes.

Therefore, with the intention to study the decomposition process of Li_2O_2 in a realistic environment of the solvent DMSO, the restriction to small Li_nO_n clusters is inevitable. In the beginning of Part I the nature of the charge process in Li/air batteries and its dependency on the Li_2O_2 morphology are summarized in a preceding introduction in Chapter 2, followed by a brief overview

of the applied first principle approach and its computational implementation in Chapter 3 and 4. Before simulating the charge process, we analyze the structural and electronic properties of bulk crystalline lithium and lithium oxides at the level of DFT. A brief comparison and examination of stability in presence of crystalline Li and Li_2O_2 surfaces of the two solvents PC (propylene carbonate) and DMSO is performed with DFT-based calculations. Further analysis of the solvent DMSO is then carried out with classical molecular dynamics simulations. All validating calculations can be found in the second part of Chapter 4. Finally, we generate small Li_nO_n clusters which are decomposed in vacuo as well as in DMSO upon removal of electrons via DFT-based molecular dynamics simulations. The results are analyzed in Chapter 5 and discussed in Chapter 6 in terms of putative reaction mechanisms for the charge process in Li/air batteries.

In Part II of the thesis the main subject of interest is the highly capacity-limiting issue of pore clogging. The oxygen starvation of the cathode and the unused free cathode volume concomitant with a battery capacity loss is governed by the macroscopic growth of discharge product. An atomistic approach is not appropriate to model the clogging of pores due to the much larger time and size scales. Thus, the simulation technique chosen here is based on (macroscopic) physical laws which are typically simpler and faster to solve. By this means, it is possible to describe the macroscopic evolution of discharge product deposition. The experimental access to the exact deposition is hindered by the highly porous and fragile carbon cathode, such that the analysis is often limited to an analysis of the accessible cathode sides of separator and oxygen supply. Modeling the Li_2O_2 deposition enables a detailed insight into the exact deposition inside the porous structure and hence into the reasons for pore clogging. Moreover, this method simultaneously provides the possibility of comparison with experimental results due to simulations on a macroscopic scale. Using a reliable and experimentally verified model, a review of prevention mechanisms as well as optimization techniques to preselect potential electrolytes and to maximize the pore volume utilization is possible without the need of complex and expensive experiments. However, this is done at the expense of the knowledge of the actual microscopic structure. Furthermore, the applied physical laws (such as Fickian diffusion) and physical properties (such as oxygen solubility and diffusivity) have to be justified by experimental results and/or atomistic simulations, concomitantly being aware of the possibilities as well as the limitations of the model.

The dynamical processes and clogging of pores in the implemented model are realized via a reaction-diffusion equation applied to porous structures. This model is based on the approach of Sandhu et al.,[44] a simplified version of the originally developed model for Li-ion batteries by Newman et al.[45,46] It is introduced in the beginning of Chapter 8 after a preceding introduction in Chapter 7, which gives a more detailed insight into the pore clogging issue. The implemented

solver, the method of finite differences, is explained in detail in the second part of Chapter 8 with regard to the system-determining equations. Special attention is devoted to the stability of the applied algorithm, which limits the time step and thus, indirectly, the choice of growth mechanisms. Following the mathematical formulation, the numerical implementation of continuous and locally catalyzed growth is described in Chapter 9. At this point we introduce the Greedy optimization algorithm which is used to maximize the pore volume utilization via a non-uniform catalyst distribution. All benchmark tests as well as a comparison between two applied solvers can be found in the second part of Chapter 9. Finally, the continuous model and the developed localized growth mechanism are studied in four commonly used solvent environments in Chapter 10. Analyzing the continuous growth as a reference measurement, the optimization algorithm is applied in all solvent environments for different growth mechanisms and pore geometries. The resulting optimal catalyst numbers and distributions for the applied solvents are discussed in Chapter 11 with regard to pore volume utilization and improved battery capacity.

The majority of the content of Part I has been accepted for publication in *The Journal of Physical Chemistry C*.[47]
The majority of the content of Part II has been accepted for publication in *Journal of The Electrochemical Society*.[48]

Part 1.

Atomistic modeling of the charge process in lithium/air batteries

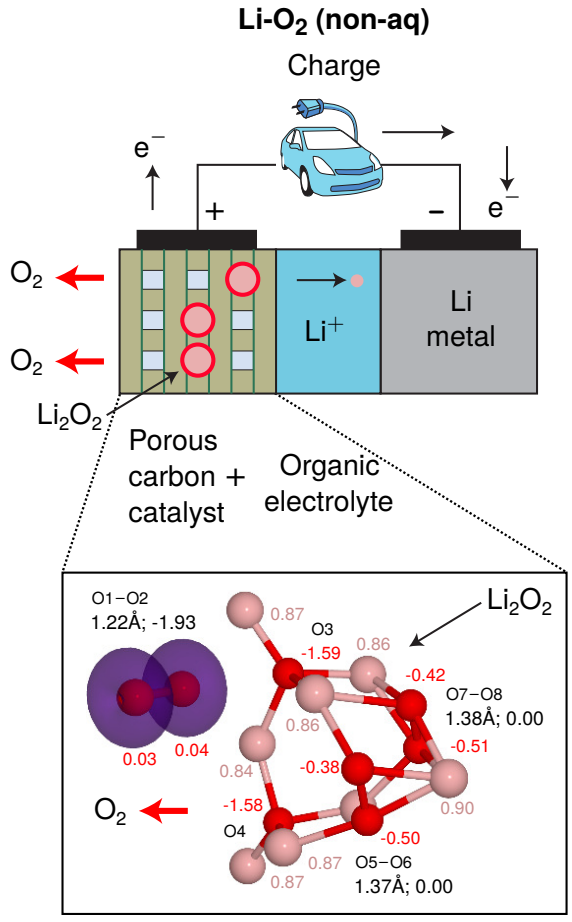

Model of a Li/air battery adapted from ref. 2 (top) and decomposition of Li_2O_2 based on a density functional theory study (bottom).

CHAPTER 2

INTRODUCTION

The high overpotential occurring in the OER during the charge process in Li/air batteries is among the main limiting factors of their efficiency and especially reversibility. Most of the existing literature has focused on the ORR during the discharge process. In non-aqueous, non-carbonate organic electrolytes, the ORR result in the formation of insoluble lithium peroxide, Li_2O_2.[7,22,28,49] Laoire et al.[7,8] has proposed a three-step process for the cathodic reaction, according to equation (1.1) with a chemical and electrochemical reduction of LiO_2 to Li_2O_2 in the last step. Peng et al.[9] confirmed in an experimental study that LiO_2 is indeed an intermediate product in the discharge process which forms at the cathode surface and disproportionates in a second step to Li_2O_2. Based on atomic force microscopy measurements of the thickness of the deposition product, Viswanathan et al.[10] suggested that the growth mechanism during the discharge process is not a simple layer-by-layer growth of bulk Li_2O_2. As also confirmed by several recent experimental studies, the initial growth of Li_2O_2 at higher voltages (2.7 V) proceeds with the formation of disc-like particles composed of thin platelets with bulk (insulating) electronic properties.[11–13] These discs form the core of larger toroidal particles developing at progressively low voltage and presenting an electrically conductive shell. At the end of discharge, superoxide-like species and amorphous Li_2O_2 are found at the surface of the toroidal particles.[11–15]

Importantly, the morphology of the deposited Li_2O_2 strongly influences the (electro-) chemical mechanisms of the OER in the subsequent charge process which are comparatively less well understood.[12] Laoire et al. and Peng et al. have formerly suggested a direct decomposition of Li_2O_2 via a two electron process (equation (1.2)) with no formation of LiO_2 as an intermediate. However, recent work revealed that the OER is far more complex than first assumed and could proceed through a multi-step decomposition process. At low voltages (hence with a small over-

potential), decomposition of the amorphous and/or defective surface species takes place. This is thought to be followed first by delithiation of the toroidal Li_2O_2, supposedly proceeding from the lithium interlayer (Li1 sites in Figure 4.2) and forming LiO_2-like phases, and then by an evolution of molecular oxygen.[11,12,50–53] In a third stage, oxidation of the core discs takes place platelet by platelet. Due to the insulating properties of crystalline Li_2O_2, this third step requires high voltages to ensure sufficient electron transport through the material. Therefore, electrolyte degradation can take place at the end of the charge process, since most of the currently used organic electrolytes are not stable at voltages above 4 V.

Whereas a few theoretical works have addressed the electronic structural details of the charge process limited to the case of crystalline Li_2O_2 phases[50,51] and employing static total energy calculations, nothing is known about the dynamics of the initial decomposition of amorphous Li_2O_2 discharge products. Models for such products have been suggested in the form of small amorphous clusters with Li nuclearities from 2 up to 32 atoms.[14,54] In this part, we present a computational study of the decomposition of similarly small Li_nO_n clusters upon removal of one or two electrons from the simulation system. In the framework of DFT, we perform both static and dynamical analyses of the atomic and electronic structures of bulk lithium (per)oxides as well as small amorphous clusters and of their oxidation reactions. The simulations are performed both in vacuum and in a DMSO environment whose molecular arrangement in the liquid state is optimized by a combination of DFT-based and classical molecular dynamics simulations. DMSO has been chosen as the solvent, since formerly employed alkyl carbonate-based electrolytes have been shown to decompose during the discharge process forming lithium carbonate rather than the desired Li_2O_2.[23–27] Even ether-based electrolytes show a lack of reversibility over several charge/discharge cycles despite the improved stability in comparison to carbonates.[29,30,55] Although DMSO may also decompose when exposed to superoxide species upon very long periods,[34] when combined with Au and TiC cathodes DMSO shows the highest stability during repeated charge and discharge, resulting in a low capacity loss over several hundred cycles.[30–33]

CHAPTER 3

FIRST-PRINCIPLES MOLECULAR DYNAMICS

First-principles molecular dynamics (FPMD) represent a molecular dynamics simulations, in which the potential and the forces acting on the nuclei are determined from electronic structure calculations. Based on quantum mechanics they provide an insight into electronic structures and dynamics of chemical reactions on time and size scales that are often not accessible experimentally. Furthermore, an increase in CPU performance and computer memory, and particularly parallelization techniques concomitant with a good communication system provide the possibility to increase system sizes and to extend simulated trajectories (tens of picoseconds). These improvements in computational resources give FPMD simulations the required chemical accuracy to determine properties of matter as well as a qualitatively predictive character of chemical reaction pathways at various conditions.

In the following we discuss the strategy of the FPMD method applied in the present work. In a first step, after separating the nuclear and the electronic dynamics, we introduce the Car-Parrinello molecular dynamics (CPMD) and reveal the differences and similarities to other approaches such as the Ehrenfest (EMD) and the Born-Oppenheimer molecular dynamics (BOMD). This is followed by a chronological development of the solution of the electronic problem based on density functional theory. With regard to the actual implementation of the method, the chapter closes with a brief introduction into the concept of pseudopotentials.

Unless otherwise specified, the approach is mainly based on the textbook of Marx & Hutter,[56] but also on the textbooks of Burke[57] and Koch & Holthausen.[58]

3.1. Born-Oppenheimer approximation

The challenge in the modeling of chemical systems is the mathematical formulation and the computational implementation of a many-electron system in the presence of nuclei. Starting point of the description of a many-electron system is the non-relativistic time-dependent Schrödinger equation (in a position basis) **

$$i\partial_t \Psi = \hat{\mathcal{H}}\Psi \,, \tag{3.1}$$

where the total wavefunction is $\Psi = \langle \{\boldsymbol{r}_i\}, \{\boldsymbol{R}_I\} | \Psi(t) \rangle = \Psi(\{\boldsymbol{r}_i\}, \{\boldsymbol{R}_I\}, t)$, and $\{\boldsymbol{r}_i\}$ and $\{\boldsymbol{R}_I\}$ are the electronic and the nuclear degrees of freedom. The corresponding fundamental Hamiltonian is given by

$$\begin{aligned} \hat{\mathcal{H}} &= -\frac{1}{2}\sum_i \nabla_i^2 + \sum_{i<j} \frac{1}{|\boldsymbol{r}_i - \boldsymbol{r}_j|} - \sum_{i,I} \frac{Z_I}{|\boldsymbol{r}_i - \boldsymbol{R}_I|} - \frac{1}{2}\sum_I \frac{\nabla_I^2}{M_I} + \sum_{I<J} \frac{Z_I Z_J}{|\boldsymbol{R}_I - \boldsymbol{R}_J|} \\ &= \hat{\mathcal{T}}_e + \hat{\mathcal{V}}_{ee} + \hat{\mathcal{V}}_{eN} + \hat{\mathcal{T}}_N + \hat{\mathcal{V}}_{NN} \\ &= \hat{\mathcal{H}}_e + \hat{\mathcal{T}}_N \,, \end{aligned} \tag{3.2}$$

where M_I is the mass and Z_I the charge of nuclei I, and $\hat{\mathcal{T}}_\bullet$ and $\hat{\mathcal{V}}_\bullet$ are the kinetic and the potential energy operators. In general, electron-related parts are denoted by lower case subscripts (i, j and e), nuclei related parts by upper case subscripts (I, J and N), and operators are indicated by a hat "^". The electron-related terms are summarized in the electronic Hamiltonian $\hat{\mathcal{H}}_e$. The last term $\hat{\mathcal{V}}_{NN}$ is included in the electronic part. Since the purely nuclear interaction acts solely as a constant E_{NN}, it is added to the electronic part causing only a shift of the eigenvalues.

Although considering only the electron-electron, electron-nuclear, and nuclear-nuclear Coulomb interactions, the above problem is already not solvable for a many-electron system in a practical sense. In particular, no separation of a purely electronic and nuclear Hamiltonian is possible due to the coupling term $\hat{\mathcal{V}}_{eN} = \hat{\mathcal{V}}_{eN}(\{\boldsymbol{r}_i\}, \{\boldsymbol{R}_I\})$. Nonetheless, an approximative separation of the nuclear and electronic motion is performed based on the assumption of an adiabatic behavior of the electrons, i. e., the much faster electrons have no heat exchange with their environment and follow the nuclear motion adiabatically. Although both kinds of particles have the same electronic charge, nuclei possess much smaller velocities due to the significantly larger mass $M_I \gg m_e$ and hence interact on different time scales than the electrons. From an electronic point of view nuclei are quasi-static. Thus, the dependency of the electronic Hamiltonian $\hat{\mathcal{H}}_e$ and the electronic

** Unless otherwise specified, all equations are given in atomic units (a. u.), i. e., electron mass m_e, elementary charge e, and the reduced Planck constant $\hbar$ are set to one.

wavefunction ψ on the nuclear degrees of freedom is reduced on a parametric dependency, i. e., nuclei are fixed with respect to the electron motion, and the Born-Oppenheimer separation leads to

$$\Psi = \psi\big(\{\boldsymbol{r}_i\}, \{\boldsymbol{R}_I\}\big) \times \chi\big(\{\boldsymbol{R}_I\}, t\big) \ ,$$

where χ is the nuclear wavefunction. Thus, the electronic Schrödinger equation is reduced to the time independent (stationary) form for every considered set of nuclear coordinates $\boldsymbol{R}_I$ (eigenvalue problem)

$$\hat{\mathcal{H}}_e \psi_n = E_n \psi_n \ , \tag{3.3}$$

where n denotes the number of eigenfunctions and corresponding eigenvalues $E_n = E_n\big(\{\boldsymbol{R_I}\}\big)$. Since $\hat{\mathcal{H}}_e$ is hermitian, ψ_n represent an orthonormal basis (see Appendix F, Definition F.1 and Theorem F.1)

$$\langle \psi_n | \psi_k \rangle = \int \psi_n^*\big(\{\boldsymbol{r}_i\}, \{\boldsymbol{R}_I\}\big) \psi_k\big(\{\boldsymbol{r}_i\}, \{\boldsymbol{R}_I\}\big) \mathrm{d}\boldsymbol{r} = \delta_{nk} \ ,$$

and we can expand the total wavefunction in this basis according to

$$\Psi_{BO}\big(\{\boldsymbol{r}_i\}, \{\boldsymbol{R}_I\}, t\big) = \sum_n \psi_n\big(\{\boldsymbol{r}_i\}, \{\boldsymbol{R}_I\}\big) \chi_n\big(\{\boldsymbol{R}_I\}, t\big) \ .$$

Returning to the time-dependent Schrödinger equation (3.1), we obtain

$$i\partial_t \Psi_{BO} = \hat{\mathcal{H}} \Psi_{BO} = \big(\hat{\mathcal{T}}_N + \hat{\mathcal{H}}_e\big) \Psi_{BO} \ .$$

Multiplying from the left side with ψ_n^* and integrating over all electronic degrees of freedom $\int \mathrm{d}\boldsymbol{r}$ results in

$$\begin{aligned} i\partial_t \chi_n =& \Big\{ -\sum_I \frac{1}{2M_I} \nabla_I^2 + E_n\big(\{\boldsymbol{R}_I\}\big) \Big\} \chi_n \\ &+ \sum_k \Big\{ -\sum_I \frac{1}{2M_I} \int \psi_n^* \nabla_I^2 \psi_k \mathrm{d}\boldsymbol{r} - 2 \sum_I \frac{1}{2M_I} \Big(\int \psi_n^* \nabla_I \psi_k \mathrm{d}\boldsymbol{r} \Big) \cdot \nabla_I \Big\} \chi_k \\ =& \Big\{ \hat{\mathcal{T}}_N + E_k \Big\} \chi_n + \sum_k \Big\{ \hat{\mathcal{T}}_{nk}^{(2)} + 2\hat{\mathcal{T}}_{nk}^{(1)} \Big\} \chi_k \end{aligned} \tag{3.4}$$

using the product rule $\nabla^2(\psi\chi) = \nabla^2\psi\chi + 2\nabla\psi\nabla\chi + \psi\nabla^2\chi$. The resulting time evolution is an entirely nuclear problem since the equation does not depend on the electronic degrees of freedom, while the electronic problem is decoupled from the nuclear motion and provides only a parametric dependency on the nuclear degrees of freedom. Nonetheless, equation (3.4) has to be solved to

determine chemical reactions.

In the Born-Oppenheimer approximation[59] both coupling terms $\hat{\mathcal{T}}_{nk}^{(2)}$ and $\hat{\mathcal{T}}_{nk}^{(1)}$ are neglected, i. e., the nuclei are assumed to move in a potential of eigenenergies $E_n\big(\{\boldsymbol{R}_I\}\big)$ of the electronic solution (potential hypersurfaces) which depend only parametrically on the nuclear degrees of freedom. The Born-Oppenheimer approximation is valid if the electronic wavefunctions do not change strongly with the change of nuclear coordinates, since both coupling terms contain derivatives of the wavefunctions ψ_n. Finally, the approximated and decoupled nuclear Schrödinger equation is given by

$$i\partial_t \chi_n = \Big\{\hat{\mathcal{T}}_N + E_n\Big\}\chi_n \; .$$

3.2. Molecular dynamics

Nuclear motion according to classical molecular dynamics A promising ansatz for the derivation of classical molecular dynamics from the quantum mechanical description of the decoupled nuclear wavefunction (in SI units) is given by

$$\chi_n\big(\{\boldsymbol{R}_I\}, t\big) = A_n\big(\{\boldsymbol{R}_I\}, t\big) \exp\left[iS_n\big(\{\boldsymbol{R}_I\}, t\big)/\hbar\right] \; ,$$

where $A_n \in \mathbb{R}$ is the amplitude and $S_n \in \mathbb{R}$ the phase. Separating real and imaginary parts, two equations arise for A_n and S_n. To derive the nuclear motion according to classical molecular dynamics, we focus on the phase equation in the classical limit $\hbar \to 0$

$$\partial_t S_n + \sum_I \frac{1}{2M_I}\big(\nabla_I S_n\big)^2 + E_n = 0 \; .$$

Using S_n as the generating function for the canonical transformation in the Hamilton-Jacobi formalism, we write

$$\partial_t S_n + \mathcal{H}\big(\{\boldsymbol{R}_I\}, \{\boldsymbol{P}_I\}\big) = 0 \; ,$$

where $\boldsymbol{P}_I = \nabla_I S_n$ represents the momentum and $\mathcal{H}\big(\{\boldsymbol{R}_I\}, \{\boldsymbol{P}_I\}\big) = \mathcal{T}\big(\{\boldsymbol{P}_I\}\big) + E_n\big(\{\boldsymbol{R}_I\}\big)$ the Hamilton function. Thus, the Newtonian equation of motion is given by

$$\begin{aligned} \partial_t \boldsymbol{P}_I &= -\nabla_I \mathcal{H}\big(\{\boldsymbol{R}_I\}, \{\boldsymbol{P}_I\}\big) \\ \Rightarrow \quad \partial_t \boldsymbol{P}_I &= -\nabla_I E_n\big(\{\boldsymbol{R}_I\}\big) \\ \Rightarrow M_I \ddot{\boldsymbol{R}}_I &= -\nabla_I E_n\big(\{\boldsymbol{R}_I\}\big) \; . \end{aligned} \tag{3.5}$$

Again we can state the role of the energy eigenvalues E_n as an effective potential for the nuclear motion.

Born-Oppenheimer molecular dynamics In the BOMD approach the electronic wavefunction is restricted to the ground state wavefunction with corresponding energy E_0 obtained from the time-independent Schrödinger equation (3.3). The ground state energy, which determines the effective potential of the classical nuclear dynamics, is calculated for a set of fixed nuclei with corresponding coordinates $\boldsymbol{R}_I$ via $\hat{\mathcal{H}}_e\psi_0 = E_0\psi_0$. Hence, the time evolution of the quantum mechanical system is not maintained but dictated by the dynamics of the nuclei. On the basis of the obtained energies $E_0\big(\{\boldsymbol{R}_I\}\big)$, the potential energy surface and the corresponding gradient are extrapolated. In a last step the Newtonian equation of motion is solved to obtain the propagation of nuclear motion according to classical dynamics via

$$M_I\ddot{\boldsymbol{R}}_I = -\nabla \min_{\psi_0}\left\{\big\langle\psi_0\big|\hat{\mathcal{H}}_e\big|\psi_0\big\rangle\right\} .$$

Notably, although in contrast to the following EMD the minimization procedure has to be performed in each BOMD step, which makes the BOMD computationally very expensive, these simulations can be performed at much larger time steps.

Ehrenfest molecular dynamics In the EMD approach the electronic structure problem is solved using the time-dependent Schrödinger equation and the Newtonian equation of motion to obtain the nuclear dynamics. Both coupled equations (restricted to the ground state)

$$\begin{aligned} M_I\ddot{\boldsymbol{R}}_I &= -\nabla\big\langle\psi_0\big|\hat{\mathcal{H}}_e\big|\psi_0\big\rangle \\ i\partial_t\psi_0 &= \hat{\mathcal{H}}_e\psi_0 \end{aligned}$$

are then solved simultaneously such that a calculation of the potential energy surface is not required. The time-dependent Schrödinger equation, which determines the electronic wavefunctions, is solved “on-the-fly”, obviating the minimization in each step and preserving the electronic time evolution. Nonetheless, since the time evolution is defined by the fast electronic dynamics, only very small integration time steps are feasible.

Car-Parrinello molecular dynamics In the CPMD approach we attempt to take advantage from both the BOMD as well as the EMD, i. e., a larger integration time step comparable to the BOMD while the electronic wavefunctions are kept in their minimum during the nuclear propagation

(smooth electronic time evolution) as in the EMD. For this purpose, the adiabatic separation idea of Born and Oppenheimer of fast electronic and slow nuclear motion is used to transfer the combined quantum mechanical/classical problem to a combined classical/classical problem on different energy scales. Once again the separation and mapping on different scales is performed at the expense of the electronic time evolution. Furthermore, we introduce single electron wavefunctions (orbitals) ϕ_i in the sense of electronic dynamic variables such that $\psi_0 = \psi_0\big(\{\phi_i\}\big)$. Their meaning and significance for the solution of the electronic problem in a DFT approach are illuminated in Section 3.3 and following. While the energy of the electronic system $\big\langle\psi_0\big|\hat{\mathcal{H}}_e\big|\psi_0\big\rangle$ has been considered, so far, as a function of the nuclear coordinates (in a parametric dependency), we can also assume the energy as a function of the wavefunction and hence the orbitals ϕ_i. In summary, we state two classical problems with dynamic variables $\boldsymbol{R}_I$ and ϕ_i for the nuclear and the electronic problem. The corresponding Lagrangian introduced by Car and Parrinello[60] is given by

$$\mathcal{L}_{CP} = \sum_I \frac{M_I}{2}\dot{\boldsymbol{R}}_I^2 + \mu\sum_i \frac{1}{2}\langle\dot{\phi}_i|\dot{\phi}_i\rangle - \langle\psi_0|\hat{\mathcal{H}}_e|\psi_0\rangle + constraints\ , \tag{3.6}$$

where the first two terms determine the nuclear and the electronic kinetic energy with corresponding fictitious mass μ and $\langle\psi_0|\hat{\mathcal{H}}_e|\psi_0\rangle$ the potential energy. The constraints are given for example by an assumption of orthonormal orbitals via $constraints = \sum_{i,j}\Lambda_{ij}(\langle\phi_i|\phi_i\rangle - \delta_{ij})$, where Λ_{ij} are the Lagrange multipliers. Thus, the Euler-Lagrange equations with respect to the dynamic variables

$$\begin{aligned}
\mathrm{d}_t\big(\partial_{\dot{\boldsymbol{R}}_I}\mathcal{L}_{CP}\big) = \partial_{\boldsymbol{R}_I}\mathcal{L}_{CP} &\Rightarrow M_I\ddot{\boldsymbol{R}}_I = -\partial_{\boldsymbol{R}_I}\big\langle\psi_0\big|\hat{\mathcal{H}}_e\big|\psi_0\big\rangle + \partial_{\boldsymbol{R}_I}\{constraints\}\\
\mathrm{d}_t\big(\delta_{\dot{\phi}_i^*}\mathcal{L}_{CP}\big) = \delta_{\phi_i^*}\mathcal{L}_{CP} &\Rightarrow \mu\ddot{\phi}_i = -\delta_{\phi_i^*}\big\langle\psi_0\big|\hat{\mathcal{H}}_e\big|\psi_0\big\rangle + \delta_{\phi_i^*}\{constraints\}
\end{aligned} \tag{3.7}$$

determine the nuclear motion and the forces on the orbitals ϕ_i. While the nuclear motion proceeds at a temperature $\propto \sum_I \frac{M_I}{2}\dot{\boldsymbol{R}}_I^2$, the electronic evolution is determined by a temperature $\propto \sum_i \frac{\mu}{2}\langle\dot{\phi}_i|\dot{\phi}_i\rangle$. That is to say, "cold" electrons remain close to their ground state energy $E_0 = \min_{\{\phi_i\}}\langle\psi_0|\hat{\mathcal{H}}_e|\psi_0\rangle$. Furthermore, also the wavefunctions, which have to be optimized only for an initial configuration of nuclei, are assumed to remain close to the ground state configuration during the nuclear time evolution. To ensure the thermal separation but maintain the adiabatic behavior of the electrons following the nuclear motion, it is necessary to prevent an overlap in the nuclear and electronic power spectra, i. e., to separate both motions on two different energy scales via the assumption $\omega_e^{min} \gg \omega_N^{max}$, where ω_e^{min} is the lowest electronic frequency and ω_N^{max} is the highest nuclear frequency. Furthermore, the lowest electronic frequency is determined by the

energy gap E_{gap} between the lowest unoccupied and the highest occupied orbital according to

$$\omega_e^{min} \propto \left(\frac{E_{gap}}{\mu} \right) .$$

Since ω_N^{max} and E_{gap} are fixed by the physical conditions of the system, separation is controlled solely by the fictitious mass μ, whose decrease cause a broadening of the entire spectrum according to

$$\omega_e^{max} \propto \left(\frac{E_{cut}}{\mu} \right) \quad \Leftrightarrow \quad \Delta t^{max} \propto \left(\frac{\mu}{E_{cut}} \right) , \tag{3.8}$$

where E_{cut} is the maximum kinetic energy in a plane wave expansion of the wavefunction (for details see Section 3.3.5) and Δt^{max} governs the maximum time step for the CPMD step.

For extensions of the approach in the case of metallic systems ($E_{gap} = 0$) see ref. 61 and 62.

3.3. Density functional theory

Density functional theory represents a fast access to the complex many-electron system, in particular to the solution of the separated electronic problem. Based on the Hohenberg-Kohn theorems, the main idea is to determine the total electronic wavefunction as well as the system-regrading quantities via the electron density functional. By this means, the explicit treatment of the $3N$ spatial degrees of freedom of a N-body problem can be reduced to the 3 degrees of freedom of the electron density.

In the next section we follow step-by-step the ideas that conclude in the development of DFT and reveal the computational limits and practical implementations such as cutoff energies, finite k-point grids and applied exchange-correlation functionals.

3.3.1. Hartree-Fock approximation

The ground state energy of the electronic system is determined by the ground state wavefunction via the expectation value in this state

$$E_0 = \left\langle \psi_0 \middle| \hat{\mathcal{H}}_e \middle| \psi_0 \right\rangle .$$

On the other hand, we consider the ground state energy as a functional of the total wavefunction, i. e., a mapping from the vector space of wavefunctions into a scalar field (“function of a function”, Appendix F, Definition F.3). Thus, we convert the calculation of the ground state energy to a

minimization problem with respect to trial wavefunctions ψ according to

$$E_0 = \min_{\psi} E_0[\psi] \; .$$

Nonetheless, for a N-electron system characterized by a wavefunction $\psi\big(\{\boldsymbol{r}_i\}\big)$, where $i = 1, \ldots, N$, the problem has still $3N$ degrees of freedom. Since it is not possible to determine and test all feasible wavefunctions for the N-electron problem, the minimization is reduced to the consideration of selected forms of the total wavefunction ψ. One of the simplest approaches is the Hartree ansatz (H) of N uncorrelated electrons and can be realized as a product of single electron wavefunctions ϕ_i in the form $\psi_H \propto \prod_{i=1}^{N} \phi_i(\boldsymbol{r}_i)$. Taking into account Pauli's exclusion principle, Hartree and Fock (HF) approximated the total wavefunction with an antisymmetric product of the single electron wavefunctions in the case of fermions (and symmetric for bosons) represented by a Slater determinant (SD)

$$\psi_{SD} = \frac{1}{\sqrt{N!}} \begin{vmatrix} \phi_1(\boldsymbol{r}_1) & \phi_2(\boldsymbol{r}_1) & \cdots & \phi_N(\boldsymbol{r}_1) \\ \phi_2(\boldsymbol{r}_2) & \phi_2(\boldsymbol{r}_2) & \cdots & \phi_N(\boldsymbol{r}_2) \\ \vdots & \vdots & \ddots & \vdots \\ \phi_1(\boldsymbol{r}_N) & \phi_2(\boldsymbol{r}_N) & \cdots & \phi_N(\boldsymbol{r}_N) \end{vmatrix} \; .$$

Demanding orthonormality of the single orbitals, the resulting Hartree-Fock energy is then given by

$$\begin{aligned} E_{HF}\big[\{\phi_i\}\big] &= \big\langle \psi_{SD} \big| \hat{\mathcal{H}}_e \big| \psi_{SD} \big\rangle \\ &= \sum_{i=1}^{N} \big\langle \phi_i \big| \hat{\mathcal{F}} \big| \phi_i \big\rangle \; . \end{aligned}$$

The Fock operator $\hat{\mathcal{F}}$ is stated as

$$\begin{aligned} \hat{\mathcal{F}} &= \hat{h} + \frac{1}{2} \sum_{j=1}^{N} \Big(\big\langle \phi_j \big| \hat{w} \big| \phi_j \big\rangle - \big| \phi_j \big\rangle \big\langle \phi_j \big| \hat{w} \Big) \\ &= \hat{h} + \underbrace{\frac{1}{2} \sum_{j=1}^{N} \Big(\hat{\mathcal{J}}_j(\boldsymbol{r}) - \hat{\mathcal{K}}_j(\boldsymbol{r}) \Big)}_{\text{Hartree-Fock potential}} = \hat{h} + \hat{\mathcal{V}}_H + \hat{\mathcal{V}}_x \; , \end{aligned} \tag{3.9}$$

where $\hat{h} = -\frac{\nabla_r^2}{2} + \hat{\mathcal{V}}_{eN} + \hat{\mathcal{V}}_{NN}$ and $\hat{w} = |\boldsymbol{r} - \boldsymbol{r}'|^{-1}$. Acting on an electron i as $\hat{\mathcal{J}}_j(\boldsymbol{r}) \big| \phi_i \big\rangle = \big\langle \phi_j \big| \hat{w} \big| \phi_j \big\rangle \big| \phi_i \big\rangle$, the first term in the Hartree-Fock potential describes the Coulombic

effect on electron i in the presence of the $N-1$ remaining electrons. Since the so-called Hartree term does not require the knowledge of $\phi_i(\boldsymbol{r})$ over the whole space, the potential part is called local, in contrast to the second operator $\hat{\mathcal{K}}_j(\boldsymbol{r})\big|\phi_i\big\rangle = \big\langle\phi_j\big|\hat{w}\big|\phi_i\big\rangle\big|\phi_j\big\rangle$. Here, electrons i and j are exchanged (subscript x) and the orbital $\phi_i(\boldsymbol{r})$ has to be evaluated over the whole space due to $\big\langle\phi_j\big|\hat{w}\big|\phi_i\big\rangle = \int \phi_j^*(\boldsymbol{r})\ \hat{w}\ \phi_i(\boldsymbol{r})\mathrm{d}\boldsymbol{r}$. Thus, the second part of the Fock potential is non-local and has no classical counterpart. Without the assumption of antisymmetry for fermions the exchange part vanishes.

While electron exchange and electron correlation between parallel spins (Hartree/Coulomb term) are taken into account in the Hartree-Fock approach, correlation is entirely neglected for antiparallel spin leading to a Hartree-Fock energy E_{HF} larger than the real ground state energy E_0. Despite this fact, the Hartree-Fock approach provides the basic ideas how to handle the electronic problem, which we take advantage from in the following sections deriving the density functional theory.

3.3.2. Hohenberg-Kohn theorems

The fundamental concept of the density functional theory is based on the two theorems of Hohenberg and Kohn.[63] Considering an interacting system in a system-dependent external potential $\mathcal{V}_{ext} = \mathcal{V}_{eN} + \mathcal{V}_{NN}$, the idea is to reduce the $3N$ spatial degrees of freedom of the N-electron wavefunction ψ to only three spatial degrees of freedom of the electron density

$$n(\boldsymbol{r}) = N\sum_{\sigma}\sum_{\sigma_1}\cdots\sum_{\sigma_N}\int\cdots\int\big|\psi(\boldsymbol{r},\sigma,\boldsymbol{r}_2,\sigma_2\ldots,\boldsymbol{r}_N,\sigma_N)\big|^2\mathrm{d}\boldsymbol{r}_2\ldots\mathrm{d}\boldsymbol{r}_N\ .$$

Here $\boldsymbol{r}_i$ denotes the spatial coordinate and σ_i the spin of electron i, i. e., an electron is fixed at position $\boldsymbol{r}$, and the sum is carried out over the probabilities of all possible positions of the $N-1$ remaining electrons represented by the probability density $\big|\psi\big|^2$.

Since the electron density itself is a function of the electron position $\boldsymbol{r}$, all electron density dependent quantities are functionals of n (see Section 3.3.1 and Appendix F, Definition F.3). According to the first theorem of Hohenberg and Kohn,

Theorem 3.1. *(Hohenberg-Kohn I)*
"$\mathcal{V}_{ext}(\boldsymbol{r})$ is a unique functional of $n(\boldsymbol{r})$, apart from a trivial additive constant" [63]

and has been demonstrated by the authors using proof by contradiction.

Since the kinetic energy $\mathcal{T}_e$ as well as the electron-electron interaction $\mathcal{V}_{ee}$ in the electronic Hamilton function $\mathcal{H}_e$ (see equation (3.2)) are universal and $\mathcal{V}_{ext}$ is a unique functional of the

electron density (according to the first theorem), all system-regrading quantities such as the total energy

$$E[n] = \mathcal{T}_e[n] + \mathcal{V}_{ee}[n] + \mathcal{V}_{ext}[n] = \mathcal{F}_{HK}[n] + \int \mathcal{V}_{ext}(\boldsymbol{r}) n(\boldsymbol{r}) \mathrm{d}\boldsymbol{r}$$

can be expressed as functionals of the electron density in a unique way. Furthermore, determining the correct electron density allows us to calculate the ground state energy E_0 based on Hohenberg's and Kohn's second theorem:

Theorem 3.2. *(Hohenberg-Kohn II)*
"$E_0[n]$ assumes its minimum value for the correct $n(\boldsymbol{r})$, if the admissible functions are restricted by the condition $N[n] = \int n(\boldsymbol{r}) \mathrm{d}\boldsymbol{r} = N$." [63]

Thus, under the normalization constraint for the electron density, minimizing the energy functional

$$E_0 = E[n_0] = \min_n \{E[n]\}$$

results in the ground state energy in a unique way, where n_0 is the ground state electron density.

3.3.3. Kohn-Sham ansatz

While the external potential can be evaluated via an integration using the electron density, the Hohenberg-Kohn functional $\mathcal{F}_{HK}[n]$ is still unknown. Kohn and Sham (KS) proposed an ansatz for the functional based on the idea of non-interacting electrons in a fictitious potential which are chosen to produce the same ground state electron density $n_0(\boldsymbol{r})$ as the interacting system.[64] For this reason, $\mathcal{F}_{HK}[n]$ is divided into the classical part of the kinetic energy functional $\mathcal{T}_s[n]$ of non-interacting electrons (single-electron equations) and the Hartree energy functional $E_H[n] = \frac{1}{2} \int \int n(\boldsymbol{r})\, \hat{w}\, n(\boldsymbol{r'}) \mathrm{d}\boldsymbol{r}\, \mathrm{d}\boldsymbol{r'}$ (equivalent to the Hartree potential $\hat{\mathcal{V}}_H(\boldsymbol{r})$ in the Hartree-Fock approach in Section 3.3.1) which considers the classical Coulomb interactions. All non-classical electron-electron interactions and correlations (Pauli's exclusion principle, Coulombic correlation between electrons with parallel and antiparallel spins) are covered via an exchange-correlation energy functional $E_{xc}[n]$ such that the Kohn-Sham energy functional is given by

$$E_{KS}[n] = \mathcal{T}_s[n] + E_H[n] + \mathcal{V}_{ext}[n] + E_{xc}[n]\ ,$$

where $E_{xc}[n] = \mathcal{T}_e[n] - \mathcal{T}_s[n] + \mathcal{V}_{ee}[n] - E_H[n]$, i. e., the exchange-correlation energy is the kinetic energy difference between the non-interacting and interacting system as well as the non-classical part of the internal potential.

The advantage of the Kohn-Sham ansatz is based on the exact determination of the kinetic energy of non-interacting electrons and hence the reduction of the uncertainty in the Hohenberg-

Kohn functional on a small contribution of the (still unknown) exchange-correlation functional. Furthermore, in the framework of the Kohn-Sham ansatz, non-interacting electrons are given by auxiliary orbitals $\{\phi_i(\boldsymbol{r})\}$ (KS orbitals) in an effective KS potential $\mathcal{V}_{KS}(\boldsymbol{r})$. The electronic problem is then reduced to the solution of the one-electron Kohn-Sham equations

$$\hat{\mathcal{H}}_e^{KS}\phi_i(\boldsymbol{r}) = \left\{ -\frac{\nabla_i^2}{2} + \mathcal{V}_{KS}(\boldsymbol{r}) \right\}\phi_i(\boldsymbol{r}) = \epsilon_i\phi_i(\boldsymbol{r}) \ . \tag{3.10}$$

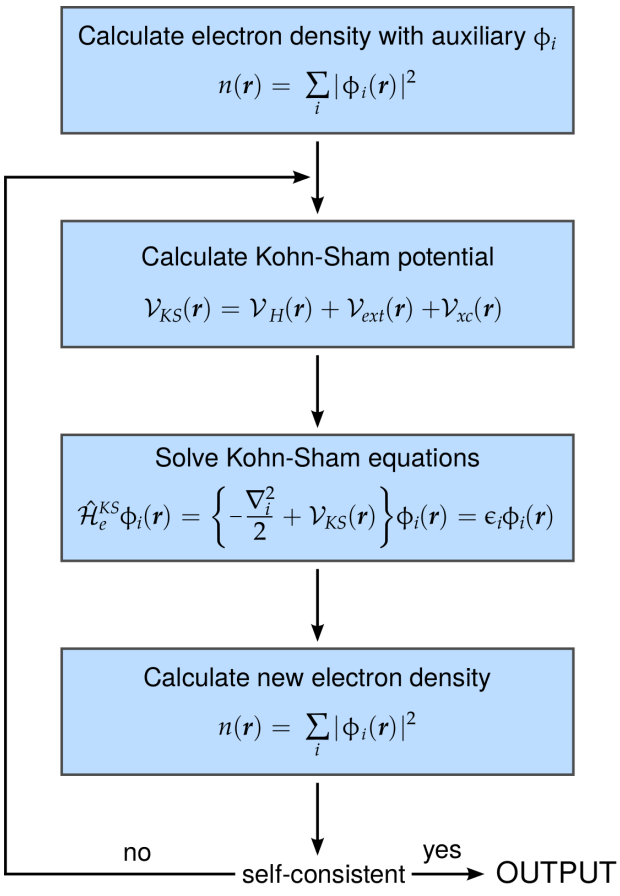

Figure 3.1.: Flowchart for the self-consistent iterative solution of the KS equations (adapted from ref. 65 and 66).

A functional derivative with respect to the electron density (Appendix F, Definition F.4) results in the KS potential

$$\mathcal{V}_{KS}(\boldsymbol{r}) = \mathcal{V}_H(\boldsymbol{r}) + \mathcal{V}_{ext}(\boldsymbol{r}) + \mathcal{V}_{xc}(\boldsymbol{r}) \ ,$$

where

$$\mathcal{V}_H(\boldsymbol{r}) = \int \frac{n(\boldsymbol{r}')}{|\boldsymbol{r} - \boldsymbol{r}'|} \mathrm{d}\boldsymbol{r}'$$

and

$$\mathcal{V}_{xc}(\boldsymbol{r}) = \frac{\delta E_{xc}[n]}{\delta n(\boldsymbol{r})} \ ,$$

while the electron density is given by the sum of the occupied KS orbitals

$$n(\boldsymbol{r}) = \sum_i \left|\phi_i(\boldsymbol{r})\right|^2 .$$

The procedure of solving the KS equations self-consistently is shown schematically in Figure 3.1. Since the KS single-electron Hamiltonian $\hat{\mathcal{H}}_e^{KS}$ still includes the many-body effects via the exchange-correlation functional, the equations have to be solved self-consistently to obtain the ground state electron density and the corresponding orbitals. Note that the KS orbitals as well as the energies have no strict physical meaning. The relevant quantities are the ground state electron density and the total energy. Although the uncertainty is reduced to the exchange-correlation functional, this part is still unknown. A selection of broadly used approximation methods is subject of the next section.

3.3.4. Exchange-correlation functionals

The simplest approximation for the exchange-correlation functional is the so-called Local (Spin) Density Approximation (L(S)DA). In this case the exchange-correlation energy density ϵ_{xc} in the exchange-correlation functional

$$E_{xc}^{LDA}[n] = \int n(\boldsymbol{r})\epsilon_{xc}^{hom}\big(n(\boldsymbol{r})\big)\,\mathrm{d}\boldsymbol{r}$$

is approximated with the energy density of a homogeneous (but interacting) electron gas evaluated at the local electron density $n(\boldsymbol{r})$ at point $\boldsymbol{r}$ of the inhomogeneous system. The exchange-correlation energy is separated into the exchange part, which can be calculated analytically using Slater determinants (for details see the Hartree-Fock approach in Section 3.3.1), and the correlation part which, however, has to be obtained from Quantum Monte-Carlo simulations.[67] The validity of the LDA is given only for slowly changing densities and not strongly correlated systems. While binding energies are overestimated in the LDA approach (bond lengths are underestimated by 1-3 %), ground state energies are usually too low. In a generalized formulation of spin polarized systems (LSDA), the functional dependency on the electron density $[n]$ is replaced with $[n^{\uparrow}, n^{\downarrow}]$ of the two spin states of opposite directions or with $[n, \zeta]$, where $\zeta(\boldsymbol{r}) = n^{\uparrow}(\boldsymbol{r}) - n^{\downarrow}(\boldsymbol{r})$ is the spin density.

A more sophisticated approach to the exchange-correlation functional is the General Gradient Approximation (GGA)

$$E_{xc}^{GGA}[n] = \int n(\boldsymbol{r})\epsilon_{xc}\Big(n^{\uparrow}(\boldsymbol{r}), n^{\downarrow}(\boldsymbol{r}), \nabla n^{\uparrow}(\boldsymbol{r}), \nabla n^{\downarrow}(\boldsymbol{r})\Big)\,\mathrm{d}\boldsymbol{r}\,.$$

Although locality is still present in the GGA approach, variations of the electron density at point $\boldsymbol{r}$ are taken into account in form of first derivatives, and thus GGA can provide more accuracy in the determination of geometries as well as ground state energies. Some of the most successful and broadly used GGA functionals have been developed by Becke,[68] Perdew, Burke, and Ernzerhof (PBE)[69] and the functional of Perdew and Wang (PW91)[70] which is applied in the present work.

A comparison of both methods is performed on the example of metallic lithium. Figure 3.2 shows the total energy E with respect to the lattice constant a obtained from a DFT-based calculation using a LDA and a GGA functional. As evident from the simulation results, the equilibrium lattice constant a_{LDA} = 3.38 Å deviates from the experimental value of a_{exp} = 3.49 Å[71] by about 3.2 %, while the lattice constant a_{GGA} = 3.45 Å differs only by 1.1 %. Despite the obvious improvement in the present case, GGA does not always provide a more accurate solution, since it can overcompensate

the weaknesses of LDA.

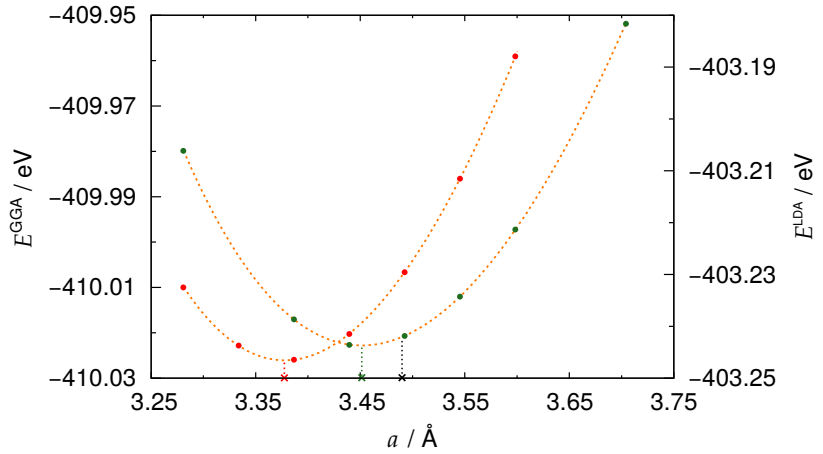

Figure 3.2.: Total energy E with respect to the lattice constant a of metallic lithium for LDA (red) and GGA (green) with corresponding equilibrium lattice constants and an experimental value in black as crosses. The discrete data points are fitted based on the Murnaghan equation of states (orange).[72]

Another group of very successful exchange-correlation functionals are represented by the so-called hybrid functionals. These functionals are a combination of standard density functionals E_{xc}^{DF} such as GGA or LDA and an exchange functional E_x^{HF} from the KS ansatz, obtained in a similar way to the Hartree-Fock method in Section 3.3.1, e. g., $E_{xc} = \frac{1}{2}\left(E_{xc}^{DF} + E_x^{HF}\right)$. Although more accurate, hybrid functionals increase the computational time significantly.

3.3.5. Bloch theorem and cutoff energy

The quantification of the electronic wavefunction requires an appropriate basis set of orbitals ϕ_i. In the case of a crystalline structure the translational symmetry implies a periodic potential and hence a periodic electron density. Thus, periodic boundary conditions (PBC) to save computational effort and the choice of a plane wave basis set to expand the electronic wavefunction emerge naturally.

However, also in the case of surfaces and non-crystalline structures plane wave basis sets are applied, provided that a sufficiently large supercell (vacuum region in the case of surfaces) is used, such that undesired interactions with their periodic images are avoided. Starting from the idea of a periodic potential, we can apply Bloch's theorem:[71]

Theorem 3.3. *(Bloch) In a periodic potential*

$$\mathcal{V}(\boldsymbol{r}) = \mathcal{V}(\boldsymbol{r} + \boldsymbol{a})$$

with periodicity $\boldsymbol{a}$ the solution of the stationary Schrödinger equation is given by plane waves

$$\phi_j(\boldsymbol{r}, \boldsymbol{k}) = u_j(\boldsymbol{r}, \boldsymbol{k}) \exp(i\boldsymbol{k}\boldsymbol{r}) ,$$

where $u_j(\boldsymbol{r}, \boldsymbol{k})$ is a periodic function with periodicity $\boldsymbol{a}$, and $\boldsymbol{k}$ is a vector in the first Brillouin zone of the reciprocal space.

Associating the periodic potential with the KS potential and expanding also the periodic function in the plane wave basis for every state j

$$u_j(\boldsymbol{r}, \boldsymbol{k}) = \sum_{\boldsymbol{G}} c_j(\boldsymbol{G}, \boldsymbol{k}) \exp(i\boldsymbol{G}\boldsymbol{r}) ,$$

we can write the KS orbitals as

$$\phi_j(\boldsymbol{r}, \boldsymbol{k}) = \sum_{\boldsymbol{G}} c_j(\boldsymbol{G}, \boldsymbol{k}) \exp\left(i(\boldsymbol{G} + \boldsymbol{k})\boldsymbol{r}\right) ,$$

where $\boldsymbol{G}$ are reciprocal space vectors and $c_j(\boldsymbol{G}, \boldsymbol{k}) \in \mathbb{C}$. Thus, the electron density is finally expanded in the same basis set according to

$$n(\boldsymbol{r}) = \sum_j \int \sum_{\boldsymbol{G}, \boldsymbol{G}'} c_j^*(\boldsymbol{G}', \boldsymbol{k}) c_j(\boldsymbol{G}, \boldsymbol{k}) \exp\left(i(\boldsymbol{G} + \boldsymbol{k})\boldsymbol{r}\right) \mathrm{d}\boldsymbol{k} .$$

Note that the expansion of the electron density requires double the range of reciprocal space vectors due to the sum over $\boldsymbol{G}$ and $\boldsymbol{G}'$.

Two simplifications are made in the practical calculation of the electron density. First, the integration over the first Brillouin zone is approximated with a finite sum of special weighted $\boldsymbol{k}$-points via $\int \mathrm{d}\boldsymbol{k} \approx \sum_{\boldsymbol{k}} w_k$. To reduce the computational effort even further, i. e., to reduce the number of $\boldsymbol{k}$-points, advantage is taken of translational and rotational symmetries of crystalline structures. In which way symmetries can reduce the number of $\boldsymbol{k}$-points is shown on a simple two-dimensional equidistant lattice in Figure 3.3, where the number of $\boldsymbol{k}$-points is reduced to one third of the initially required value (Figure 3.3 (a)) due to a shift and a diagonal symmetry (Figure 3.3 (b)).

The second approximation is the limitation of the infinite sum over reciprocal space vectors $\boldsymbol{G}$

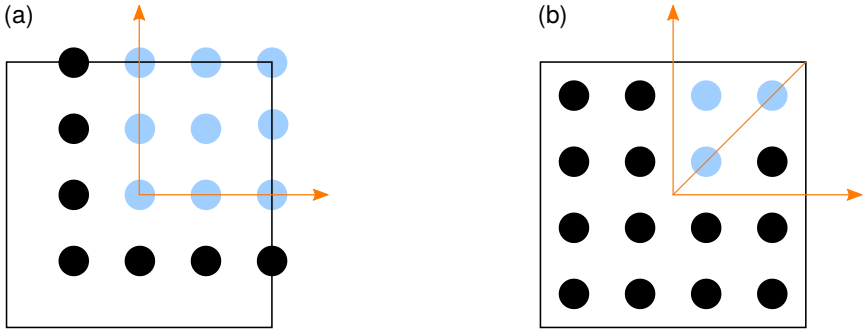

Figure 3.3.: Two-dimensional equidistant lattice (a) before a shift with 9 required $\boldsymbol{k}$-points (blue) and (b) after a shift with 3 required $\boldsymbol{k}$-points (adapted from ref. 65).

via a maximum kinetic energy E_{cut} (cutoff energy) according to

$$\frac{1}{2}|\boldsymbol{k}+\boldsymbol{G}|^2 \leq E_{cut} \ .$$

Apart from the limitation of reciprocal space vectors, the cutoff energy determines the maximum time step in the CPMD, as introduced in Section 3.2 in equation (3.8). The simplification is based on the assumption of a fast convergence of the KS potential and shown exemplary in Figure 3.4 for a supercell of a Li_8O_8 cluster in a solvent of 39 DMSO molecules (see Chapter 4 and 5 for more details). The energy difference relative to the cutoff value of 80 Ry is about 0.17 % for E_{cut} = 20 Ry and decreases to 0.004 % already for E_{cut} = 40 Ry. In the next step for E_{cut} = 60 Ry the improvement is less dramatically of about 0.006 %. Simultaneously, the runtime is increasing approximately linearly with increasing cutoff energy. Thus, a good compromise between accuracy and computation time efficiency for the applied code and the addressed problem is an energy cutoff of 40 Ry, which is chosen in the present work.

A huge advantage of a plane wave approach is its simple treatment in the Fourier-transformed $\boldsymbol{G}$-space, where derivatives are reduced to simple multiplications. Furthermore, due to the lack of origin, the plane wave basis set is considered as an unbiased basis which does not depend on the nuclei positions. The quality of the approximation is solely controlled by the cutoff energy.

Nonetheless, one should be aware of the disadvantages of a plane wave approach. An unbiased basis set does not differentiate regions of high inhomogeneity such as surface supercells which include large vacuum spaces. Furthermore, the treatment in the Fourier space results in a poor resolution of small structures in the real space. Due to the reciprocal character of the Fourier transformation, a high number of coefficients is required in the Fourier decomposition of the orbitals for an adequate description of the real space. The issue of “small structures” arises in the near-core area, where valence-electron wavefunctions show high frequency oscillations due to the

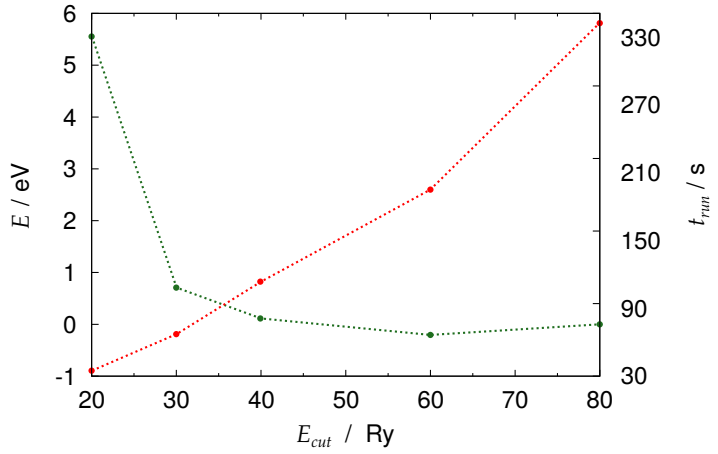

Figure 3.4.: Total energy E (relative to 80 Ry) (green) and runtime t_{run} (red) with respect to the cutoff energy for a Li_8O_8 cluster in a solvent of 39 DMSO molecules. First 200 steps of the electronic minimization calculation of a 17 Å edge length supercell at the Γ-point (center of the first Brillouin zone).

assumption of orthogonality between core and valence electron wavefunctions and hence require a vast plane wave basis set.

A way of bypassing this problem is a separate treatment of core and valence electrons since the latter ones are mainly responsible for chemical processes. The core electrons are excluded in the electronic consideration and approximated with effective potentials. Two concepts of effective potentials, the pseudopotentials and the combined approach of the projector augmented wave method, are briefly introduced in the next section.

3.4. Pseudopotentials and projector augmented wave method

To avoid the problem of an unmanageably large number of basis functions in the plane wave approach, the Coulomb core-potential as well as the tight bound core electrons are fixed and substituted via an effective potential $\mathcal{V}_{pseudo}$ (pseudopotential), such that the corresponding valence-electron pseudo wavefunction ϕ_{pseudo} is represented by a smooth and nodeless function in the core area $r < r_c$ and matches the all-electron wavefunction ϕ for $r \geq r_c$ (frozen-core approximation). Since the fusion of nuclei and core-close electrons in a single core is determined by a particular state such as a single atom, this approach is called the frozen-core approximation.

The approximation of the potential and the corresponding pseudo wavefunction are shown schematically in Figure 3.5. Notably, pseudopotentials have to be generated with the same exchange-correlation functional that is used in further calculations. However, the choice of pseu-

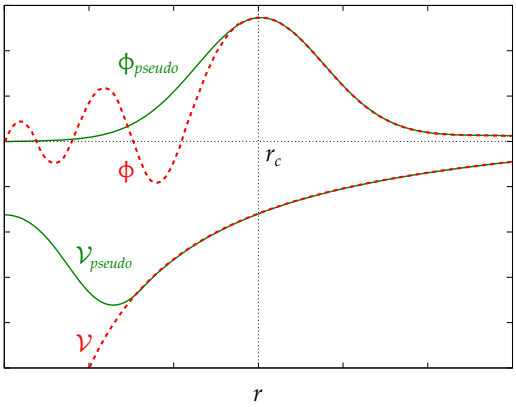

Figure 3.5.: Approximation of the all-electron potential and wavefunction (red) via a pseudopotential and pseudo wavefunction (green) up to a core radius r_c (adapted from ref. 73).

dopotentials is not unique due to the variety of functionals as well as the freedom of core area restriction . Nonetheless, conservation of scattering properties have to be ensured for all choices of approximations to guarantee transferability, i. e., the application of the same potential in different environments in a variety of molecules and crystal structures.

Two general classes of pseudopotentials are distinguished, the norm-conserving and the ultrasoft pseudopotentials developed by Vanderbilt.[74] While the first provide the possibility to reproduce the charge density of the all-electron system, simultaneously norm-conserving pseudopotentials require a high number of plane waves to ensure this quality. In the case of ultrasoft pseudopotentials the assumption of norm-conservation is relaxed in favor of even smoother wavefunctions and a significantly lower number of plane waves, however, at the expense of orthogonality of the wavefunctions.

The projector augmented wave (PAW) method developed by Blöchl[75] is a combination of the pseudopotential approach and the linear augmented plane wave method. Starting point is a "muffin-tin" approach in which we separate the system in a defined augmented region around every atom and an interstice. The potential arising from the nucleus is given by a spherically symmetric function in the augmented region and is constant outside. In the interstitial region all-electron wavefunctions are used, while smooth pseudo wavefunctions are applied in the augmented region and expanded in terms of plane waves. All-electron wave functions and pseudo wavefunctions are related via a linear transformation $\mathcal{T}$. The transformation acts solely in the augmented region, such that the pseudo wavefunctions are mapped onto the all-electron wavefunctions in the augmented region via

$$|\phi\rangle = \mathcal{T}|\phi_{pseudo}\rangle = 1 + \sum_i \left(|\phi_i\rangle - \langle\phi_{i,pseudo}|\right)\langle p_i| \ ,$$

but remain identically equal to the all-electron wavefunctions in the interstitial region. Here, $|\phi_i\rangle$ is a basis set in the augmented region (solutions of the radial Schrödinger equation for an isolated atom), $|\phi_{i,pseudo}\rangle$ is the smooth basis set (plane waves) generated using the linear transformation on $|\phi_i\rangle$, and $|p_i\rangle$ is a projector function with $\langle p_i|\phi_{j,pseudo}\rangle = \delta_{ij}$.

In summary, the PAW method provides an access to the entire all-electron wavefunction and charge density and hence avoids transferability problems. Furthermore, the energy cutoff for the plane wave expansion is comparable to the approach of ultrasoft pseudopotentials. Thus, within the frozen-core approximation the PAW method provides the accuracy of an all-electron method with simultaneous reasonable computational effort.

CHAPTER 4

COMPUTATIONAL DETAILS AND SYSTEM VALIDATION

In the following chapter we introduce the framework for the applied computational methods, DFT-based and classical molecular dynamics simulations. A benchmark test for the DFT-based LAUTREC (LAUsanne Total REal to Complex energy) code as well as all performed calculations and their system parametrization are summarized in a brief manner. This is followed by the results of preliminary system tests of solvents and bulk crystalline structures.

4.1. Density functional theory based simulations

All first-principles molecular dynamics simulations are carried out within density functional theory using the Car-Parrinello method[60] based on special algorithms developed for metallic systems,[61,62] as implemented in the LAUTREC code.[76] The PW91 generalized gradient approximation[70] is used for the exchange-correlation functional and the PAW method[75] to describe the electron-core interactions. The PAW data sets for lithium and oxygen are generated with valence states of 1s2s and 2s2p, respectively. The wave functions are expanded in plane-waves up to a kinetic energy of about 40 Ry (540 eV). Convergence criteria are set to 10^{-5} eV for the total energy and to 0.05 eV Å^{-1} for all force components in the geometry relaxations.

The parallel scaling behavior of the LAUTREC code is shown in Figure 4.1. The parallelization technique is based on the programming interface Message Passing Interface (MPI) and explained more detailed in Section 9.5. Parallel calculations are performed distributing k-points as well

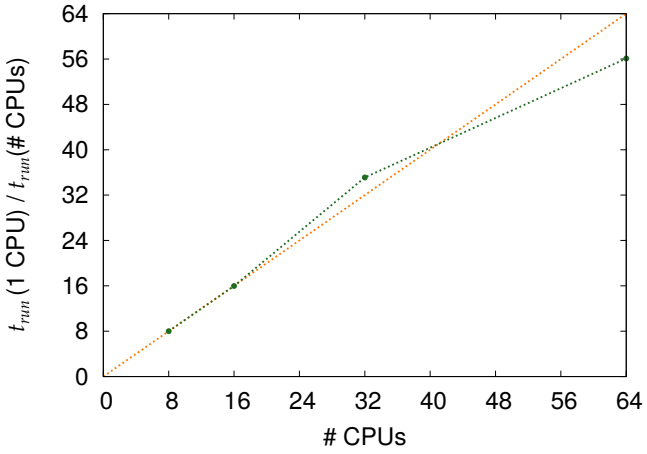

Figure 4.1.: Scaling behavior of the LAUTREC code (green) with respect to the number of CPUs in comparison to an ideal linear scaling (orange).

reciprocal space vectors uniformly on the individual CPUs. Up to 32 CPUs the LAUTREC code shows an excellent scaling and decreases not until 64 CPUs below the ideal linear behavior. The performance drop is originated in the decreasing speed in communication, synchronization, and exchange of data files between single nodes (4 or 8 CPUs) with increasing number of cores involved in the calculation.

Total energy calculations of bulk crystal structures of metallic Li, Li_2O, and Li_2O_2 are carried out using k-point distributions of $4\times4\times4$, $4\times4\times4$, and $4\times4\times2$ in the smallest unit cells, respectively. Li surfaces in presence of 11 PC and 13 DMSO molecules and Li_2O_2 surfaces in presence of 8 PC and 10 DMSO molecules are carried out using a Γ-point calculation only. Slabs with surfaces in z-direction are built according to $3a\times3a\times3.5a$ in units of the cubic Li unit cell with a total cell length of 34.51 Å including the vacuum and $3a\times3a\times2c$ in units of the hexagonal Li_2O_2 unit cell with an O-termination on each surface and a total cell length of 34.72 Å including the vacuum. The structures of the solvent molecules are previously optimized using classical molecular dynamics simulations (see Section 4.2).

A Fermi-Dirac distribution is applied to the occupation of the electronic states for metallic systems according to a smearing energy of 0.1 eV. Small Li_nO_n clusters are simulated in a cubic cell of 10 Å edge length using the Γ-point only. In order to determine their correct magnetic state, both spin-restricted (triplet and singlet) and spin-unrestricted calculations with additional empty states corresponding to 50-70 % of the occupied states are performed. In the spin-restricted calculations the electronic occupations of each spin manifold are kept fixed to force the system in a given spin state, In the unrestricted case, the occupancies are free to change the self-consistent energy minimization loop. The dynamical simulations of the decomposition of Li_8O_8 clusters in vacuum

upon removal of one and two electrons are performed in a larger cubic cell of 15 Å edge length, in order to avoid interaction of the decomposition products with their periodic images. Charges and spin moments are calculated using a Bader analysis[77] of the electron density and of the spin density of each system, respectively.

The DFT-based simulations of the Li_8O_8 cluster decomposition in DMSO solvent are performed in an even larger cubic cell of 17 Å edge length, in which the structure of the solvent molecules is previously optimized using classical molecular dynamics simulations. The cell contains 41 DMSO molecules which corresponds to a density of 1.08 g cm^{-3}, to be compared with an experimental value of 1.09 g cm^{-3} at 300 K.[78] The energetically most favored Li_8O_8 cluster is then inserted in the center of the cell, replacing two DMSO molecules whose molecular volume corresponds roughly to the molecular volume of the Li_8O_8 cluster (240 Å^3 vs 220 Å^3). Prior to the DFT-based simulations each lasting about 14 ps, the solvent is relaxed classically around the fixed cluster for 2 ns.

4.2. Classical molecular dynamics simulations

All classical molecular dynamics simulations are carried out using the LAMMPS (Large-scale Atomic/Molecular Massively Parallel Simulator) package.[79] The total energy is represented by standard Lennard-Jones and Coulomb potentials for the intermolecular interactions and harmonic bond-stretching, angle-bending, and torsional potentials for the intramolecular interactions according to

$$E = \frac{1}{2} \sum_{\substack{i,j \\ \text{nonbonded}}} \left\{ \frac{q_i q_j}{4\pi\epsilon_0 r_{ij}} + 4\epsilon_{ij} \left[\left(\frac{\sigma_{ij}}{r_{ij}} \right)^{12} - \left(\frac{\sigma_{ij}}{r_{ij}} \right)^{6} \right] \right\} + \sum_{\text{bonds}} k_b (b - b_0)^2 + \sum_{\text{angles}} k_\theta (\theta - \theta_0)^2 + \sum_{\text{dihedrals}} k_\phi [1 + \cos(n\phi - d)]^2 \,, \tag{4.1}$$

where b, θ, and ϕ are the bond distance, the bond angle, and the dihedral angle, b_0 , θ_0, ϕ_0, and d their equilibrium values and k_b , k_θ, and k_ϕ the corresponding force constants. The distance between site i and j in two different molecules is denoted by r_{ij} and the Lennard-Jones parameters are determined by the Lorentz-Berthelot mixing rule applied to atom-specific parameters

$$\epsilon_{ij} = (\epsilon_i \epsilon_j)^{\frac{1}{2}}, \quad \sigma_{ij} = \frac{1}{2}(\sigma_i + \sigma_j) \,.$$

The simulation parameters for DMSO are taken from ref. 80, for PC from ref. 81–83, for lithium ions from ref. 84 and for molecular oxygen from ref. 85. All parameters are summarizes in Appendix A, Tables A.1 and A.2.

The structure of the liquid DMSO solvent in the absence and presence of Li^+ ions and dissolved O_2 molecules is simulated in cubic cells of about 36 Å edge length, containing 410 molecules of DMSO, 30 additional Li^+ ions, or 30 additional O_2 molecules. All systems are initially equilibrated in an NVE ensemble for 200 ps and in an NPT ensemble for 6 ns at a temperature of 300 K and an isotropic pressure of 1.0 atm using an integration time step of 2 fs. The temperature is relaxed in a time span of 100 ps and the pressure in a time span of 500 ps. Comparison of the classical results with DFT-based simulations is performed in smaller cells of 17 Å edge length containing 41 DMSO molecules (see previous section), alone and in the presence of three lithium ions or three oxygen molecules. In this case, a classical NVE MD simulation is run for 200 ps, followed by a DFT-based simulation for about 6 ps at a temperature of about 300 K. Classical relaxation of the solvent around a Li_8O_8 cluster is performed in the same smaller cell in an NVT ensemble for 2 ns at a temperature of 300 K, while the cluster is geometrically fixed.

4.3. Bulk Li metal, oxide and peroxide structures

Lattice parameters and energies of formation of Li, Li_2O, and Li_2O_2 bulk structures are analyzed in order to validate the framework of DFT parameters and pseudopotentials. At room temperature and low pressures metallic Li crystallizes in a bcc structure (space group: $Im\bar{3}m$)[86] and Li_2O in a cubic antifluorite structure (space group: $Fm\bar{3}m$),[87] where every lithium ion is tetrahedrally coordinated by oxygen atoms which are placed on a fcc sublattice.[88] Li_2O_2 assumes a Föppl structure[89] based on a hexagonal crystal lattice (space group: $P6_3/mmc$), as verified experimentally and computationally.[90,91]

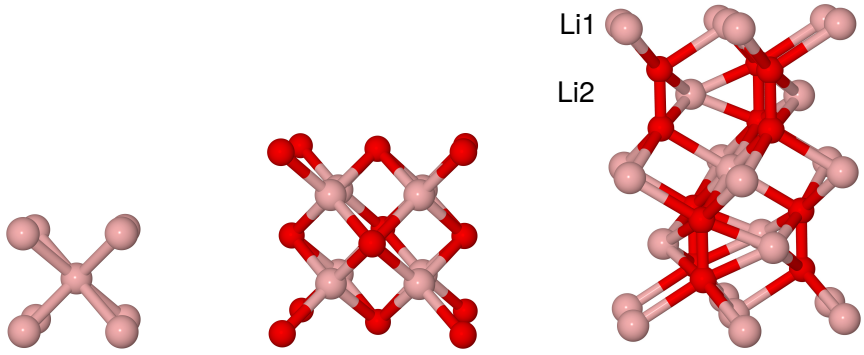

Figure 4.2.: Bulk Li, Li_2O, and Li_2O_2 with lithium (pink) and oxygen (red).

The equilibrium lattice constants are obtained from a fit of the total energy of the relaxed crystal structures (Figure 4.2) based on the Murnaghan equation of state[72] and are reported in Table 4.1. All results are in good agreement with available experimental data as well as other DFT-based calculations.

Table 4.1.: Lattice parameters for bulk Li, Li_2O, and Li_2O_2 and energy of formation at zero temperature per Li atom, ΔG_f, with respect to bulk lithium and atomic oxygen. Other DFT-based calculations are carried out using the PAW method, the PBE-GGA functional, a kinetic energy cutoff of 430 eV, and a $9\times9\times9$ k-point grid.[54]

		this work	other calculations	exp.
Li	a / Å	3.45	3.45	3.49[71]
Li_2O	a / Å	4.63	4.62	4.61[92]
	ΔG_f / eV	-3.08	-3.16	-3.06[93]
Li_2O_2	a / Å	3.16	3.14	3.14 (Föppl)[89]
	c/a	2.42	2.43	2.44 (Föppl)[89]
	ΔG_f / eV	-3.38	-3.26	-3.36[93]

The Gibbs free energies of formation of Li oxide and peroxide at a pressure of 1 atm are calculated for different temperatures via

$$\Delta G_f = E^{\text{bulk}}_{\text{Li}_2\text{O}_{(2)}}(N_{\text{Li}}, N_{\text{O}}) - N_{\text{Li}}\mu_{\text{Li}} - N_{\text{O}}\mu_{\text{O}} \ ,$$

where $N_\bullet$ is the number of atoms and $E^{\text{bulk}}_\bullet$ is the total energy of the bulk structure. In so doing, we assume entropic effects to be associated only with O_2 gas and neglect the differences in zero-point energy of the bulk phases. Moreover, the chemical potentials are assumed to be

$$\mu_{\text{Li}} \approx E^{\text{bulk}}_{\text{Li}}$$

and

$$\mu_{\text{O}}(T,p) \approx \frac{1}{2}\left(2E^{\text{gas}}_{\text{O}} - E^{\text{bind}}_{\text{O}_2}\right) + \frac{1}{2}k_B T \ln\left(\frac{p}{p_0}\right) + \mu_{\text{O}}(T,p_0) \ ,$$

where

$$\mu_{\text{O}}(T,p_0) = \frac{1}{2}\left[H_{\text{O}_2}(T,p_0) - H_{\text{O}_2}(0\,\text{K},p_0) - T(S_{\text{O}_2}(T,p_0) - S_{\text{O}_2}(0\,\text{K},p_0))\right] \ .$$

The enthalpy H_{O_2} and the entropy S_{O_2} are taken from ref. 93 and the binding energy of molecular oxygen $E^{\text{bind}}_{\text{O}_2} = 5.18\,\text{eV}$ from ref. 94.

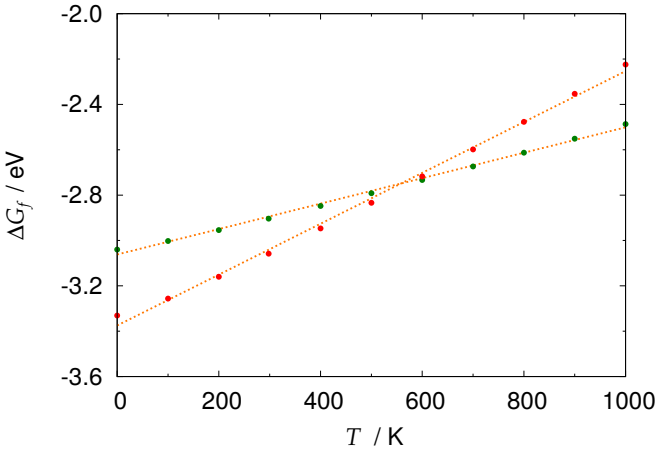

Figure 4.3.: Gibbs free energy of formation per Li atom as a function of temperature for Li_2O_2 (red) and Li_2O (green) and best-fit lines of the linear regression in orange (in both cases the correlation coefficient is $r = 0.9984$).

The calculated Gibbs free energies of formation as a function of temperature for both oxides are shown in Figure 4.3. For a better visualization of the relative stability of the bulk phases at different temperatures as well as a verification of the transition-point temperature with experimental results a linear regression has been applied on the data. At the working temperature of a lithium/air battery of 298 K the Gibbs free energy of formation of lithium peroxide is below the one of lithium oxide with an energy difference of about 0.15 eV per lithium atom. A change in stability occurs at a temperature of 595(36) K, to be compared with an experimental value for the thermal decomposition of Li_2O_2 of 570 K.[95] While these results apply for the case of pure oxygen gas, it should be taken into account that at an atmospheric pressure of 1 atm and a temperature of 298 K the oxygen solubility in $DMSO^{Li^+}$ is $2.1 \cdot 10^{-6}$ mol cm^{-3}.[96] When the reduced oxygen concentration is taken into account according to Henry's law, the energy difference between oxide and peroxide at 298 K is only slightly reduced to 0.12 eV per Li atom, confirming that Li_2O_2 remains the more stable phase in the working pressure and temperature regime of Li/air batteries.

4.4. Solvent: DMSO vs PC

The stability of the solvents PC, which has been widely used in the first attempts to Li/air batteries, and DMSO are tested on the (001) Li surface as well as on the O-rich (0001) Li_2O_2 surface. The choice of the O-rich (0001) Li_2O_2 surface is determined by preliminary studies on the stability of Li_2O_2 surfaces and has been found to be the most stable low Miller index surface. All analyzed surfaces with different terminations and stoichiometries and their corresponding surface energies

can be found in the Appendix in Figure B.1 and Table B.1. Figure 4.4 shows (a) DMSO and (b) PC solvent in contact with metallic lithium in the initial configuration and after a MD simulation at about 300 K.

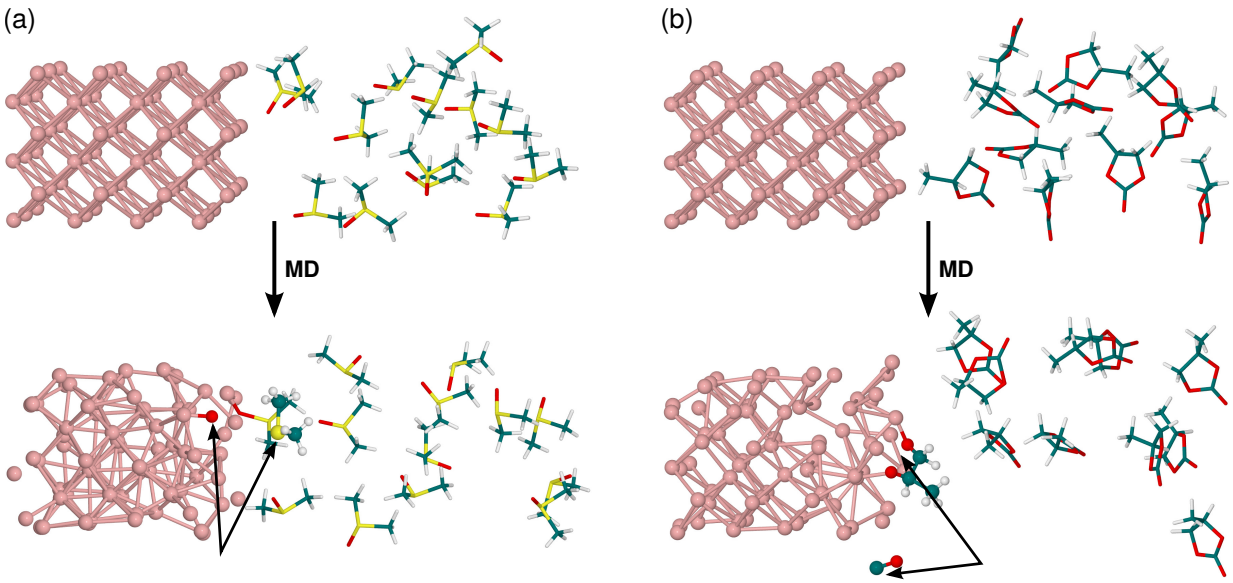

Figure 4.4.: (a) DMSO and (b) PC on the (001) Li surface in the initial state and after a MD simulation at 300 K.

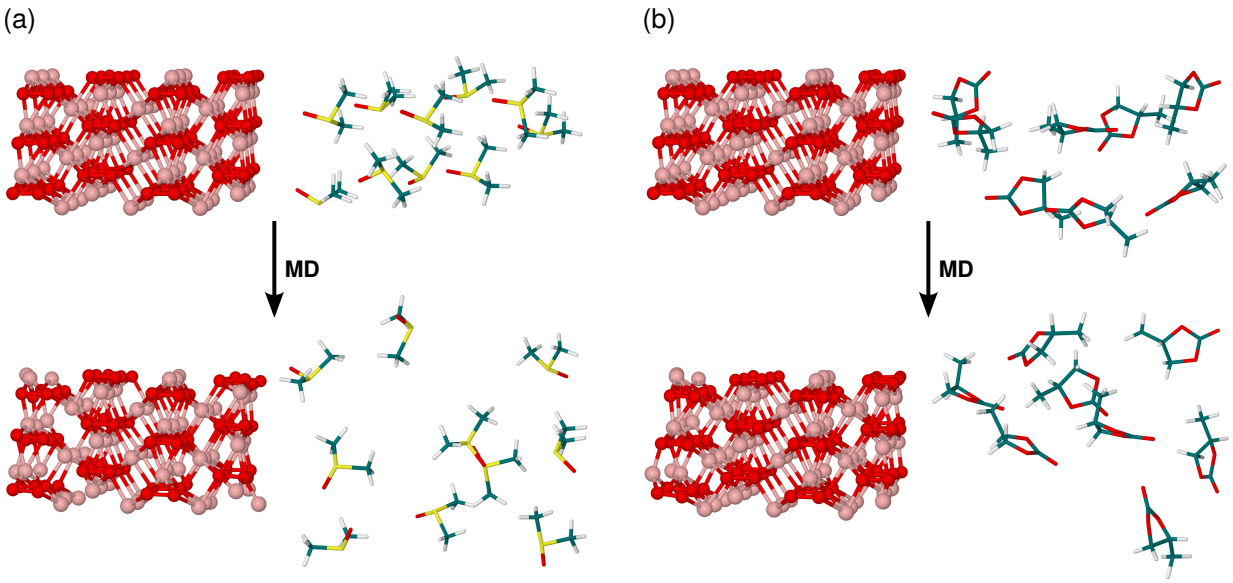

Figure 4.5.: (a) DMSO and (b) PC on the O-rich (0001) Li_2O_2 surface in the initial state and after a MD simulation at 300 K.

According to expectations, both solvents undergo a decomposition process, as can be seen in the splitting of the DMSO-O after about 0.6 ps and a CO unit in the case of PC after about 0.9 ps at the Li surface. The same procedure is repeated at the O-rich (0001) Li_2O_2 surface and is shown in Figure 4.5 for (a) DMSO and (b) PC. In the performed MD simulation of 10 - 12 ps at 300 K no spontaneous decomposition has been observed, neither for DMSO nor for PC. This is in contrast to a spontaneous ring opening of PC observed by Laino et al.[97] after a few ps in a similar simulation of PC on the O-rich $(10\bar{1}0)$ Li_2O_2 surface performed with the CP2K code.[98]

Although we can not confirm the role of bulk Li_2O_2 as a degrading agent for the solvent, we do not exclude the possibility of a spontaneous decomposition which could not have been observed due to a too short simulation time. Nonetheless, according to our simulations, both solvents are stable in the performed simulation time and environment.

4.5. DMSO Solvent: Radial distribution function

The intermolecular radial distribution functions of pure liquid DMSO and of the reaction products of the charge process Li^+ and O_2 dissolved in DMSO are obtained from classical and DFT-based MD simulations and shown in Figure 4.6. In the latter two cases the integrals of the radial distribution functions, which determine the number of DMSO molecules coordinating Li^+ and O_2, are also presented. The radial distribution function $g(r)$ between two particles X and Y denotes the number density of particle Y at a distance r to particle X, i. e. between DMSO-O and Li^+ or DMSO-CH_3 and O_2. In the case of pure DMSO the intermolecular atom-atom pair distribution functions $S-S$, $O-O$, $C-C$, $S-O$, $S-C$ and $O-C$ are added up using the same weights as in the neutron diffraction experiments from Luzar et al.[99].

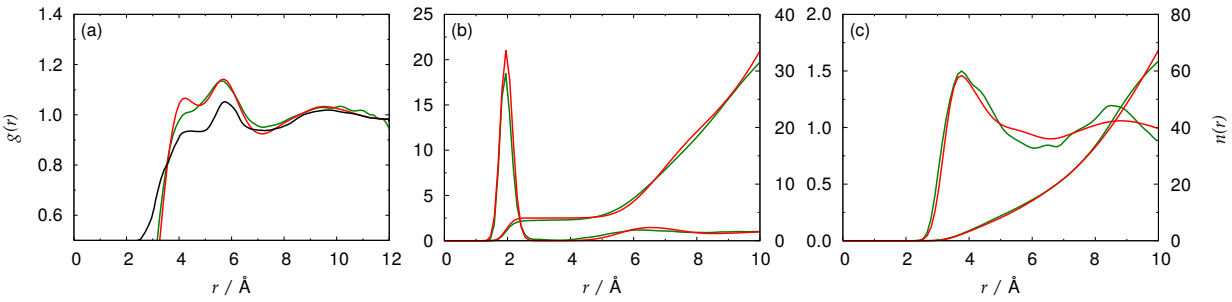

Figure 4.6.: Radial distribution functions $g(r)$ of (a) DMSO, (b) Li^+ in DMSO and (c) O_2 in DMSO with corresponding integrals $n(r)$ performed with LAMMPS (red) and LAUTREC (green). Experimental results for DMSO[99] are shown in black.

Although slightly different in the absolute intensity for $r < 7$ Å, there is a good agreement of our results with the experimental data concerning the peak positions and the overall shape of the curves. The first peak position and the number of DMSO molecules in the first coordination shell of the dissolved Li^+ and O_2 species are shown in Table 4.2 in comparison with other calculations and experimental results.

Table 4.2.: Peak position r_1 and number of molecules in the first coordination shell n_1 for Li^+ and O_2 in DMSO. Experimental values and other classical MD calculations are taken from Megyes et. al.[100]

	this work		other calculations		exp.
	DFT	Class. MD	DFT[101]	Class. MD.	
$r_1(Li^+)$ / Å	1.95	1.95	1.96	1.93;[102] 1.98	2.02
$n_1(Li^+)$	3.70	4.02	4.00	4.00	4.10
$r_1(O_2)$ / Å	3.76	3.79			
$n_1(O_2)$	8.34	8.06			

The Li^+ ion is faced by oxygen atoms of DMSO at a distance of about 2 Å with an overall coordination number of four molecules. The coordination number obtained from the DFT-based simulation is 3.7, probably due to the shorter simulation time than in the classical simulations. The oxygen molecule is faced by the methyl groups of eight DMSO molecules, at an average distance of about 3.8 Å. The self-diffusion coefficient of DMSO and the diffusion coefficients of Li^+ and O_2 are calculated from the performed MD simulations based on the mean square displacement (MSD)

$$\text{MSD} = \langle (\boldsymbol{x}(t) - \boldsymbol{x}_0)^2 \rangle = 2Dt \ ,$$

where $\boldsymbol{x}(t)$ is the molecule position at time t and $\boldsymbol{x}_0$ the initial position. The results are reported in Table 4.3 and agree well with available experimental values.

Table 4.3.: Diffusion coefficients in DMSO carried out with classical MD simulations; experimental values for D_{O_2} performed by Laoire et al.[7] are obtained in 0.1 M $LiPF_6$-DMSO and by Fujinaga et al.[103] in 0.1 M $(Et)_4NClO_4$-DMSO, for D_{Li^+} in 0.1 M $LiPF_6$-DMSO.

D / 10^{-6} cm^2 s^{-1}	this work	exp.
D_{DMSO}	7.70	8.00[104]
D_{O_2}	22.60	16.70;[7] 27.00[103]
D_{Li^+}	3.05	3.33[105]

In summary, both the classical and the DFT-based MD simulations are able to reproduce the correct behavior of liquid DMSO at 300 K. Therefore, we can rely on classical simulations to initially optimize the distribution of DMSO molecules around Li_2O_2 clusters before performing DFT-based studies of their decomposition due to oxidation processes. However, before doing that, in the next chapter we first investigate the atomic and electronic structures of Li_2O_2 clusters and their oxidation behavior in vacuo.

CHAPTER 5

RESULTS

In the present chapter we present the results of the study of amorphous Li_nO_n clusters which are generated to model amorphous peroxide phases in actual Li/air batteries. Following this, the decomposition of Li_2O_2 taking place during the charge process is studied in vacuo and in the solvent DMSO via a DFT-based dynamic simulation. Furthermore, we analyze the geometrical as well as electronic properties of the resulting structures and decomposed species using a Bader charge and a density of states (DOS) analysis and interpret these in terms of possible reaction mechanisms for the charge process in Li/air batteries.

5.1. Li_nO_n clusters

Possible structures of lithium peroxide clusters Li_nO_n are investigated in spin-restricted (triplet and spin-paired states) as well as spin-unrestricted DFT-based simulations performed starting from three different initial conditions. These correspond to (i) a portion of a bulk lithium peroxide structure, (ii) randomly distributed lithium atoms and oxygen molecules with 2:1 stoichiometry, and (iii) randomly distributed lithium and oxygen atoms with 2:2 stoichiometry. All initial structures are first annealed in DFT-based simulations at 300 K lasting 1 to 10 ps depending on the size of the system and eventually fully relaxed via geometry optimization. None of the obtained ground states in spin-unpaired calculations present magnetization of single atoms and an overall singlet character of the whole system (total spin zero), so that in the following we can refer to singlet and triplet states only. The optimized structures of lowest energy for all sizes n = 2, 4, 6, 8 and for both spin states are shown in Figure 5.1 together with the corresponding Bader atomic charges, lengths

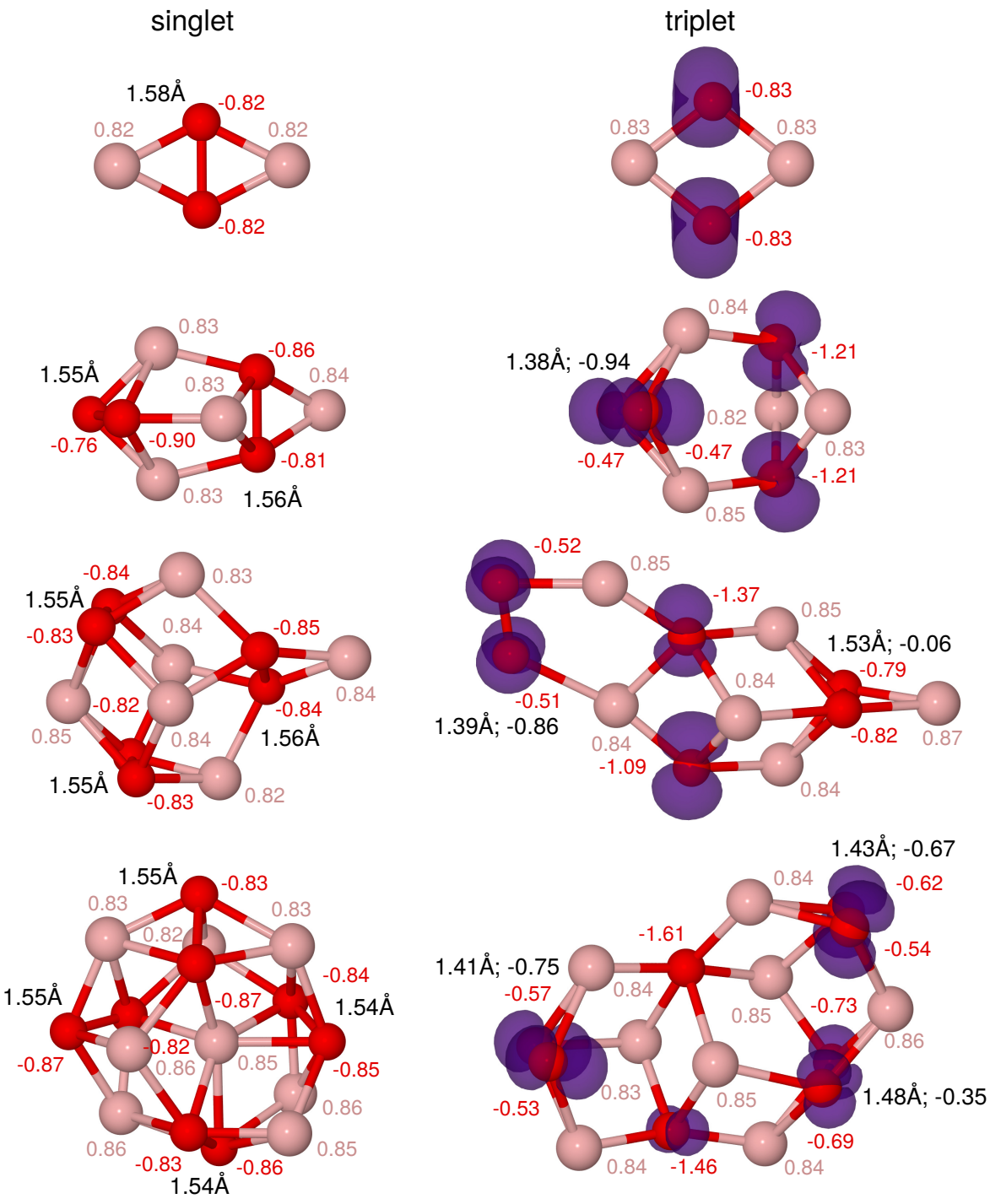

Figure 5.1.: Lowest-energy structures of Li_nO_n clusters in singlet (left) and triplet (right) electronic configurations along with the Bader atomic charges in e (same color as the atom type), O — O bond lengths, and spin moments on O — O pairs (black), and their spin densities (blue isosurfaces).

of O — O bonds, and spin moments on the O — O bonded pairs (in the case of triplet states). Both the obtained geometries and the O — O bond lengths are in good agreement with the results of similar DFT-based simulations performed by Lau et al.[106] Also, the values of atomic charges and spin moments are comparable, although a Mulliken analysis is used in ref. 106, while a Bader analysis is performed in the present work. Differences in the equilibrium geometries obtained here and in ref. 106 are due to very small energy differences among different structures (all computed structures and their relative energies are reported in Appendix C, Figures C.1-C.5 and Table C.1).

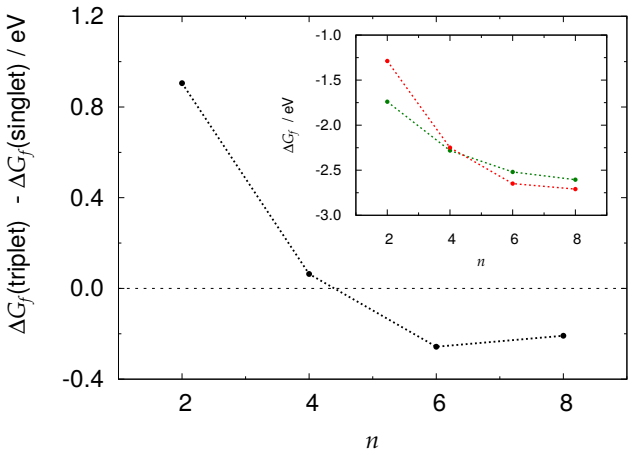

Figure 5.2.: Difference in Gibbs free energies of formation between a singlet and a triplet state; energies per lithium atom of singlet (red) states and triplet (green) states are given explicitly in the inlay.

The Gibbs energies of formation of the lowest-energy clusters in the singlet and triplet states as well as the energy difference between the two states are reported in Figure 5.2 as a function of the cluster size. Triplet spin states are favored for Li nuclearities larger than n = 4, which is in good agreement with the results of Lau et al.[106] In the spin-paired configurations the O — O bond lengths are between 1.54 Å and 1.58 Å with an average O charge of -0.84 e, to be compared with a distance of 1.58 Å and a charge of -0.82 e calculated in bulk lithium peroxide. Despite of the 2:2 Li:O stoichiometry, clusters in the spin-triplet configuration present O — O bonds of peroxide, superoxide and intermediate peroxide/superoxide character. Namely, the distances vary from 1.38 Å to 1.53 Å, the charges from -0.47 to -0.81 e, and the absolute spin moments from 0.94 to 0.06 μ_B, to be compared with the peroxide values reported above and the superoxide values computed for an isolated LiO_2 molecule: 1.37 Å, -0.42 e and 1.00 μ_B, respectively. Notably, both unrestricted spin calculations and spin-restricted calculations with total spin values higher than 2.0 confirm that the actual ground state of larger clusters is a triplet. This is an an initial hint that the surfaces of deposited amorphous Li_2O_2 phases in Li/air batteries may present a partial

superoxide character in spite of an overall 2:2 stoichiometry. To investigate whether the same order of stability of Li_2O_2 and Li_2O at the working temperature of Li/air batteries also applies in the case of small clusters, Li_8O_4 clusters are generated in spin-unrestricted DFT-based simulations starting from three different initial conditions, either from a Li_2O crystal or from randomly placed Li and O atoms or molecules with 4:1 or 2:1 stoichiometry. The Gibbs free energies of formation as a function of temperature are then compared with that of the energetically most favored Li_8O_8 cluster (Appendix C, Figures C.6 and C.7 and Table C.2). These indicate a higher stability of the peroxide with respect to oxide phases also in the case of clusters, with an energy difference between the Li_8O_4 and the Li_8O_8 clusters at 298 K varying between 0.34 and 0.53 eV per Li atom, depending on the initial condition.

5.2. Cluster decomposition in vacuum

In a next step, starting from the most stable Li_8O_8 cluster in its ground-state triplet configuration in vacuo, either one or two electrons are removed from the system and two DFT-based simulations at 300 K lasting about 2 ps are performed, followed by geometry relaxations. The obtained systems are reported in Figure 5.3 along with the $O-O$ bond lengths, charges, and $O-O$ spin moments, both after the initial electron minimization before the dynamics and after the dynamics and relaxation. After removal of one single electron, the cluster remains in a similar geometry with an energy gain of -0.27 eV associated with the structural relaxation. Two of the three $O-O$ bonds shorten to distances of about 1.38 Å and increase their spin moment to about 1.0, thus, becoming clearly of superoxide type.

After removal of two electrons, an oxygen molecule with a bond length of 1.22 Å, a mean oxygen charge of 0.04 e, and an absolute spin moment of 1.93 is released from the cluster, according to the formal reaction

$$Li_8O_8 \longrightarrow [Li_8O_6]^{2+} + O_2 + 2e^- \ .$$

The energy difference associated with the partial decomposition after removal of two electrons is -1.52 eV. The $O-O$ pairs remaining in the cluster shorten their distances to 1.37 Å and 1.38 Å, respectively, and assume an average O charge of about -0.45 e. This is indicative of a superoxide bond, although the $[Li_8O_6]^{2+}$ cluster ends up in a spin-paired configuration. Separate electron minimizations of this cluster structure with spin constraints indeed reveal that the triplet configuration is slightly higher in energy, although by less than 0.02 eV. We could think of the reaction product as a Li_6O_6 cluster with two electrostatically bound Li^+ ions. However, it should be noted that the two singly-coordinated Li atoms present the same Bader charge (0.87 e) as all

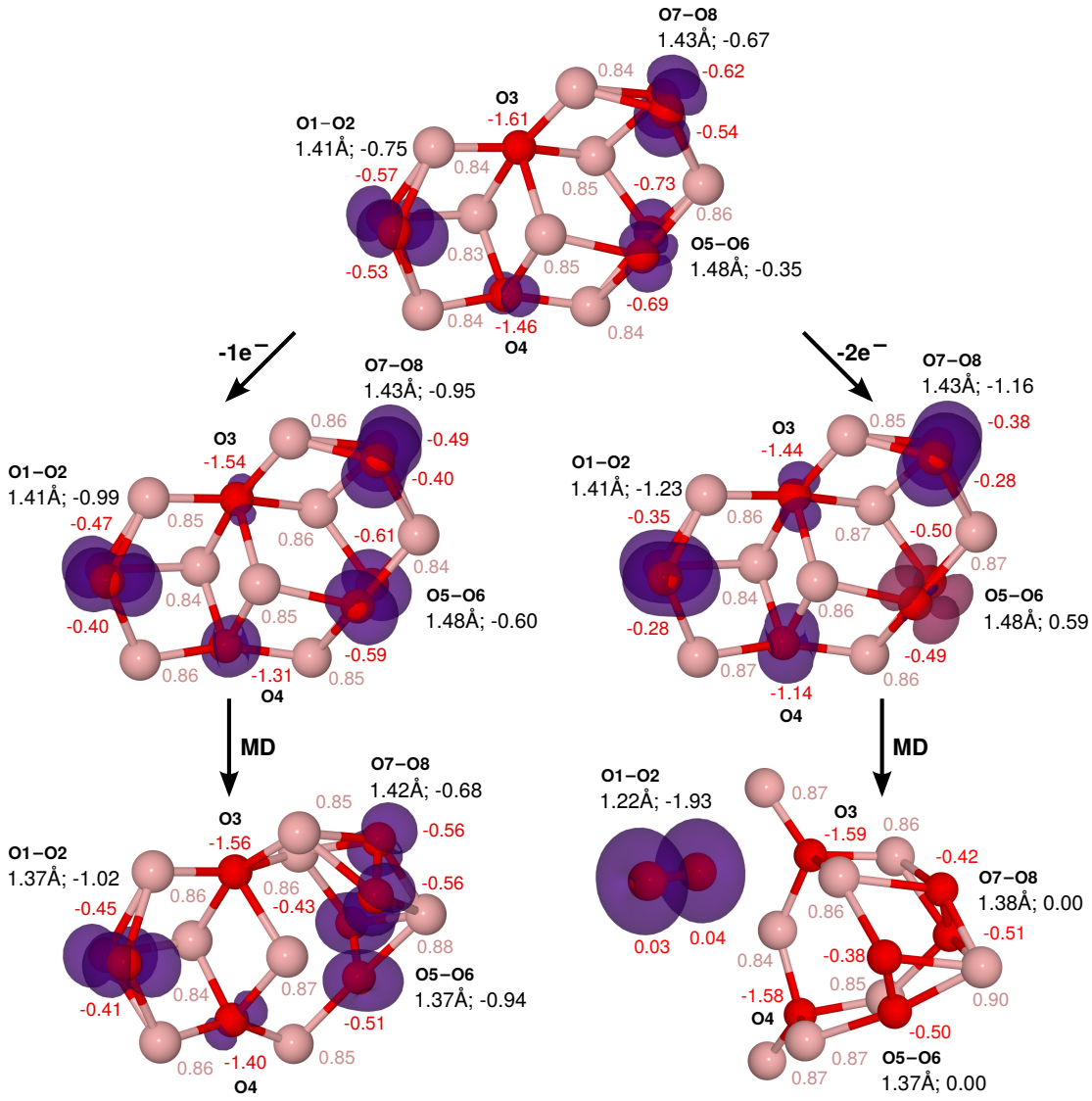

Figure 5.3.: Snapshots of DFT-based MD simulations of a Li_8O_8 cluster in vacuo after removal of one and two electrons with Bader atomic charges in e (same color as the atom type), $O-O$ bond lengths and spin moments on $O-O$ pairs (black), and their spin densities (blue and purple isosurfaces).

other Li atoms, so that they cannot be differentiated on the basis of electron-structure arguments.

To ensure that the release of an oxygen molecule after removal of only one electron is not hindered by an activation barrier, we compute the total energy of an alternative structure, in which the $O1-O2$ pair is forceably detached from the cluster and placed at a distance of about 5.7 Å far from it. After a short MD simulation of about 1 ps and a subsequent geometry relaxation, the obtained energy is 0.58 eV higher than before O_2 detachment, confirming that the release of dioxygen is clearly not favored unless two electrons are removed from the system.

5.3. Cluster decomposition in DMSO

In order to study the influence of solvent on the OER process, MD simulations after electron removal from the most stable Li_8O_8 cluster are performed in the presence of DMSO. To this aim, the cluster is placed in a cell filled with DMSO molecules which are initially relaxed by means of classical MD simulations as described in the Computational Details section. After that, DFT-based simulations with the system deprived of either one or two electrons are started ((Figures 5.4 and 5.5)). As in the absence of solvent, removal of a single electron does not result in any dramatic structural changes. Mobility of the $O-O$ pairs is evident, though, leading to the $O5-O6$ and $O7-O8$ pairs switching their positions. Nonetheless, the overall geometry of the cluster remains stable and no decomposition is observed in a total of 15 ps of simulation, after which the dynamics is stopped and the atomic positions fully relaxed. In the optimized final structure, the $O-O$ bond lengths are 1.34, 1.39, and 1.40 Å, the absolute spin moments are 1.07, 0.78, and 0.73, and the O Bader charges are between -0.41 e and -0.53 e which implies $O-O$ bonds of superoxide type.

The evolution of the system is markedly different after removal of two electrons. In this case, the $O1-O2$ pair is repeatedly observed to temporarily detach from the cluster and is eventually able to leave it irreversibly after about 10 ps of simulation time. Upon completion of the dynamics after 15 ps, the O_2 molecule released into the solvent presents a bond length of 1.27 Å, an absolute spin moment of 1.61, and an average charge of -0.18 e which are fully consistent with molecular dioxygen. Regarding the other two $O-O$ pairs, one of them is clearly of superoxide type (bond length 1.38 Å, spin moment 0.83, and O charge -0.48 e), while the second shows also a trend toward molecular dioxygen (1.31 Å, -1.36, -0.27 e) which is different from the vacuum case (two remaining superoxide bonds).

To obtain a further, statistically independent trajectory, we perform a second DFT-based simulation starting from a snapshot of the previous run after 8 ps of simulation. After an initial randomization of the atom velocities and a brief thermalization to reach 300 K, the dynamics follows

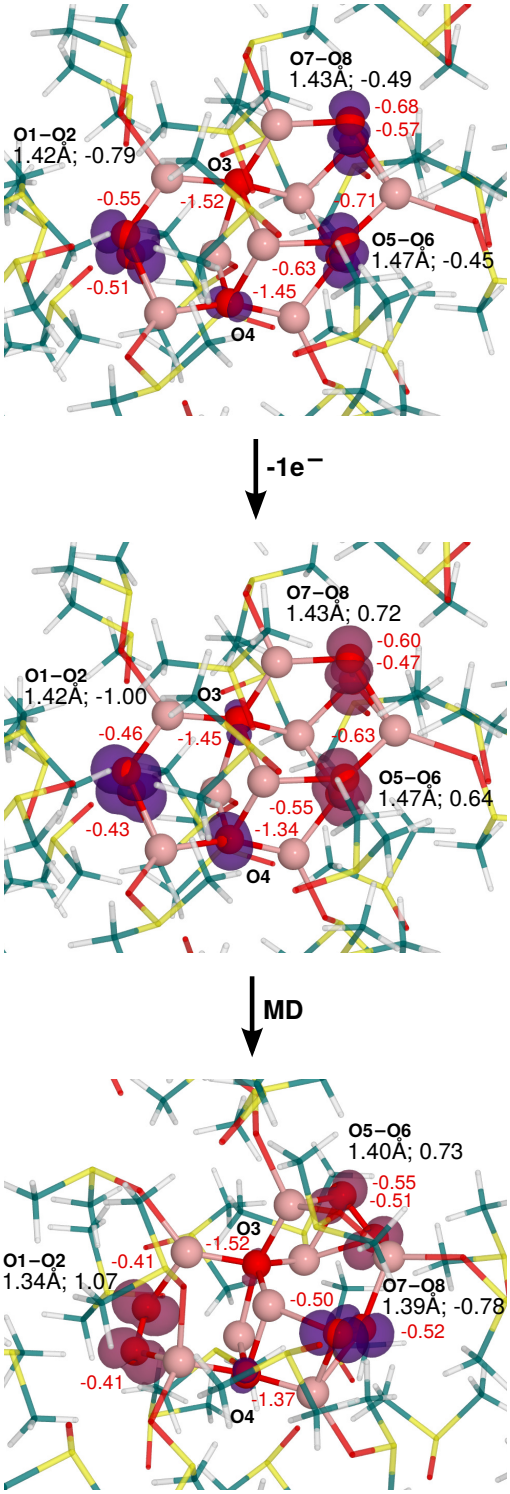

Figure 5.4.: Snapshots of DFT-based MD simulations of a Li_8O_8 cluster in DMSO after removal of one electron with Bader atomic charges in e (same color as the atom type), O − O bond lengths and spin moments on O − O pairs (black), and their spin densities (blue and purple isosurfaces).

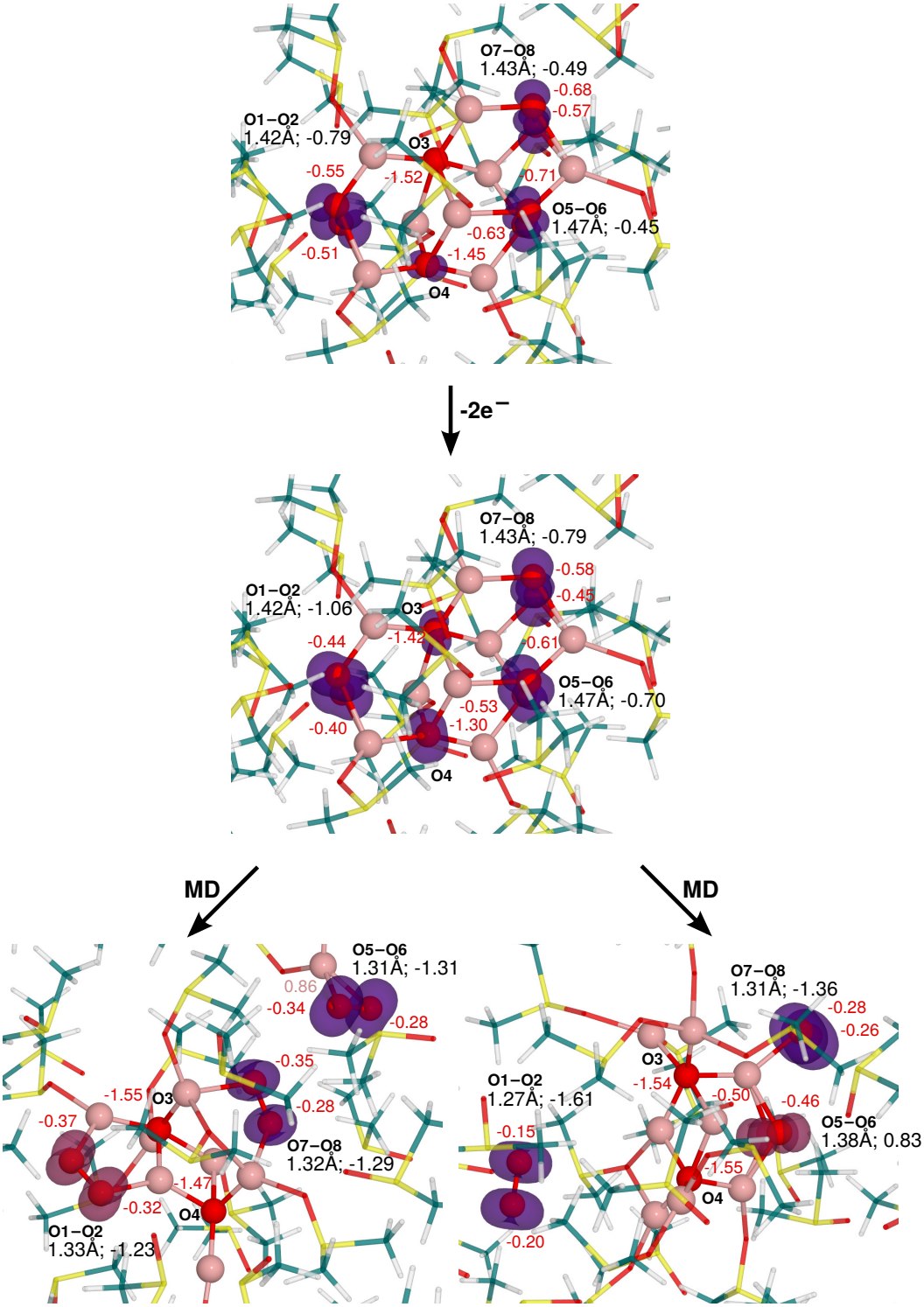

Figure 5.5.: Snapshots of DFT-based MD simulations of a Li_8O_8 cluster in DMSO after removal of two electrons with Bader atomic charges in e (same color as the atom type), O — O bond lengths and spin moments on O — O pairs (black), and their spin densities (blue and purple isosurfaces).

a different path. This time, instead of the detachment of an O_2 molecule, after about 3 ps into the new DFT-based run we observe a LiO_2 molecule leaving the cluster. Notably, though, $O-O$ bond lengths of about 1.32 Å, spin moments between 1.23 and 1.31, and average O charges between -0.35 e and -0.31 e both in the detached molecule and in the remaining cluster do not indicate pure superoxide bond types, but a trend toward the formation of molecular dioxygen coordinated to Li^+ ions.

5.4. Density of states evolution during decomposition

During the electron removal and cluster decomposition described above it is noteworthy that the Li atoms barely change their Bader charge values of about 0.86 e (see Figures 5.3 and 5.5). The changes are limited to the oxygen atoms, as reported in Table 5.1 and in Appendix D, Table D.1 for the initial and final states in vacuo and in DMSO. A visual representation of the charge differences are reported in Figure 5.6 and in Appendix D, Figure D.1.

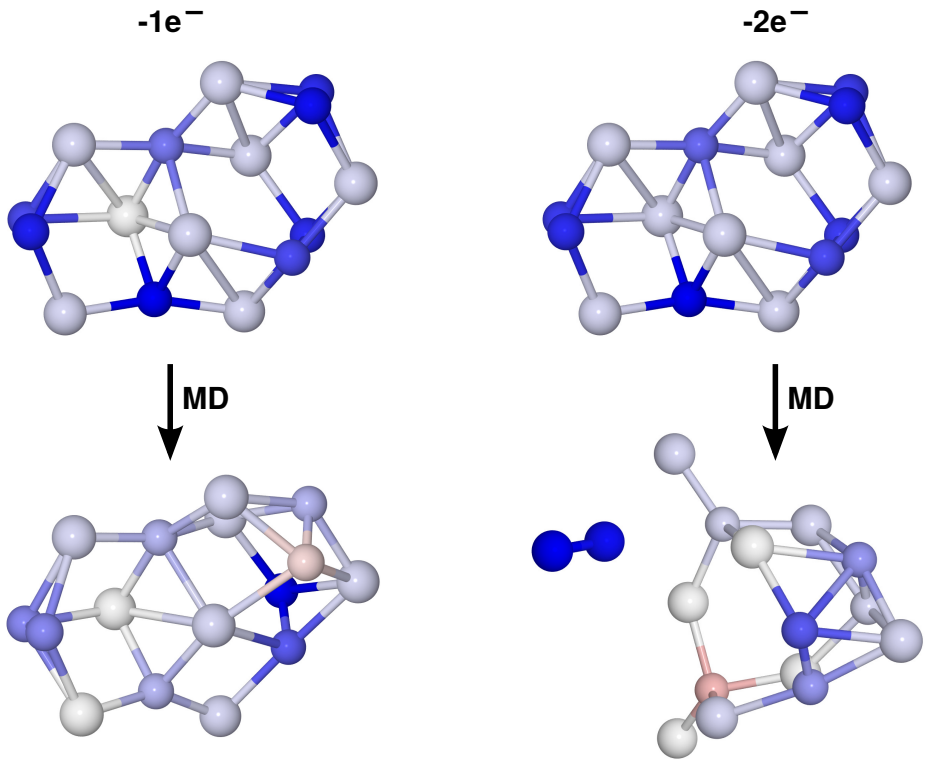

Figure 5.6.: Visualization of the Bader charge differences upon removal of electrons from negative (red) values to positive (blue) values in vacuo.

For the case of solvated clusters, non-negligible charge differences are localized on the solvent

molecules, in part due to polarization of the DMSO molecules neighboring the cluster and in part because of the well-known tendency of plane-wave-based DFT to over-delocalize electronic states. Note that the electrons are not removed from a single O atom or $O-O$ pair but rather uniformly from all oxygen species.

Table 5.1.: Charge difference in e between the initial clusters before removal of electrons and the final clusters after removal of electrons and an MD simulation in vacuum and in DMSO.

	$\Delta q_{\text{-1e}^-}$	$\Delta q_{\text{-2e}^-}$	
in vacuo			
Li_8O_8	1.0000	1.9999	
oxygens	0.8879	1.8312	
in DMSO			
DMSO	0.1712	0.3731	0.3600
Li_8O_8	0.8291	1.6261	1.6340
oxygens	0.8216	1.6552	1.6514

More precise information about the evolution of the electronic structure during the oxidation process can be obtained by analysis of the DOS projected on selected atoms (Figure 5.7 and Appendix E, Figures E.1, E.2, and E.3). As far as the Li atoms are concerned, differences in their DOS are mostly governed by their coordination number to oxygen atoms and pairs (see Appendix E, Figures E.1, E.2, and E.3). More interesting are the DOS changes experienced by the $O-O$ pairs. Before electron removal, the $O-O$ pairs in the Li_8O_8 cluster present a mixture of superoxide (O_2^-) and peroxide (O_2^{2-}) character, as evident especially for the $O1-O2$ and $O5-O6$ pairs, respectively (Figure 5.7 (a), red curves). This is consistent with the neutral Li_8O_8 cluster being composed by 8 Li^+ ions, 2 O^{2-} ions, and 3 $O-O$ pairs with formal oxidation state $O_2^{\frac{4}{3}-}$.

After removal of a single electron, all three pairs become of clear superoxide (O_2^-) character (Figure 5.7 (a), green curves), consistent with the formal oxidation states in a $[Li_8O_8]^+$ cluster (8 Li^+, 2 O^{2-}, 3 O_2^-). After removal of two electrons, one trajectory (both in vacuo and in DMSO) leads to the removal of the $O1-O2$ pair in the form of an oxygen molecule, as confirmed both by analysis of the charge and bond distance and by analysis of the projected DOS (Figure 5.7 (c), green curves). In the remaining $[Li_8O_6]^{2+}$ cluster, both the formal oxidation states (8 Li^+, 2 O^{2-}, 2 O_2^-) and the DOS indicate superoxide bond type of the two $O-O$ pairs. A second trajectory leads to removal of the $O7-O8$ pair together with a Li^+ ion. Here, the DOS indicate, rather than

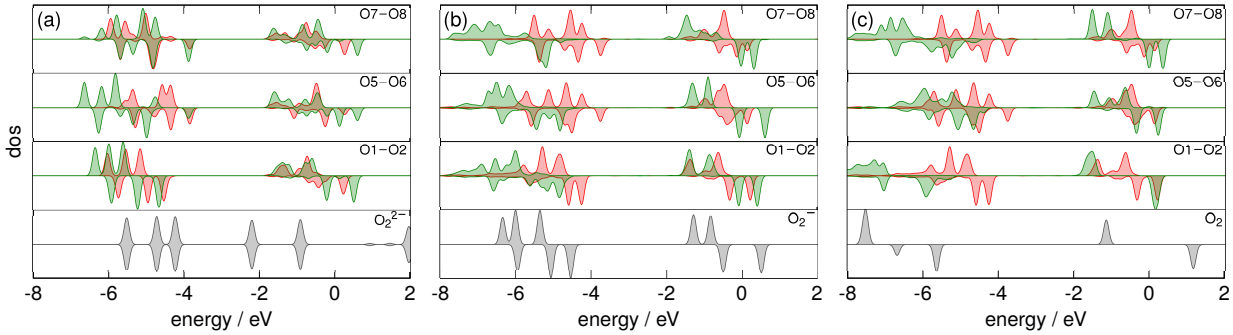

Figure 5.7.: DOS for $O-O$ pairs before removal of electrons (red) and after removal of electrons and an MD simulation (green) (a) in vacuo upon removal of a single electron and (b) and (c) in DMSO upon removal of two electrons. For comparison the DOS of the O_2^{2-} ion of a Li_2O_2 molecule, the O_2^- ion of a LiO_2 molecule and the O_2 molecule are shown in (a), (b), and (c) in gray.

a clear superoxide bond, a mixed superoxide/oxide character (Figure 5.7 (b), green curves). This is consistent with the previously mentioned $O-O$ bond length, spin, and charge intermediate between O_2 and O_2^-. We are thus inclined to write this second possible decomposition reaction as $Li_8O_8 \longrightarrow [LiO_2]^+ + [Li_7O_6]^+ + 2e^-$, suggesting that a Li^+ and a dioxygen molecule leave the cluster concomitantly and are not able to dissociate within the short MD simulation.

CHAPTER 6

DISCUSSION

Most of the available experimental literature about the mechanism of the OER during the charge of Li/air batteries indicates the presence of lithium superoxide species prior to the evolution of dioxygen molecules in the electrolyte. Starting from crystalline Li_2O_2, superoxide formation is suggested to proceed via a delithiation process taking place initially at the peroxide surfaces.[11,12,53] Static DFT-based total energy calculations have indeed confirmed that formation of Li vacancies in the interlayer sites of bulk Li_2O_2 may be energetically favored under the battery operation conditions.[50,51] However, recent evidence has suggested that the Li_2O_2 particles deposited during actual discharge processes are characterized by the presence of amorphous phases at their surfaces[12] or, with increasing current density, even purely amorphous peroxide films,[13] whose atomistic structure may be well described by Li_nO_n clusters.[106] The first stages of the OER are dominated by the chemical composition of the Li_2O_2 particle surfaces, rather than by their bulk composition and structure[11,12]. The small clusters studied in our work are a good model for the amorphous Li_2O_2 particle surfaces, since they include all relevant lithium and oxygen species (single O atoms as well as $O-O$ pairs) participating in the OER. As has been shown by Lau et al.[106] in a DFT-based calculation of $(Li_2O_2)_{16}$ clusters, surface $O-O$ pairs of peroxide, superoxide, and mixed peroxide/superoxide type in a high-spin state are the system-characterizing species also in the case of larger clusters. The authors concluded that their behavior do not differ, in essence, from one of the smaller cluster models and do not present additional or different chemical/physical properties than clusters of the size employed in the present work. The cluster size chosen in this work represents a trade-off between a sufficiently large model size and computational effort.

Interestingly, both previous literature results and our own simulations have shown that Li_nO_n clusters are formed by Li^+ coordinating not only peroxide $O-O$ pairs, but also single O atoms.

If, as usual, a formal oxidation state of $2-$ is assigned to such atoms, necessarily the $O-O$ pairs must assume intermediate peroxide/superoxide character. This situation emerges with clear evidence from our analysis of the bond lengths, atomic charges, spin moments, and local DOS of the $O-O$ pairs present in our lowest-energy cluster structures which we have obtained from unbiased MD simulations starting from various initial conditions including crystalline Li_nO_n clusters (see Figures 5.1 and 5.7 and Appendix E, Figures E.1, E.2, and E.3). Partial removal of electrons from these clusters, which corresponds to the application of a low oxidation potential to the cathode material, contributes to accentuate the superoxide character of the $O-O$ pairs. Notably, removal of only one electron from Li_8O_8 clusters is not sufficient to promote the spontaneous release of O_2 molecules, as instead observed in simulations of systems deprived of two electrons at the same time. These results can be interpreted as a two-stage process in which a peroxide-to-superoxide transition takes place at low oxidation potentials due to selective oxidation of $O-O$ pairs in amorphous Li_2O_2 phases, later followed by the evolution of dioxygen molecules at higher potentials. Notably, neither of these two processes require the dissolution of isolated Li^+ ions, at least in the very initial decomposition stages simulated in this work.

However, we have observed that a Li^+ ion is able to spontaneously leave the cluster bound to an O_2 molecule. While our DFT-based results indicate a mixed superoxide/oxide character of the $O-O$ bond in the leaving LiO_2 unit, we believe that the effects of solvent polarization and spurious electron delocalization contribute to lowering the total charge of the unit (+0.24 in our Bader analysis), so that in fact we should consider it as a $[LiO_2]^+$ species. It is conceivable that entropically driven effects not accessible within the short DFT-based MD simulation time could lead to a later dissociation of this molecule, effectively leading to a concomitant release of dioxygen and Li^+ ions, but this is an issue that would require further investigations.

In summary, on the basis of our simulations we propose, as an additional possibility to the reaction mechanisms suggested in the literature,[11–13,50,51,53] the following OER reaction steps:

(i) At low potential a partial oxidation of the amorphous Li_2O_2 phases present at the surface of the deposited peroxide particles without release of ions or molecules

$$[Li_2O_2] \longrightarrow [Li_2O_2]^{n+} + n\,e^- \ .$$

As a consequence, since the electron removal takes place selectively from $O-O$ pairs, the particles assume a partial superoxide character consistently with a number of spectroscopic investigations.[14]

(ii) At high potential release of both O_2 molecules and Li^+ ions

$$[Li_2O_2]^{n+} \longrightarrow [Li_2O_2]^{(n-m+k)+} + m\,Li^+ + s\,O_2 + k\,e^- \ .$$

Here, the different stoichiometric coefficients m, s, k express the idea that neither electron removal nor release of dioxygen may be directly associated with dissolution of a corresponding number of Li^+ ions but the processes can take place independently of each other, at least until a critical high decomposition potential is reached.

At the present stage we cannot exclude the possibility of early delithiation processes even at low oxidation potentials, since our analysis is limited to spontaneous (i. e., not thermically activated) processes. The quantification of possible kinetic barriers associated with decomposition processes in a solvent is, however, a task that goes far beyond the goals of the present work. Moreover, our short-time simulations do not allow us to reach any conclusion about the electrochemical stability of the electrolyte under application of a high oxidation potential, an issue that is known to limit the life-time of rechargeable Li/air batteries.[30,33] During our simulations, even after electron removal, the DMSO molecules are nevertheless observed to remain stable and to play an important role in the decomposition process, acting as complexing agents for the dissolving species. Finally, complementary studies considering the recently proposed and currently discussed delithiation during the OER[11,12,50–53] shall be performed in future work on extended Li_2O_2 crystalline surfaces.

Part 2.
Optimization of catalytically active sites positioning in porous cathodes of lithium/air batteries filled with different electrolytes

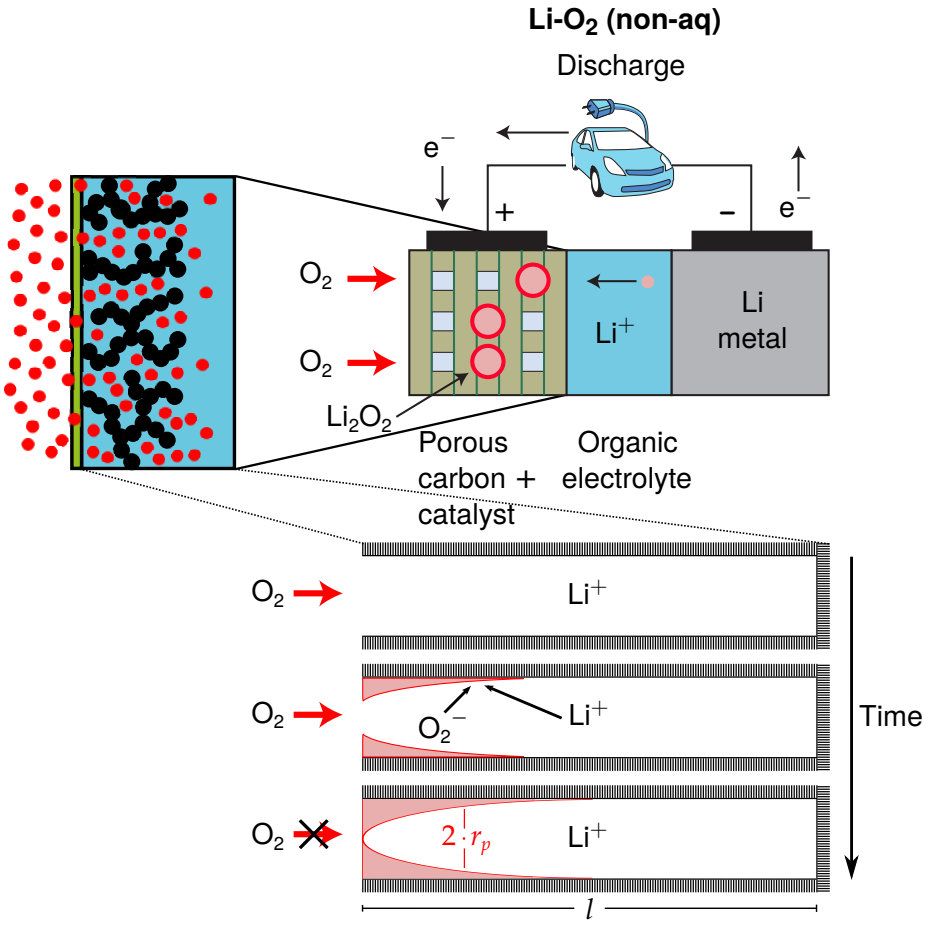

Model of a Li/air battery adapted from ref. 2 (top), a porous cathode adapted from ref. 107 (left) and schematic pore clogging (bottom).

CHAPTER 7

INTRODUCTION

The capacity of current Li/air cells is severely limited by the early clogging of the porous cathode due to the deposition of the discharge product Li_2O_2.[14,35] Assuming sufficient electrochemical stability of the materials used for the electrolyte and the electrodes, this is directly influenced by (i) the diffusivity and solubility of oxygen within the electrolyte, (ii) the structural details of the porous cathode, and (iii) the use and positioning of catalysts therein. In this part we perform a theoretical analysis of the progressive filling of a model porous cathode in different electrolytes. In particular, we aim at optimizing the positioning of catalytically active sites within the pores in order to maximize the volume of discharge products deposited before pore clogging sets in.

Since the non-aqueous electrolyte in an Li/air battery transports Li^+ ions to the anode, it should thus present a good Li^+-conductivity, guarantee sufficient stability of all species during the electrochemical reactions, and promote the formation of a protective SEI on the highly reactive metallic Li anode.[1] These requirements have restricted the choice of electrolytes to only a relatively small number of candidates. First attempts focused on alkyl carbonate electrolytes such as PC, containing either LiTFSI ($Li(CF_3SO_2)_2N$) or $LiPF_6$ salts.[19,35,108–110] However, recent studies have shown that carbonate-based electrolytes undergo possible degradation by side reactions evolving CO_2 rather than dioxygen.[23,25,27,28,111] Newer attempts focus on non-carbonate based electrolytes with low viscosities, moderate oxygen solubilities, and small dielectric constants.[55] Some of the most common representatives are TEGDME (tetraethylene glycol dimethyl ether), 2,3,4,5-tetrahydrothiophene-1,1-dioxide (Sulfolane - SL), DMSO and DME. The best performance in stability, so far, has been obtained with DMSO which enables reversibility over several cycles with low capacity loss.[30–33] In comparison, TEGDME and DME show a less stable behavior and tend to decompose during the charge process, likely because of the high cell potential.[15,28,29] In addition

to a suitable electrolyte, the electrode design provides a further mean of significantly improving the cell capacity. Basic requirements for a cathode are low cost, low weight, a straightforward fabrication and a good electron conductivity. Furthermore, the cathode has to provide enough storage volume for the insoluble Li_2O_2 discharge product and among others a comparably large surface area over which the ORR take place. The most commonly used cathodes are based on carbon materials coated onto metal grids or foams with a highly porous structure or on carbon nanotubes and fibers.[36,112] According to Viswanathan et al.[10] and Albertus et al.[19] passivation of the electrode due to the insulating character of lithium peroxide can take place after deposition of a 5 nm thick layer of Li_2O_2. Meini et al.[20] reported even a value below 1 nm limiting the discharge capacity. Consequently, a variety of carbon coatings with different surface areas, pore radii, and volumes as well as wettability properties have been investigated as potential cathode materials promoting a uniform thin film growth of the discharge product.[14,35,107,110,113]

Furthermore, since the oxygen solubility and diffusivity are low in non-aqueous electrolytes, there is a fast oxygen concentration drop from the oxygen supplying side into the interior regions of each pore, as shown for instance by Read et al.[114] via a steady-state model and schematically in Figure 7.1.

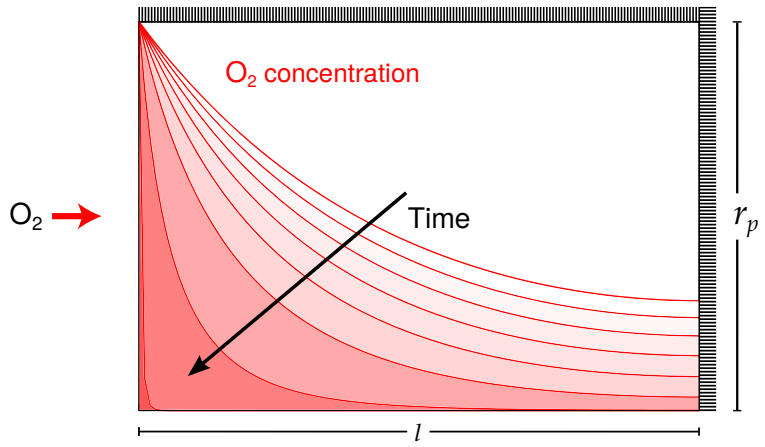

Figure 7.1.: Schematic representation of the concentration drop in a half-pore of radius r_p and length l.

As a consequence, the electrochemical Li_2O_2 deposition takes place preferentially at the oxygen supplying side, blocking the oxygen transport into the pore, as demonstrated by means of SEM imaging by Zhang et al.[36] This clogging of the narrow pore entrances by Li_2O_2 leads to a loss of active surface area for the electrochemical reaction and a lack of utilization of the cathode volume.[14,35]

In an effort to alleviate these problems, different catalysts have been proposed to enhance the electrochemical efficiency,[37–39] in particular α-MnO_2, Pd, Pt or Au nanoparticles and their combinations.[40–43] In order to prevent pore clogging, Williford et al.[115] suggested a dual pore system composed of a catalyzed and a non-catalyzed part. Solving theoretically a diffusion model, the authors could demonstrate an improvement of the cathode volume utilization when this dual pore system is combined with a time-released activation of the catalytic sites. Also Andrei et al.[116] studied how catalysts improve the discharge capacity. In their theoretical study the authors have demonstrated that pore clogging and oxygen starvation are reduced by a non-uniform distribution of catalytically active sites which they modeled via an exponential increase of the deposition rate along the pore. In this particular case, the authors observed a significant enhancement of energy density and specific capacity.

To take advantage of state-of-the-art achievements in stable electrolytes, cathode designs, and catalyst use, the present part focuses on the improvement of the discharge capacity by means of a smart catalyst distribution. In order to suggest a catalyst distribution that leads to a maximal pore volume utilization, we first implement a numerical method for the solution of a reaction-diffusion equation[117] that describes the catalytic growth of Li_2O_2 in narrow pores, based on previous models by Sandhu et al.[44] and Andrei et al.[116] We then optimize the number of catalytic sites and their positions along the pore by means of a Greedy optimization algorithm.[118] This procedure is carried out for the case of different electrolytes (PC^{Li^+}, $TEGDME^{Li^+}$, SL, $DMSO^{Li^+}$ and DME^{Li^+}) presenting different combinations of oxygen diffusivities and solubilities. This allows us to demonstrate that non-uniform and electrolyte-dependent catalyst distributions can lead to a considerable increase in capacity with respect to uniform or non-catalyzed discharge product depositions.

CHAPTER 8

PORE CLOGGING AND FINITE DIFFERENCE METHOD

The modeling of pore clogging in Li/air batteries is based on chemical and physical processes within the battery as well as the mathematical methods which provide a solution of the considered issue. Thus, the following chapter is focused on a brief introduction to reaction kinetics and diffusion processes and concludes with a detailed guide for the applied method of finite differences with regard to the particular form of the established partial differential equations.

8.1. Reaction rate of a chemical process

The reaction rate v_R defines the change in molar concentration c of species in a chemical process

$$\sum_{i \in I} r_i R_i \rightarrow \sum_{j \in J} p_j P_j, \qquad I, J \subset \mathbb{N} \quad finite\,,$$

where R_i are the reactants, P_j the products and r_i and p_j the corresponding stoichiometric coefficients. According to ref. 119 we can write the reaction rate as

$$v_R = -\frac{1}{r_l}\frac{\mathrm{d}c_{R_l}}{\mathrm{d}t} = \frac{1}{p_m}\frac{\mathrm{d}c_{P_m}}{\mathrm{d}t} \quad \forall l \in I, \forall m \in J\,. \tag{8.1}$$

The negative sign indicates the consumption of reactants. A different approach to the reaction rate is based on the conservation of mass and formulated in the rate law[120] as

$$v_R = k \cdot \prod_{i \in I} c_{R_i}^{x_i} \, . \tag{8.2}$$

The reaction rate constant k of the reduction is dependent on extrinsic properties such as temperature and potential, but does not depend on the concentration. The exponents x_i have to be determined experimentally and are added up to the reaction rate order $\sum_i x_i$. A combination of both approaches in equations (8.1) and (8.2) results in the temporal change in concentration of a reactant R_l during a chemical reaction

$$\frac{\mathrm{d}c_{R_l}}{\mathrm{d}t} = -k \cdot r_l \prod_{i \in I} c_{R_i}^{x_i} \quad \forall l \in I \, . \tag{8.3}$$

The derivation of the reaction rate constant is carried out from collision theory. We assume the velocity distribution of two reacting particles A and B of a chemical process $aA + bB \rightarrow C$ as the Maxwell-Boltzmann distribution of the kinetic theory of gases[121]

$$f(v) = \left(\frac{\mu}{2\pi k_B T} \right)^{\frac{3}{2}} \cdot 4\pi v \exp\left(\frac{-\frac{\mu}{2} v^2}{k_B T} \right) \mathrm{d}v \, ,$$

where T is the temperature, k_B the Boltzmann constant and $\mu = \frac{m_A m_B}{m_A + m_B}$ the relative mass. The mean velocity $\overline{v}$ of A relative to B is written as

$$\overline{v} = \int_0^\infty v \cdot f(v) \mathrm{d}v = \left(\frac{8 k_B T}{\pi \mu} \right)^{\frac{1}{2}} \, .$$

In a time Δt particle A covers a collision volume $\Delta V = \overline{v} \Delta t \sigma_{AB}$, where $\sigma_{AB} = \pi r_{AB}^2$ defines the cross section of particle A and B schematically shown in Figure 8.1 (a).

Hence, the number of collisions between all particles A and B per unit volume and time is given by $\tilde{Z}_{AB} = \sigma_{AB} \overline{v} \tilde{c}_A \tilde{c}_B$ or in the molar notation using the Avogadro constant N_A

$$Z_{AB} = \frac{\tilde{Z}_{AB}}{N_A} = \sigma_{AB} \overline{v} N_A \frac{\tilde{c}_A}{N_A} \frac{\tilde{c}_B}{N_A} = \sigma_{AB} \overline{v} N_A c_A c_B = \sigma_{AB} \left(\frac{8 k_B T}{\pi \mu} \right)^{\frac{1}{2}} N_A c_A c_B \, .$$

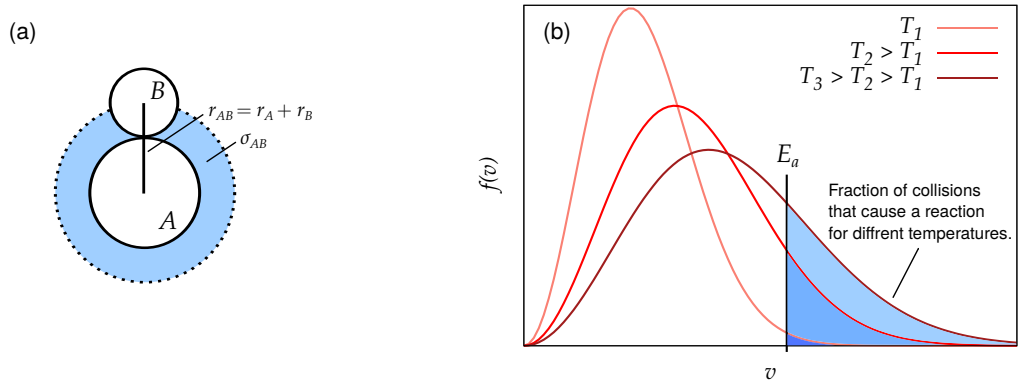

Figure 8.1.: (a) Cross section of particles A and B, and (b) Maxwell-Boltzmann distribution for different temperatures.

Provided that every collision causes a reaction, the number of collisions equals the reaction rate

$$v_R = Z_{AB}$$
$$k \cdot c_A c_B = \sigma_{AB} \left(\frac{8 k_B T}{\pi \mu} \right)^{\frac{1}{2}} N_A c_A c_B \, .$$

However, the derived relation does not reproduce the temperature dependency of the reaction rate constant $k \propto \exp\left(-\frac{E_a}{RT}\right)$ that has been observed experimentally by Arrhenius,[122] where E_a is the activation energy and $R = N_A \cdot k_B$ the universal gas constant.[123] The mismatch between theory and experiment emerges from the assumption that all particles possess the same mean velocity $\overline{v}$, and every collision causes a reaction. However, a reaction takes place only if the kinetic energy of a particle reaches the activation energy E_a, as illustrated in Figure 8.1 (b). This assumption results in a velocity-dependent cross section $\sigma_{AB} = \sigma_{AB}(v)$, such that the reaction rate constant is calculated via an integral over all velocities according to the Maxwell-Boltzmann distribution. Using the kinetic energy $E = N_A \mu / 2 \cdot v^2$, we state

$$\begin{aligned} k(T) &= \int_0^\infty \underbrace{\sigma_{AB}(v) v N_A}_{k} \cdot f(v) \mathrm{d}v \\ &= \int_0^\infty \sigma_{AB}(E) f(E) \frac{1}{\mu} \mathrm{d}E \\ &= \frac{1}{N_A} \left(\frac{8}{\pi \mu (k_B T)^3} \right)^{\frac{1}{2}} \int_0^\infty \sigma_{AB}(E) E \exp\left(-\frac{E}{RT}\right) \mathrm{d}E \, . \end{aligned}$$

All particles that do not overcome the activation energy have a cross section of zero. Otherwise we use the probability $p = \frac{E-E_a}{E}$ that a reaction is caused by a collision and summarize for the cross section

$$\sigma_{AB}(E) = \begin{cases} 0, & \text{if } E \leq E_a \\ \sigma_{AB} \cdot \frac{E-E_a}{E}, & \text{if } E > E_a \end{cases} .$$

The reaction rate constant can now be written as

$$\begin{aligned} k(T) &= \frac{1}{N_A} \left(\frac{8}{\pi \mu (k_B T)^3} \right)^{\frac{1}{2}} \int_{E_a}^{\infty} \sigma_{AB} \cdot (E - E_a) \exp\left(-\frac{E}{RT} \right) \mathrm{d}E \\ &= N_A \left(\frac{8 k_B T}{\pi \mu} \right)^{\frac{1}{2}} \sigma_{AB} \exp\left(-\frac{E_a}{RT} \right) \\ &= k_0(T) \exp\left(-\frac{E_a}{RT} \right) . \end{aligned} \tag{8.4}$$

The exponential temperature dependency as well as the pre-exponential factor $k_0(T)$ are in good agreement with experimental results.

In a last step we analyze the dependency of the reaction rate constant on an external potential U. The activation energy for the reduction of dioxygen is the provided Gibbs free energy ΔG, schematically shown in Figure 8.2 (a). However, an external potential changes the required energy according to $\Delta G = \Delta G(U = 0) + \alpha z F U = E_a + \alpha z F U$ (see Figure 8.2 (b)). Thus, the required energy is composed of the activation energy and the electric energy zFU, where z is the charge number and F the Faraday constant (amount of charge of one mol of electrons). The charge transfer coefficient $\alpha \in [0, 1]$ considers the dependency of the reaction rate on an external potential

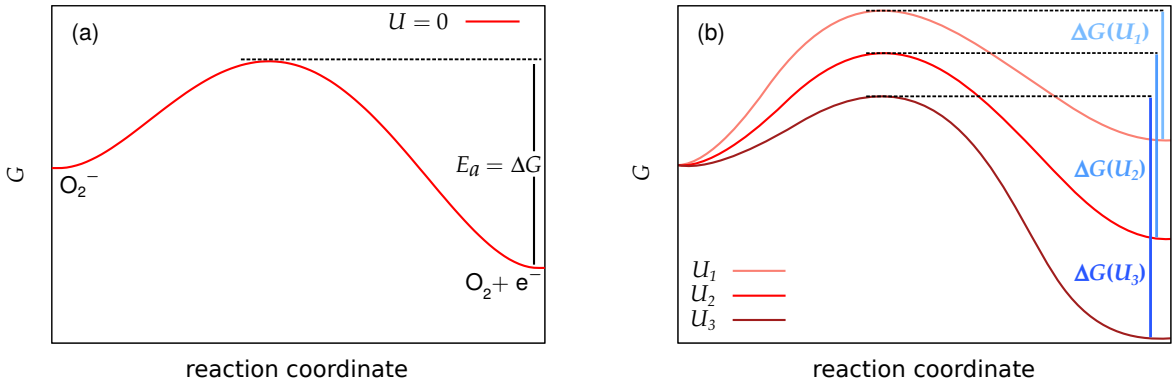

Figure 8.2.: (a) Gibbs free energy of a redox reaction, and (b) influence of an external potential on the Gibbs free energy.

and is most often set to $\alpha = 0.5$.

Finally, we obtain the dependency of the reaction rate constant on temperature as well as on an external potential U

$$k(T) = k_0(T) \exp\left(-\frac{E_a}{RT}\right) \exp\left(-\frac{\alpha z F U}{RT}\right) . \tag{8.5}$$

8.2. Reaction-diffusion equation

Diffusion is a gradient-driven process that describes a compensation of differences in concentration via a stochastic movement of particles induced by their kinetic energy. The ordinary diffusion equation without a reactive term (reaction rate) results from the two Fickian laws. The first law can be derived from collision theory[121] and is stated as follows.

Fick's law 1. *The particle current density $\vec{j}$ is proportional to the gradient of concentration c against the direction of diffusion*

$$\vec{j} = -D \cdot \operatorname{grad} c . \tag{8.6}$$

The constant of proportionality is called diffusion coefficient D. The second law is better known as the continuity equation and is based on the conservation of mass, i. e., in a certain volume particles are neither created nor destroyed.[121]

According to the continuity equation, the temporal change of the density of a conserved quantity corresponds to the spatial change of its current density, i. e., in the present case using the particle number as the conserved quantity

$$\partial_t c = -\operatorname{div} \vec{j} . \tag{8.7}$$

Fick's law 2. *Assuming of a position-independent diffusion coefficient, a combination of Fick's first law (8.6) and the continuity equation (8.7) results in the diffusion equation*

$$\partial_t c = D \cdot \operatorname{div}(\operatorname{grad} c) . \tag{8.8}$$

The reaction-diffusion equation is based on the ordinary diffusion equation (8.8) considering a chemical reaction which causes a variation of the concentration of diffusing particles. The general form of the equation is given by

$$\partial_t c = D \cdot \operatorname{div}(\operatorname{grad} c) + v_R(c) . \tag{8.9}$$

The reaction rate $v_R(c)$ considers the change in concentration not because of diffusion and hence the movement of particles, but because of an actual conversion of matter. According to

equation (8.3) we can write the reaction rate for a reactant with stoichiometric coefficient r and concentration c as

$$v_R(c) = -k \cdot r \prod_{i \in I} c_i^{x_i} \,, \tag{8.10}$$

where $c_i = c$ for an i.

8.3. Diffusion dependent growth in a porous structure

During the discharge process at the cathode oxygen is consumed by its reaction with lithium ions, and the pore volume decreases due to the growth of Li_2O_2. The mathematical description of this process is based on a diffusion-limited model introduced by Sandhu et al.[44]

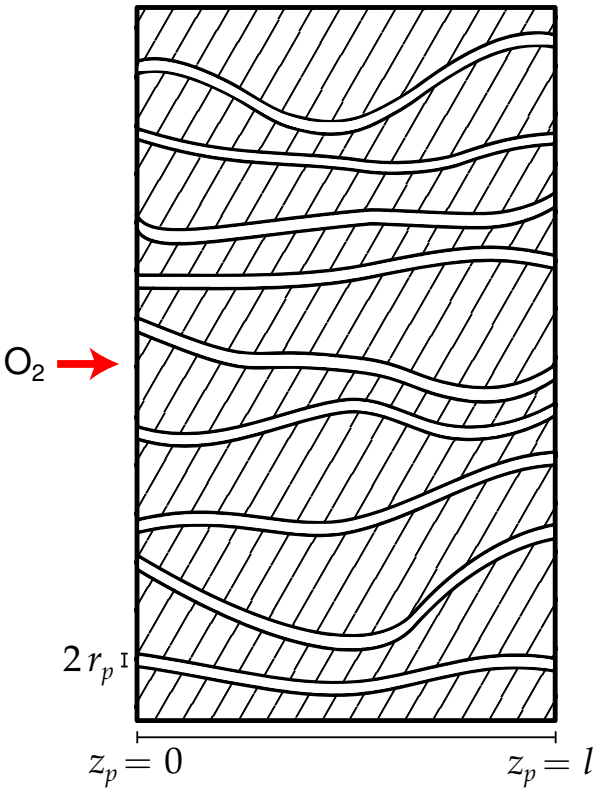

Figure 8.3.: Schematic representation of the modeled cathode geometry with porosity ϵ and tortuosity τ.

A porous cathode of volume V_{cath}, length l, and porosity ϵ is modeled as a set of n cylindrical pores of radius r_p, length l, and tortuosity τ, fully filled with electrolyte (see Figure 8.3). According to Bruggeman the tortuosity is a function of porosity, and it is assumed that $\tau = \epsilon^{-\frac{1}{2}}$.[124] The cathode is thus characterized by a porosity $\epsilon = \pi r_p^2 l \tau n / V_{cath}$ and a specific pore area $a_{cath} = 2\pi r_p l \tau n / V_{cath} = 2\epsilon / r_p$. As shown by Andrei et al.,[116] who considered the diffusion of lithium ions from a finite-sized electrolyte phase, the decrease of Li^+ concentration from the separator to the oxygen supplying side of the cathode decreases only very slightly. Thus, the Li^+ concentration is kept constant, and the sole limiting factor in the present model is the diffusion of oxygen inside the pore. Moreover, if $r_p \ll l$, we can assume angular symmetry around the diffusion direction z_p along the pore axis and no change of the oxygen concentration c_{O_2} in the radial direction. Therefore, we can describe the dynamics of the discharge processes by two coupled partial differential equations using z_p as the only dimensional coordinate.

The first one is a reaction-diffusion equation introduced in Section 8.2, equation (8.9) based on a Fickian diffusion in a porous structure without convection[44,125]

$$\partial_{t_p}(\epsilon c_{O_2}) = \partial_{z_p}\left(D^{\text{eff}}_{O_2} \cdot \partial_{z_p} c_{O_2}\right) + v_R(c_{O_2}, \epsilon, r_p)\ . \tag{8.11}$$

Here, the effective diffusion coefficient $D^{\text{eff}}_{O_2}$ considers the impact of porosity ϵ and tortuosity τ on the oxygen mass diffusivity D_{O_2} via $D^{\text{eff}}_{O_2} = D_{O_2} \cdot \epsilon/\tau$.[126] The rate of Li_2O_2 formation per unit of cathode volume (reaction rate) is represented by $v_R(c_{O_2}, \epsilon, r_p)$. Based on the assumption of a sufficiently high concentration of lithium ions, the reaction rate is given by the change of oxygen concentration c_{O_2} due to the first-order ORR $O_2 + e^- \rightarrow O_2^-$ with stoichiometric coefficient r = 1. That is to say, we have a direct proportionality between the oxygen concentration and the reaction rate (see equation (8.10)). Since the reduction is only taking place at the pore surface, we can write the reaction rate as

$$v_R(c_{O_2}, \epsilon, r_p) = a_{cath} \cdot \partial_{t_p} c_{O_2} = -\frac{2\epsilon}{r_p} \cdot k \cdot c_{O_2}\ , \tag{8.12}$$

where k is the reaction rate constant per unit of specific pore area. It should be noted that the first-order approximation of the reaction rate may be considered as a simplification which is, however, often used in the pertinent literature.[44,115,116,127] In several of these previous studies first-order deposition rates have been shown to be a successful approximation if the modeling of pore clogging is considered.

The second equation

$$\partial_{t_p}\epsilon = v_R(c_{O_2}, \epsilon, r_p) \cdot \frac{M_{Li_2O_2}}{\rho_{Li_2O_2}} \tag{8.13}$$

considers the decrease of free pore volume in terms of the reaction rate weighted by the molar volume $M_{Li_2O_2}/\rho_{Li_2O_2}$ of the discharge product, where $M_{Li_2O_2}$ is the molar mass and $\rho_{Li_2O_2}$ the density of Li_2O_2. Using the initial values $\epsilon_0 = \epsilon(t_p = 0)$, $r_p^0 = r_p(t_p = 0)$ and the above Bruggeman relation, the porosity can be related to the pore radius via

$$\left(\frac{\epsilon}{\epsilon_0}\right)^{\frac{3}{2}} = \left(\frac{r_p}{r_p^0}\right)^2\ .$$

The introduction of dimensionless quantities

$$t = \frac{t_p D_{O_2}\sqrt{\epsilon_0}}{l^2}, \quad r = \frac{r_p}{r_p^0}, \quad z = \frac{z_p}{l} \quad \text{and} \quad c = \frac{c_{O_2}}{c_{O_2,0}} \quad (0 \leq r, z, c \leq 1)$$

reduces the partial differential equations (8.11) and (8.13) to their final form

$$\partial_t(r^{\frac{4}{3}}c) = \partial_z\left(r^2 \cdot \partial_z c\right) - \beta \cdot r^{\frac{1}{3}}c \tag{8.14}$$

and

$$\partial_t r = -\gamma c\ , \tag{8.15}$$

where $c_{O_2,0} = c_{O_2}(z_p = 0)$ is the oxygen solubility at a temperature of 298 K and a pressure of 1 atm O_2 in each of the considered electrolytes listed in Table 8.1.

Table 8.1.: Oxygen solubility $c_{O_2,0}$ and diffusivity D_{O_2} of the five considered electrolytes. The oxygen solubility at 1 atm and 298 K for DMSO is adopted from ref. 96, all other solubilities are based on the Bunsen coefficients of the pure solvents from ref. 114. The diffusivities are taken from ref. 7 with the exception of PC.[114]

	$c_{O_2,0}/10^{-6}$ mol cm^{-3}	$D_{O_2}/10^{-6}$ cm^2 s^{-1}
PC^{Li^+}	3.20	2.24
$TEGDME^{Li^+}$	4.43	2.17
SL	1.47	12.00
$DMSO^{Li^+}$	2.10	16.70
DME^{Li^+}	9.56	12.20

The parameters β and γ are given by

$$\beta = k \cdot \frac{2l^2}{D_{O_2}\sqrt{\epsilon_0}r_p^0} \quad \text{and} \quad \gamma = k \cdot \frac{3l^2 c_{O_2,0}}{2D_{O_2}\sqrt{\epsilon_0}r_p^0}\frac{M_{Li_2O_2}}{\rho_{Li_2O_2}}\ . \tag{8.16}$$

They are calculated at a given time t under the condition of a constant cathode current density of 0.1 mA cm^{-2} which reflects the usual operation mode of Li/air electrochemical cells.[16,28,32]

Current density and reaction rate constant In the present work the current density is computed with respect to the nominal accessible cathode surface. According to Faraday's laws the current density change di per unit of cathode length dz_p is given by $\mathrm{d}i = -n_e F \mathrm{d}_t c_{O_2} \mathrm{d}z_p$, where n_e is the number of electrons being transfered during the electrochemical process. Assuming a two-electron process for the formation of one Li_2O_2 unit and using the above substitutions, the

total current density can be calculated via

$$i(t) = k \cdot \frac{4F\epsilon_0 c_{O_2,0} l}{r_p^0} \cdot \int_0^1 r^{\frac{1}{3}}(z,t) \cdot c(z,t) \mathrm{d}z \ . \tag{8.17}$$

Setting $i(t) = i$ allows k to be calculated which is required to compute β and γ from equation (8.16) along with all other parameters adopted from Sandhu et al.[44] and summarized in Table 8.2. Pore radius, cathode length, porosity as well as the applied current density are consistent with experimental data of typical porous cathodes.[14,35,109,114,128]

Table 8.2.: Parameters employed in the reaction-diffusion model for Li_2O_2 deposition.[44]

parameter		
r_p^0	/ 10^{-7} cm	2.00
l	/ cm	0.07
ϵ_0		0.73
$M_{Li_2O_2}$	/ g mol^{-1}	45.8768
$\rho_{Li_2O_2}$	/ g cm^{-3}	2.3
i	/ mA cm^{-2}	0.1

Initial and boundary conditions At the beginning of the process we assume that the pore is free from deposited Li_2O_2 and oxygen, i. e., for $t = 0$

$$r = 1 \quad \text{for} \quad 0 \leq z \leq 1 \quad \text{and} \quad c = 0 \quad \text{for} \quad 0 < z \leq 1 \ .$$

The concentration at the pore entrance is fixed to the maximum, normalized solubility, and a vanishing oxygen gradient is assumed for all $t \geq 0$ at the end of the pore for an oxygen supply on one side and in the center for an oxygen supply on both sides (in the following referred to as one-sided and two-sided pore)

$$c = 1 \quad \text{for} \quad z = 0 \quad \text{and} \quad \partial_z c = 0 \quad \text{for} \quad z = 1 \quad \text{or} \quad z = \frac{1}{2} \ .$$

Localized growth via catalysts In the previous model we assume a continuous catalyst distribution, i. e., the pore surface itself acts as a catalyst for the growth of Li_2O_2. To model a

catalytically-induced growth on selected sites along the pore surface, the decrease of free pore volume in equation (8.15) is modified by a catalytic function $cat(z) : [0,1] \to [0,1]$ according to

$$\partial_t r = -\gamma c \cdot cat(z) \ . \tag{8.18}$$

The discretization and numerical implementation via a threshold is discussed in detail in Chapter 9.

8.4. Finite difference method

The two partial differential equations (8.14) and (8.15) describing the pore clogging are solved numerically via a discrete finite difference method. This method is introduced in the following chapter after a brief general characterization of partial differential equations and analyzed for its consistency, stability, and convergence with regard to the considered problem. The approach is mainly based on the textbooks of Großmann & Roos,[117] Samarskii,[129] and Thomas.[130]

8.4.1. Classification of partial differential equations

The classification of partial differential equations is based on four characteristics:

- number of independent variables
- order (highest partial derivative)
- linearity (are the considered function and all its partial derivatives linear?)
- homogeneity (does the function-independent term vanish identically?).

Both considered differential equations are linear, maximum of the order of two, and have two independent variables time and space. The general form of a first-order equation for a sufficiently often differentiable function $u : \Omega \to \mathbb{R}$, where $\Omega = [a,b] \times [c,d] \subset \mathbb{R} \times \mathbb{R}$ and $(z,t) \in \Omega$, is stated as:

$$d(z,t)\partial_z u + e(z,t)\partial_t u + f(z,t)u = g(z,t) \ , \tag{8.19}$$

the equation of second order as

$$a(z,t)\partial_{zz} u + b(z,t)\partial_{zt} u + c(z,t)\partial_{tt} u + d(z,t)\partial_z u + e(z,t)\partial_t u + f(z,t)u = g(z,t) \ . \tag{8.20}$$

Considering the discriminant of the quadratic part, we define the following classification for the second-order equation on the basis of the general equation for conic sections.

Definition 8.1. *Equation (8.20) is called*

1. *hyperbolic, if* $b^2(z,t) - 4a(z,t)c(z,t) > 0 \quad \forall (z,t) \in \Omega$
2. *parabolic, if* $b^2(z,t) - 4a(z,t)c(z,t) = 0 \quad \forall (z,t) \in \Omega$
3. *elliptic, if* $b^2(z,t) - 4a(z,t)c(z,t) < 0 \quad \forall (z,t) \in \Omega \quad .$

[131]

A comparison of the general partial differential equations (8.19) and (8.20) with the partial differential equations considered in the present work for the first-order equation (8.15)

$$\partial_t r + \gamma c = 0$$

results in $d(z,t) = f(z,t) = 0$. Thus, the first equation is an ordinary, inhomogeneous differential equation coupled with the second-order equation (8.14)

$$\partial_{zz} c + \big(2r^{-1}\partial_z r\big)\partial_z c + \big(-r^{-\frac{2}{3}}\big)\partial_t c + \Big[-r^{-\frac{5}{3}}\Big(\frac{4}{3}\partial_t r + \beta\Big)\Big]c = 0\,.$$

In this particular case we obtain for the coefficients $b(z,t) = c(z,t) = g(z,t) = 0$ and $a(z,t) = 1$, i. e., the second partial differential equation is homogeneous and of parabolic type. Thus, all following consideration are restricted to the resulting prototypes

$$\partial_t u = g \tag{8.21}$$

and

$$\partial_{zz} u + d\partial_z u + e\partial_t u + fu = 0\,. \tag{8.22}$$

Boundary conditions Linear boundary conditions of partial differential equations of the considered prototypes are divided in three classes (for $\alpha, \beta, \gamma, \delta \in \mathbb{R}$).

Definition 8.2.

- *Dirichlet boundary condition*

$$u(a,t) = \alpha, \quad u(b,t) = \beta \quad \textit{and} \quad u(z,c) = \gamma, \quad u(z,d) = \delta$$

- *Neumann boundary condition*

$$\partial_z u(a,t) = \alpha, \quad \partial_z u(b,t) = \beta \quad \textit{and} \quad \partial_t u(z,c) = \gamma, \quad \partial_t u(z,d) = \delta$$

- *Robin boundary condition*

$$A_1 u(a,t) + A_2 \partial_z u(a,t) = \alpha, \quad B_1 u(b,t) + B_2 \partial_z u(b,t) = \beta \qquad A_1, A_2, B_1, B_2 \in \mathbb{R}$$

and

$$C_1 u(z,c) + C_2 \partial_z u(z,c) = \alpha, \quad D_1 u(z,d) + D_2 \partial_t u(z,d) = \beta \qquad C_1, C_2, D_1, D_2 \in \mathbb{R}\ .$$

[117]

In the present work mixed boundary conditions (Dirichlet and Neumann) are used and denoted as initial conditions for the second variable time.

8.4.2. Finite difference method

The basic idea of the finite difference method is the approximation of partial derivatives with their difference quotient. For this purpose, we define the finite differences for a function u of two variables z and t as

Definition 8.3.

- *forward difference* $(D_z^+ u)(z,t) = \frac{u(z+\Delta z,t)-u(z,t)}{\Delta z}$
- *backward difference* $(D_z^- u)(z,t) = \frac{u(z,t)-u(z-\Delta z,t)}{\Delta z}$
- *central difference* $(D_z^0 u)(z,t) = \frac{u(z+\Delta z,t)-u(z-\Delta z,t)}{2\Delta z}$ *(1st order)*
- *central difference* $(D_z^+ D_z^- u)(z,t) = \frac{u(z+\Delta z,t)-2u(z,t)+u(z-\Delta z,t)}{(\Delta z)^2}$. *(2nd order)*

Analogously for the second variable t.[117]

In addition to the approximation with finite differences, a numerical description of differential equations requires a restriction of the variables on a discrete grid. For both variables we define two

equidistant grids as

$$z_j = j \cdot \Delta z, \qquad j = 0, \ldots, J$$
$$t_n = n \cdot \Delta t, \qquad n = 0, \ldots, N\ ,$$

where Δz and Δt are the chosen spacings (spatial resolution and time step). In this notation we write the difference quotients as

Definition 8.4.

- *forward difference* $D_j^+ u_j^n = \frac{u_{j+1}^n - u_j^n}{\Delta z}$
- *backward difference* $D_j^- u_j^n = \frac{u_j^n - u_{j-1}^n}{\Delta z}$
- *central difference* $D_j^0 u_j^n = \frac{u_{j+1}^n - u_{j-1}^n}{2\Delta z}$ *(1st order)*
- *central difference* $D_j^+ D_j^- u_j^n = \frac{u_{j-1}^n - 2u_j^n + u_{j+1}^n}{(\Delta z)^2}$, *(2nd order)*

where $u_j^n = u(j \cdot \Delta z, n \cdot \Delta t)$.
Analogously for the variable n.

The order of discretization of the partial differential equations is set to first in space z and second in time t (vertical method of lines), in contrast to the horizontal method of lines (first in time and second in space), or simultaneously in both. The discretization in space provides two different approaches which are introduced in the following.

Explicit space discretization The explicit method is based on the calculation of the function $(u_j^{n+1})_{j=0,\ldots,J}$ in the next time step based on known values of the present time step $(u_j^n)_{j=0,\ldots,J}$. The first derivatives in the considered partial differential equations are approximated using a forward difference, the second derivatives using a central difference according to

$$\partial_z u \approx D_j^+ u_j^n = \frac{u_{j+1}^n - u_j^n}{\Delta z} \qquad \text{and} \qquad \partial_{zz} u \approx D_j^+ D_j^- u_j^n = \frac{u_{j-1}^n - 2u_j^n + u_{j+1}^n}{(\Delta z)^2}\ .$$

Implicit space discretization The implicit method is based on the calculation of the function $(u_j^{n+1})_{j=0,\ldots,J}$ in the next time step using the function itself, i. e., the solution of a system of equations is required and hence the method is implicit. In this approach we approximate the first

derivatives using a forward difference and the second with a central difference according to

$$\partial_z u \approx D_j^+ u_j^{n+1} = \frac{u_{j+1}^{n+1} - u_j^{n+1}}{\Delta z} \qquad \text{and} \qquad \partial_{zz} u \approx D_j^+ D_j^- u_j^{n+1} = \frac{u_{j-1}^{n+1} - 2u_j^{n+1} + u_{j+1}^{n+1}}{(\Delta z)^2} \; .$$

Explicit time discretization For all approaches the time derivatives are approximated using a forward difference

$$\partial_t u \approx D_n^+ u_j^n = \frac{u_j^{n+1} - u_j^n}{\Delta t} \; .$$

The resulting equations and system of equations to be solved are

$$D_n^+ u_j^n = g_j^n \tag{8.23}$$

and summarized for the explicit ($\sigma = 0$) and the implicit method ($\sigma = 1$)

$$\left(D_j^+ D_j^- + d_j^n D_j^+ \right) \left(\sigma u_j^{n+1} + (1-\sigma) u_j^n \right) + \left(e_j^n D_n^+ + f_j^n \right) u_j^n = 0 \; . \tag{8.24}$$

The parameter σ varies between 0 and 1 yielding further implicit methods such as the Crank-Nicolson method for $\sigma = \frac{1}{2}$. To illustrate the procedure of the finite differences approaches, the explicit, the implicit, and the Crank-Nicolson method are shown in Figure 8.4 as stencils.

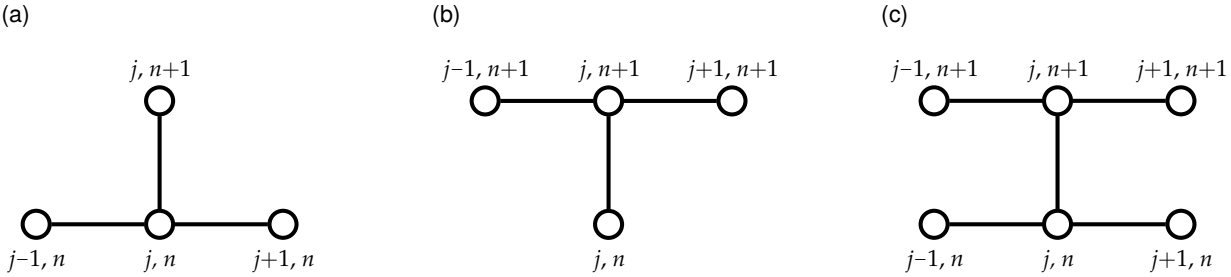

Figure 8.4.: Stencils for (a) the explicit, (b) the implicit, and (c) the Crank-Nicolson method (adapted from ref. 132).

The main difference between the various methods are their consistency and stability. Both terms are introduced in the following section in addition to a definition of convergence of a method. Finally, the considered problem is analyzed with regard to these properties.

8.4.3. Consistency, stability, and convergence

The quality of the approximation of a differential operator is characterized by the consistency and the corresponding order. To define the concept of consistency, we consider a linear differential operator $L : C^k(\Omega) \to C^0(\Omega)$ of the order k given by

$$Lu = \sum_{|\alpha| \leq k} a_\alpha(z) \frac{\partial^\alpha u}{\partial z^\alpha} = g \, .$$

For non-stationary problems $z \in \Omega$ represents the variable in space as well as in time and α denotes a multi-index $\alpha = (\alpha_1, \ldots, \alpha_d) \in \mathbb{N}_0^d$ of the d-dimensional problem, where $|\alpha| = \sum_{i=1}^d \alpha_i$. Furthermore, let $L_h : G_h \to \mathbb{R}^d$ be the discrete approximation of L restricted on a grid G_h with spacing h. Using the discrete max norm $\| \cdot \|_\infty$, we define the consistency as follows.

Definition 8.5. *Let L_h be an approximation of a differential operator L as above, then L_h is called (discrete) consistent, if*

$$\left\| L_h(u|_{G_h}) - (Lu)|_{G_h} \right\|_\infty \to 0 \quad \textit{for} \quad h \to 0 \, .$$

The order of consistency is m, if

$$\left\| L_h(u|_{G_h}) - (Lu)|_{G_h} \right\|_\infty = \mathcal{O}\left(h^m\right) \, . \tag{8.25}$$

[117]

Applied on the derived prototypes for the considered partial differential equations, we state:

Theorem 8.1.

(i) *The order of consistency for the approximation (8.23) is $\mathcal{O}(\Delta t)$ for $u \in C^{0,2}(\Omega)$.*

(ii) *The order of consistency for the approximation (8.24) is $\mathcal{O}(\Delta z + \Delta t)$ for $u \in C^{4,2}(\Omega)$ and $\sigma \in \{0, 1\}$.*

Proof. The proof is provided in Appendix G. □

However, the consistency alone is not sufficient to ensure convergence. A finite difference method can be consistent, in other words a good approximation of a differential operator, without being stable. The stability is a measure of the influence of small disturbances on the solution, i. e., the stability does not describe the quality of the approximation of the differential operator but the approximative solution itself. Only a combination of consistency and stability provides a convergent method. Hence, we define and analyze the stability of a method.

Definition 8.6. *Let L_h be an approximation of a differential operator L as above. Furthermore, let u_h be the solution of a discrete problem $L_h u_h = g_h$. Then an approximation is called (discrete) stable, if*

$$\|u_h\|_\infty \leq C \cdot \|g_h\|_\infty \,, \tag{8.26}$$

where the constant $C \geq 0$ is independent of the spacing h.[117]

For the applied approximations stability is given under the following assumptions.

Theorem 8.2.

(i) *The approximation (8.23) is stable.*

(ii) *The approximation (8.24) is stable for*

- ***(a)*** $1 + d_j^n \Delta z \geq 0$
- ***(b)*** $e_j^n \leq 0$
- ***(c)*** $\left| -e_j^n + f_j^n \Delta t \right| \leq 1$
- ***(d)*** $-e_j^n - \theta(1-\sigma)(2 + d_j^n \Delta z) + f_j^n \Delta t \geq 0$

$\forall j \in \{0, \ldots, J\}, n \in \{0, \ldots, N\}$ *and* $\theta = \frac{\Delta t}{(\Delta z)^2}$.

Proof. The proof is provided in Appendix G. □

Finally, we define the convergence of a method.

Definition 8.7. *Let L_h be an approximation of a differential operator L as above. Furthermore, u_h is the solution of the discrete problem $L_h u_h = g|_{G_h}$, then L_h is called convergent, if*

$$\left\| u_h - u|_{G_h} \right\|_\infty \to 0 \quad \textit{for} \quad h \to 0 \,.$$

The order of convergence is m, if

$$\left\| u_h - u|_{G_h} \right\|_\infty = \mathcal{O}\left((h)^m\right) \,. \tag{8.27}$$

[117]

Based on Lax' equivalence theorem[133] consistency and stability are necessary and sufficient to ensure the convergence of a method.

Theorem 8.3. *Let L_h be a consistent and stable approximation of a differential operator L in the meaning of Definition 8.5 and 8.6. Furthermore, let u_h be the solution of $L_h u_h = g_h$, then the approximation is convergent, and the order of convergence equals the order of consistency.*

Proof. Based on the stability defined in equation (8.26) and the linearity of the approximation, we can state

$$\begin{aligned}\|u_h - u|_{G_h}\|_\infty &\leq C\|L_h(u_h - u|_{G_h})\|_\infty \\ &= C\|L_h u_h - L_h(u|_{G_h})\|_\infty \\ &= C\|g_h - L_h(u|_{G_h})\|_\infty \\ &= C\|(Lu)|_{G_h} - L_h(u|_{G_h})\|_\infty \ .\end{aligned}$$

The claim follows from the consistency defines in equation (8.25)

$$\left\|u_h - u|_{G_h}\right\|_\infty = \mathcal{O}\left((h)^m\right) \ .$$

□

Thus, under the stability criteria in Theorem 8.2 both approximations in equation (8.23) and in equation (8.24) are convergent, and so is the numerical implementation of the methods. Nonetheless, the validity of the stability criteria has to be ensured and verified for every individual problem.

Applying the parameters d_j^n, e_j^n and f_j^n of the reaction-diffusion equation and the growth of Li_2O_2 in porous structures on the stability criteria, results in severe constraints on the time step/spatial resolution ratio $\Delta t/\Delta z$ as well as on the threshold in the implemented lateral propagation scheme (see Sections 8.3 and 9.1). Furthermore, the demand for convergence and hence the validity of the stability criteria reveals the huge advantage of the implicit scheme in comparison with the explicit due to the use of much larger time steps at comparable accuracy. A detailed discussion of the validity of the stability criteria in the present problem as well as the derivation of the lower and upper limits for the $\Delta t/\Delta z$-ratio are carried out in Section 9.2.

CHAPTER 9

NUMERICAL IMPLEMENTATION

The discretization of the two applied solvers, the implicit and the explicit method, are shown in the following chapter. Subsequently, the methods are analyzes with regard to the stability criteria and briefly shown in a pseudo-code formulation.

Apart from the finite difference method, we introduce and discuss the Greedy algorithm which is used to determine the optimal catalyst number and positioning. Furthermore, the parallelization method implemented in the Greedy algorithm is explained and illustrated in a benchmark test. Finally, the implicit and the explicit method are compared with regard to their accuracy and efficiency for the continuous model as well as for the discrete model of catalysts in the Greedy algorithm.

9.1. Discretization of the implicit and the explicit method

Time discretization The discretization of dimensionless time t in the two differential equations (8.14) and (8.15)

$$\partial_t r = -\gamma c \qquad \text{and} \qquad \partial_t (r^{\frac{4}{3}} c) = \partial_z \left(r^2 \cdot \partial_z c \right) - \beta \cdot r^{\frac{1}{3}} c$$

is approximated according to Definition 8.4 in Section 8.4.2 using a forward difference

$$\partial_t r \approx \frac{1}{\Delta t} \left(r_j^{n+1} - r_j^n \right) \quad \text{and} \quad \partial_t c \approx \frac{1}{\Delta t} \left(c_j^{n+1} - c_j^n \right) ,$$

where $\Delta t = N^{-1}$ is the discrete time step. Thus, the radius in the next time step is calculated directly via

$$r_j^{n+1} = r_j^n - \Delta t \gamma c_j^n \quad \text{for} \quad j = 0, \dots, J \quad \text{and} \quad n = 0, \dots, N \tag{9.1}$$

using the discrete initial conditions for $n = 0$

- $r_j^0 = 1$ for $j = 0, \dots, J$
- $c_j^0 = 0$ for $j = 1, \dots, J$

and the Dirichlet boundary conditions for $j = 0$

- $c_0^n = 1$ for $n = 0, \dots, N$.

Explicit space discretization In the explicit approach we approximate the derivatives with respect to space z using a forward difference for the radius relative to position j and for the concentration relative to $j + 1$ according to

$$\partial_z r \approx \frac{1}{\Delta z}\left(r_j^n - r_{j-1}^n\right) \quad \text{and} \quad \partial_z c \approx \frac{1}{\Delta z}\left(c_{j+1}^n - c_j^n\right) ,$$

for the second derivative using a central difference

$$\partial_{zz} c \approx \frac{1}{(\Delta z)^2}\left(c_{j+1}^n + c_{j-1}^n - 2c_j^n\right) ,$$

where $\Delta z = J^{-1}$ is the discrete spatial resolution. The index shift in the first equation results from the coupling of the two partial differential equations and is required for the numerical calculation of the coefficients that determine the concentration in the next time step. The concentration is then calculated applying the approximations to equation (8.15) according to

$$c_j^{n+1} = a_{jj-1}^n \cdot c_{j-1}^n + a_{jj}^n \cdot c_j^n + a_{jj+1}^n \cdot c_{j+1}^n \quad \text{for} \quad j = 1, \dots, J-1, \quad n = 0, \dots, N . \tag{9.2}$$

The coefficients are given by

$$\begin{aligned}
a_{jj-1}^n &= \frac{\Delta t}{(\Delta z)^2}\left(r_j^n\right)^{\frac{2}{3}} \\
a_{jj}^n &= \frac{\Delta t}{(\Delta z)^2}\left(r_j^n\right)^{-\frac{1}{3}} 2\left(r_{j-1}^n - 2r_j^n\right) + \left(r_j^n\right)^{-1}\left[\frac{1}{3}\left(7r_j^n - 4r_j^{n+1}\right) - \beta \Delta t\right] \\
a_{jj+1}^n &= \frac{\Delta t}{(\Delta z)^2}\left(r_j^n\right)^{-\frac{1}{3}}\left(3r_j^n - 2r_{j-1}^n\right) .
\end{aligned}$$

Once again we refer to the initial conditions and Dirichlet boundary conditions for the left boundary. For the right boundary ($j = J$) Neumann boundary conditions are applied, according to

- $c_{J+1}^n = c_J^n$

and the concentration is set to $c_J^{n+1} = a_{JJ-1}^n \cdot c_{J-1}^n + (a_{JJ}^n + a_{JJ+1}^n) \cdot c_J^n$ for every time n. Thus, in the explicit space discretization the concentration can be calculated directly using equation (9.2), as in the case of time discretization.

Implicit space discretization The space discretization in the implicit approach is performed using the concentration in the next time step $n+1$ according to

$$\partial_z r \approx \frac{1}{\Delta z}\left(r_j^n - r_{j-1}^n\right) \quad \text{and} \quad \partial_z c \approx \frac{1}{\Delta z}\left(c_{j+1}^{n+1} - c_j^{n+1}\right)$$

and

$$\partial_{zz} c \approx \frac{1}{(\Delta z)^2}\left(c_{j-1}^{n+1} - 2c_j^{n+1} + c_{j+1}^{n+1}\right) .$$

Analogously to the explicit approach, the indexing is shifted to ensure the calculation of the coefficient matrix.

The concentration in the next time step is calculated via

$$c_j^n = a_{jj-1}^n \cdot c_{j-1}^{n+1} + a_{jj}^n \cdot c_j^{n+1} + a_{jj+1}^n \cdot c_{j+1}^{n+1} \quad \text{for} \quad j = 1, \ldots, J-1, \quad n = 0, \ldots, N \tag{9.3}$$

applying the approximations to equation (8.14) in the previous chapter. The coefficients are given by

$$\begin{aligned}
a_{jj-1}^n &= \frac{\Delta t}{(\Delta z)^2}\left(r_j^n\right)^{\frac{2}{3}}\left[\frac{1}{3}\left(4r_j^{n+1} - 7r_j^n\right)\right]^{-1} \\
a_{jj}^n &= \left[\frac{\Delta t}{(\Delta z)^2}\left(r_j^n\right)^{\frac{2}{3}} 2\left(r_{j-1}^n - 2r_j^n\right) - r_j^n\right]\left[\frac{1}{3}\left(4r_j^{n+1} - 7r_j^n\right)\right]^{-1} \\
a_{jj+1}^n &= \frac{\Delta t}{(\Delta z)^2}\left(r_j^n\right)^{\frac{2}{3}}\left(3r_j^n - 2r_{j-1}^n\right)\left[\frac{1}{3}\left(4r_j^{n+1} - 7r_j^n\right)\right]^{-1} .
\end{aligned}$$

Furthermore, we obtain $c_J^n = a_{JJ-1}^n \cdot c_{J-1}^{n+1} + (a_{JJ}^n + a_{JJ+1}^n) \cdot c_J^{n+1}$ using Neumann boundary conditions for the right boundary and for the left boundary $j = 1$

$$c_1^n = a_{10}^n \cdot c_0^{n+1} + a_{11}^n \cdot c_1^{n+1} + a_{12}^n \cdot c_2^{n+1} \quad \Leftrightarrow \quad c_1^n - a_{10}^n \cdot c_0^{n+1} = a_{11}^n \cdot c_1^{n+1} + a_{12}^n \cdot c_2^{n+1} .$$

Thus, the system of equation can be written as

$$A\boldsymbol{c}^{n+1} = \boldsymbol{c}_j^n - \boldsymbol{corr}^n \ ,$$

where $\boldsymbol{corr}^n = \left(a_{10}^n \cdot c_0^{n+1}, 0, \ldots, 0\right)^T$ is a correction vector due to the Dirichlet boundary condition. The $J \times J$ system matrix A is given by

$$A = \begin{pmatrix} a_{11}^n & a_{12}^n & 0 & \cdots & 0 \\ a_{21}^n & a_{22}^n & a_{23}^n & & \vdots \\ 0 & \ddots & \ddots & \ddots & 0 \\ \vdots & & a_{J-1J-2}^n & a_{J-1J-1}^n & a_{J-1J}^n \\ 0 & \cdots & 0 & a_{JJ-1}^n & a_{JJ}^n + a_{JJ+1}^n \end{pmatrix} .$$

The system of equations, which determines the concentration in the next time step, is solved using a LU decomposition. The system matrix is partitioned in a lower triangular matrix L and an upper triangular matrix U. The two resulting systems of equations $L\boldsymbol{d}^{n+1} = \boldsymbol{c}^n - \boldsymbol{corr}^n$ and $U\boldsymbol{c}^{n+1} = \boldsymbol{d}^{n+1}$ are solved via a Gaussian elimination. Since the system matrix A is a strictly diagonally dominant tridiagonal matrix (see proof of stability in Appendix G), the matrix is invertible, and there exists a LU decomposition according to

$$L = \begin{pmatrix} 1 & & & \\ l_2 & 1 & & \\ & \ddots & \ddots & \\ & & l_J & 1 \end{pmatrix} \quad \text{and} \quad U = \begin{pmatrix} u_1 & a_{12}^n & & \\ & u_2 & \ddots & \\ & & \ddots & a_{J-1J}^n \\ & & & u_J \end{pmatrix} .$$

The coefficients are given by

$$u_1 = a_{11}^n, \quad l_j = \frac{a_{jj-1}^n}{u_{j-1}} \quad \text{and} \quad u_j = a_{jj}^n - l_j a_{j-1j}^n \quad \text{for} \quad j = 2, \ldots, J \ .$$

The concentration in the next time step is then calculated in two steps via

(i) $d_1^{n+1} = c_1^n - a_{10}^n c_0^{n+1}$ and $d_j^{n+1} = c_j^n - l_j d_{j-1}^{n+1}$ for $j = 2, \ldots, J$

(ii) $c_J^{n+1} = \frac{d_J^{n+1}}{u_J}$ and $c_j^{n+1} = \frac{d_j^{n+1} - a_{jj+1}^n c_{j+1}^{n+1}}{u_j}$ for $j = J-1, \ldots, 1$.

Discretization of the reaction rate The calculation of the parameters β and γ in equation (8.16) requires the knowledge of the reaction rate k. For this purpose, the integral in equation (8.17) is

approximated at every time step n using the trapezoidal rule (Appendix F, Definition F.9) via

$$Q^n(r^n c^n) = \Delta z \left[\frac{1}{2}\left(r_0^n c_0^n + r_J^n c_J^n\right) + \sum_{j=1}^{J-1} r_j^n c_j^n \right] . \tag{9.4}$$

Thus, we obtain a discrete reaction rate k^n

$$k^n = \underbrace{\frac{i r_p^0}{4F\epsilon^0 c_{O_2,0} l}}_{const.} \cdot \frac{1}{Q^n(r^n c^n)} \tag{9.5}$$

which is calculated at every time step n during the execution of the algorithm.

Discretization of the catalyst function The catalyst function is discretized via a switch function $cat_j^n : J \to \{0,1\}$, i. e., for a catalyst at position $j \in J$ we set $cat_j^n = 1$, otherwise zero. This function is used to modify the differential equation that determines the pore radius r in equation (9.1) according to

$$r_j^{n+1} = r_j^n - \Delta t \gamma c_j^n \cdot cat_j^n \quad \text{for} \quad j = 0, \ldots, J, \quad n = 0, \ldots, N . \tag{9.6}$$

The smooth growth of discharge product from the catalytic site along the pore wall is modeled in our discrete implementation using a simple propagation scheme that activates neighbor sites after the deposition of a certain fixed amount of Li_2O_2 at the initially defined position. Namely, once the radius r_j^n reaches a given threshold value S at time n, the catalytic function at the next neighbors of the position j is switched on via $cat_{j-1}^n = 1$ and $cat_{j+1}^n = 1$. The threshold is defined as the fraction $S = (r_j^0 - r_j^n)/r_j^0$ of the initially free radius $r_j^0 = 1$ becoming occupied by newly deposited material at time n.

9.2. Stability criteria applied on the implicit and the explicit method

Both approximations of the differential equations are consistent according to Theorem 8.1 for the explicit as well as the implicit method. However, to ensure stability and thus convergence all stability criteria in Theorem 8.2

(a) $1 + d_j^n \Delta x \geq 0$

(b) $e_j^n \leq 0$

(c) $\left| -e_j^n + f_j^n \Delta t \right| \leq 1$

(d) $-e_j^n - \theta(1-\sigma)(2 + d_j^n \Delta x) + f_j^n \Delta t \geq 0$

have to be fulfilled. The parameters in the present methods are given by

- $d_j^n = 2\left(r_j^n\right)^{-1}\left(r_j^n - r_{j-1}^n\right)\Delta z^{-1}$
- $e_j^n = -\left(r_j^n\right)^{-\frac{2}{3}}$
- $f_j^n = -\left(r_j^n\right)^{-\frac{5}{3}}\left(\frac{4}{3}\left(r_j^{n+1} - r_j^n\right)\Delta t^{-1} + \beta\right)$,

where $\beta = \underbrace{il\,/\left(2D_{O_2}F\epsilon_0^{\frac{3}{2}}c_{O_2,0}\right)}_{const.} \cdot \left[\Delta z\left(\frac{1}{2}\left(r_0^n c_0^n + r_J^n c_J^n\right) + \sum_{j=1}^{J-1} r_j^n c_j^n\right)\right]^{-1}$ according to equation (8.16) and the discretization of the reaction rate constant in equation (9.5).

to (a) Using parameter d_j^n we can write the first criterion as

$$\frac{r_{j-1}^n}{r_j^n} \leq \frac{3}{2}\,. \tag{9.7}$$

For a continuous catalyst distribution it is true that $r_{j-1}^n \geq r_j^n$ for all grid points j, however, choosing a reasonable (fine) discretization, large leaps between neighboring pore radii r_j^n and r_{j-1}^n are avoided and the criterion is valid.

In the case of a localized growth the criterion can be violated easier by an improper choice of the threshold (see Section 9.6, Discrete model). Thus, criterion **(a)** is a strong restriction on the threshold value and hence on the growth mechanisms that can be modeled (the impact of the threshold on the applied growth mechanism is discussed in detail at the end of Section 9.6).

to (b) Criterion **(b)** is always valid for both methods since $r_j^n \geq 0\ \forall j, n$.

to (c) Criterion **(c)** can be written as $-e_j^n + f_j^n \Delta t \leq 1$ and $-e_j^n + f_j^n \Delta t \geq -1$. The resulting restrictions are

$$\frac{\Delta t}{\Delta z} \geq const \cdot \left[\frac{1}{2}\left(\left(r_0^n\right)^{\frac{1}{3}} c_0^n + \left(r_J^n\right)^{\frac{1}{3}} c_J^n\right) + \sum_{j=1}^{J-1}\left(r_j^n\right)^{\frac{1}{3}} c_j^n\right]\left[\frac{1}{3}\left(7r_j^n - 4r_j^{n+1}\right) - \left(r_j^n\right)^{-\frac{5}{3}}\right] \tag{9.8}$$

and

$$\frac{\Delta t}{\Delta z} \leq const \cdot \left[\frac{1}{2}\left(\left(r_0^n\right)^{\frac{1}{3}} c_0^n + \left(r_J^n\right)^{\frac{1}{3}} c_J^n\right) + \sum_{j=1}^{J-1} \left(r_j^n\right)^{\frac{1}{3}} c_j^n\right] \left[\frac{1}{3}\left(7r_j^n - 4r_j^{n+1}\right) + \left(r_j^n\right)^{-\frac{5}{3}}\right].$$

Thus, there is a linear dependency between the time step and the spatial resolution for both methods.

to (d) The last criterion is analyzed for the explicit ($\sigma = 0$) and the implicit method ($\sigma = 1$) separately. The implicit approach results in the criterion

$$\frac{\Delta t}{\Delta z} \leq const \cdot \left[\frac{1}{2}\left(\left(r_0^n\right)^{\frac{1}{3}} c_0^n + \left(r_J^n\right)^{\frac{1}{3}} c_J^n\right) + \sum_{j=1}^{J-1} \left(r_j^n\right)^{\frac{1}{3}} c_j^n\right] \left[\frac{1}{3}\left(7r_j^n - 4r_j^{n+1}\right)\right] \tag{9.9}$$

which is stronger than the upper restriction of criterion **(c)** since $r_j^n \geq 0 \; \forall j, n$.

The explicit method results in a quadratic dependency (highlighted in red) between the time step and the spatial resolution according to

$$\frac{\Delta t}{(\Delta z)^2} + \frac{\Delta t}{\Delta z} \cdot const. \left[\frac{1}{2}\left(\left(r_0^n\right)^{\frac{1}{3}} c_0^n + \left(r_J^n\right)^{\frac{1}{3}} c_J^n\right) + \sum_{j=1}^{J-1} \left(r_j^n\right)^{\frac{1}{3}} c_j^n\right]^{-1} \left[2\left(r_j^n\right)^{\frac{2}{3}} \left(2r_j^n - r_{j-1}^n\right)\right]^{-1}$$
$$\leq \frac{1}{3}\left(r_j^n - 4r_j^{n+1}\right) \left[2\left(r_j^n\right)^{\frac{2}{3}} \left(2r_j^n - r_{j-1}^n\right)\right]^{-1}. \tag{9.10}$$

Since the upper as well as the lower limit are not accessible in a straightforward way, the choice of time step and spatial resolution is based on the concentration domain and is introduced in Section 9.6. However, criterion **(c)** reveals the vast advantage of a linear dependency between time step and spatial resolution in the implicit approach. The explicit method offers a straightforward implementation and a direct calculation of the concentration in the next time step, while the implicit method requires a more complex implementation for the solution of a system of equations. Nonetheless, the concomitant computational effort as well as the higher need for memory space do not outweigh the higher stability of the implicit method due to the use of distinctly larger time steps at comparable accuracy, what is shown and discussed in Section 9.6 in detail.

9.3. Greedy algorithm

The determination of the optimal number and distribution of catalysts to maximize the pore volume utilization is based on a Greedy algorithm. The strategy of Greedy algorithms is the step-by-step choice of a subsequent state that is selected on the basis of the minimization of an objective function. A characteristic property of Greedy algorithms is the irreversibility of already taken decisions. Due to this property and the restriction to a local minimization, Greedy algorithms do not always result in a global minimum. An optimal solution requires an optimal substructure and is ensured solely on matroids (specified in Appendix F, Definition F.8).[118]

To illustrate the procedure of a Greedy algorithm for the catalyst positioning, we transfer the idea in a graph-theoretical model: Starting from the source node (vertex) the outdegree equals the number of catalyst positions J, i. e., the directed graph branches in the number of possible positions. The finite difference method is proceeded for every node until pore clogging is attained at time N. Since the pore geometry and hence the pore surface are kept constant, we choose the remaining free pore volume V_{free} as an objective function to evaluate the quality of the catalyst position. The minimization of V_{free} is equivalent to the maximization of the amount of discharge product Li_2O_2 and hence the capacity of the battery at a constant cathode volume. The free pore volume represents the edge weights (costs) in the graph-theoretical picture, and is calculated numerically according to

$$V_{free}^{n} = \Delta z \left[\frac{1}{2} \left(\left(r_0^n\right)^2 + \left(r_J^n\right)^2 \right) + \sum_{j=1}^{J-1} \left(r_j^n\right)^2 \right] \tag{9.11}$$

using the trapezoidal rule (Appendix F, Definition F.9) to approximate the integration. Following the Greedy idea, we choose the node with the (locally) minimum free pore volume. In the next step the catalyst is fixed on the selected position, and the procedure is repeated for the $J-1$ remaining edges. Again the calculated free pore volumes for the new configuration of catalysts (the fixed catalyst and a newly set one) determine the choice of the next catalyst position. The algorithm stops if no further improvement can be achieved, i. e., $V_{free}^{n} > V_{free}^{n-1} = V_{free}^{N}$ in the nth iteration step. The applied Greedy algorithm trivially results in a feasible solution but not necessarily in an optimal one, as can be seen in a small example in Figure 9.1.

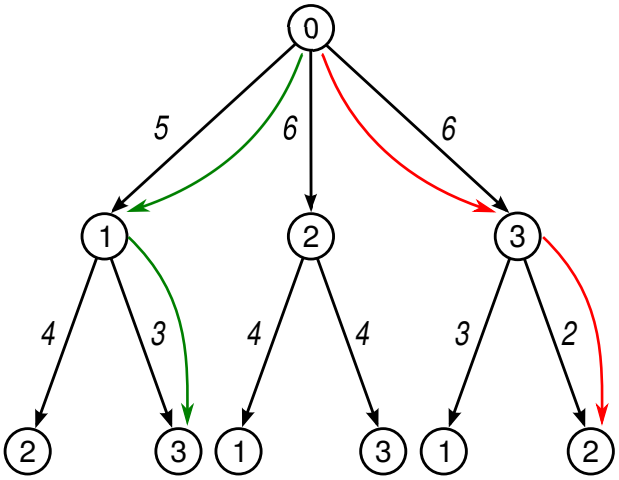

Figure 9.1.: Procedure and optimal solution in the Greedy algorithm (green) and the global optimal solution (red) on an example.

While the Greedy algorithm follows the green way of minimum edge weights (local minima) with catalyst positions {1,3}, the globally optimal way is the red one with catalyst positions {3,2} resulting in the minimum free pore volume of 2 (minimum edge weight) which is not chosen due to the lack of an optimal substructure. Despite the possibility not to gain the globally optimal solution or to obtain even the worst possible solution,[118] the Greedy approach is an outstanding optimization heuristic due to its comparably fast runtime and straightforward objective function. To clarify whether the Greedy algorithm results in a good solution for the considered problem, we analyze the process of pore clogging in a qualitative way. For a continuous growth a fast clogging of the pore occurs at the oxygen supplying entrance. Therefore, we expect a dense catalyst occupation at the end of the pore for the optimal catalyst distribution, which decreases to the pore entrance side in a reverse way as the deposition of Li_2O_2. This behavior has been observed in the present study, suggesting a (locally) optimal solution.

In general, we cannot assume an optimal substructure for the considered problem of catalyst positioning. The complex free volume landscape shown exemplary for the $DMSO^{Li^+}$ electrolyte for the first eight steps of the Greedy algorithm in Figure 9.10 suggest even a lack of one. Thus, instead of verifying or falsifying the existence of an optimal substructure via a test of the validity of all three properties of matroids (Appendix F, Definition F.8), which is beyond the scope of the algorithmic section, we demonstrate the absence on a simple counterexample. For this purpose, we calculate the distribution of the first three catalysts on 34 possible catalyst positions via the Greedy algorithm (minimum number of discretization points with at least three catalysts in the optimal solution). This distribution is then compared with all feasible solutions

$$\binom{n}{k} = \frac{n!}{k!(n-k)!},$$

where $n = 34$ and $k = 3$, hence, 5984 possible arrangements of three catalysts. The resulting free volumes in descending order are shown in Figure 9.2 along with the free volume obtained from the

Greedy algorithm. The global optimum provides a free volume of $V_{free} = 8.12\,\%$ and a catalyst distribution with positions at $(32, 33, 34)$, while the Greedy algorithm results in $V_{free} = 8.21\,\%$ and $(31, 32, 33)$. The difference is due to a local minimum of the free volume at position 31 in the first step of the Greedy algorithm. In consequence of the irreversibility of the selected position in the first step, the Greedy algorithm results in a slightly different optimal solution. However, both solutions are very close to each other in this early stage of the optimization algorithm (second best free volume and similar catalyst positioning), indicating that the Greedy optimal distribution is close to the global minimum.

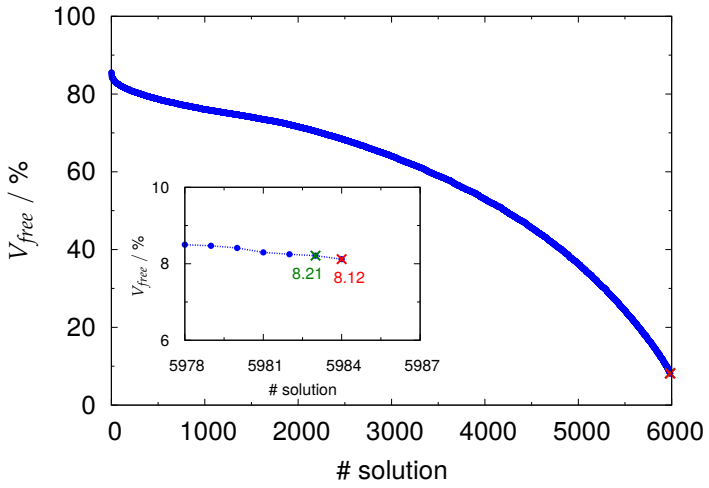

Figure 9.2.: Greedy optimal free volume (green) in comparison with all feasible solutions in descending order (blue) and the global minimum (red) of three catalysts on 34 possible catalyst positions in the $DMSO^{Li^+}$ electrolyte at a threshold of 6 %.

9.4. Pseudo codes of the finite difference method and the Greedy algorithm

The implicit and the explicit method as well as the Greedy algorithm are implemented in the programming language C++. In the following each finite differences approach and a combination with the optimization heuristic are shown as pseudo codes for the Algorithms 9.1, 9.2 and 9.3. In the implicit case identical code parts to the explicit method are shown in gray to highlight the differences between both approaches.

Algorithm 9.1: `Implicit finite difference method`

Data: $\Delta z, \Delta t, \beta, \gamma, J, S, EPS, cat_j^0, a_{jj}^n$ for $j = 0, \ldots, J$

Result: r_j^N, c_j^N for $j = 0, \ldots, J$

for $j = 0, \ldots, J$ **do**
  $r_j^0 = 1$; // initial condition for the pore radius
end
for $j = 1, \ldots, J$ **do**
  $c_j^0 = 0$; // initial condition for the concentration
end
$c_0^0 = 1$;
$n = 0$;
repeat
  $k = const. \left[\Delta z \left(\frac{1}{2} \left(\left(r_0^n \right)^{\frac{1}{3}} c_0^n + r_J^n c_J^n \right) + \sum_{j=1}^{J-1} \left(r_j^n \right)^{\frac{1}{3}} c_j^n \right) \right]^{-1}$; // reaction rate constant
  for $j = 0, \ldots, J$ **do**
    $r_j^{n+1} = r_j^n - \Delta t \gamma cat_j^n c_j^n$; // pore radius in the next time step
  end
  $u_1 = a_{11}^n$; // LU decomposition
  for $j = 2, \ldots, J$ **do**
    $l_j = \frac{a_{jj-1}^n}{u_{j-1}}$;
    $u_j = a_{jj}^n - l_j a_{j-1j}^n$;
  end
  $d_1^{n+1} = c_1^n - a_{10}^n c_0^{n+1}$;
  for $j = 2, \ldots, J$ **do**
    $d_j^{n+1} = c_j^n - l_j d_{j-1}^{n+1}$;
  end
  $c_0^{n+1} = c_0^n$; // boundary conditions for the concentration
  $c_J^{n+1} = \frac{d_J^{n+1}}{u_J}$;
  for $j = J-1, \ldots, 1$ **do**
    $c_j^{n+1} = \frac{d_j^{n+1} - a_{jj+1}^n c_{j+1}^{n+1}}{u_j}$; // concentration in the next time step
  end
  for $j = 0, \ldots, J$ **do**
    // check the threshold
    if $r_j^{n+1} < S$ **then**
      $cat_{j-1}^n = 1$;
      $cat_{j+1}^n = 1$;
    end
  end
  n++;
until $r_j^{n+1} \leq EPS$ for a j ;
$N = n$;

Algorithm 9.2: `Explicit finite difference method`

Data: $\Delta z, \Delta t, \beta, \gamma, J, S, EPS, cat_j^0, a_{jj}^n$ for $j = 0, \ldots, J$

Result: r_j^N, c_j^N for $j = 0, \ldots, J$

for $j = 0, \ldots, J$ **do**

  $r_j^0 = 1;$ // initial condition for the pore radius

end

for $j = 1, \ldots, J$ **do**

  $c_j^0 = 0;$ // initial condition for the concentration

end

$c_0^0 = 1;$

$n = 0;$

repeat

  $k = const. \left[\Delta z \left(\frac{1}{2} \left(\left(r_0^n \right)^{\frac{1}{3}} c_0^n + r_J^n c_J^n \right) + \sum_{j=1}^{J-1} \left(r_j^n \right)^{\frac{1}{3}} c_j^n \right) \right]^{-1};$ // reaction rate constant

  for $j = 0, \ldots, J$ **do**

    $r_j^{n+1} = r_j^n - \Delta t \gamma cat_j^n c_j^n;$ // pore radius in the next time step

  end

  for $j = 1, \ldots, J-1$ **do**

    $c_j^{n+1} = a_{jj-1}^n \cdot c_{j-1}^n + a_{jj}^n \cdot c_j^n + a_{jj+1}^n \cdot c_{j+1}^n;$ // concentration in the next time step

  end

  $c_0^{n+1} = c_0^n;$ // boundary conditions for the concentration

  $c_J^{n+1} = a_{JJ-1}^n \cdot c_{J-1}^n + (a_{JJ}^n + a_{JJ+1}^n) \cdot c_J^n;$

  // check the threshold

  for $j = 0, \ldots, J$ **do**

    if $r_j^{n+1} < S$ **then**

      $cat_{j-1}^n = 1;$

      $cat_{j+1}^n = 1;$

    end

  end

  n++;

until $r_j^{n+1} \leq EPS$ for a j ;

$N = n;$

Algorithm 9.3: `Greedy algorithm`

Data: $\Delta z, \Delta t, \beta, \gamma, J, S, EPS, a_{jj}$ for $j = 0, \ldots, J$

Result: $V_{free}^N, r_j^N, c_j^N, cat_j$ for $j = 0, \ldots, J$

$V_{free}^0 = 1$; // initialize volume

for $j = 0, \ldots, J$ **do**

  $cat_j = 0$; // initialize catalysts

end

repeat

  // Greedy iteration step

  for $j = 0, \ldots, J$ **do**

    if $cat_j \neq 1$ **then**

      $cat_j = 1$;

      `implicit/explicit finite difference method`;

      $V_{free,j}^n = \Delta z \left[\frac{1}{2} \left(\left(r_0^n \right)^2 + \left(r_J^n \right)^2 \right) + \sum_{j=1}^{J-1} \left(r_j^n \right)^2 \right]$; // free pore volume

    end

  end

  $V_{free}^n = \min_j \{ V_{free,j}^n \}$; // minimum free pore volume

  if $V_{free}^n < V_{free}^{n-1}$ **then**

    $V_{free}^{n-1} = V_{free}^n$; // update free pore volume

    for $j = 0, \ldots, J$ **do**

      $cat_j = cat_j^{min}$; // update catalysts

    end

    n++;

  else

    switch $= 1$;

  end

until switch $\neq 1$;

9.5. Parallelization and scaling behavior

The principle of the Greedy algorithm is based on the idea to calculate all feasible solutions in an iteration step and choose the optimal one according to the determining quantity of the free pore volume. Since the calculation of the individual solutions in a Greedy iteration step are independent from each other, the algorithm provides the opportunity of (ideal) parallelization.

The applied method for parallelization in the present work is the programming interface OpenMP (Open Multi-Processing).[134] The crucial advantage of this software is the parallelization of single parts of a process, so-called threads, which, however, require a shared memory. An example for such a system are the cores P of a single computer. Although other approaches such as MPI (Message Passing Interface), in which whole processes are parallelized, provide a higher level of parallelization, they might be very time consuming due to the required communication, synchronization, and exchange of data files between single processes. An example for such a system is a cluster of computers which communicate via a network between the distributed memory. The two parallelization methods are shown schematically in Figure 9.3. In modern high performance and supercomputing a combination of both approaches is used.

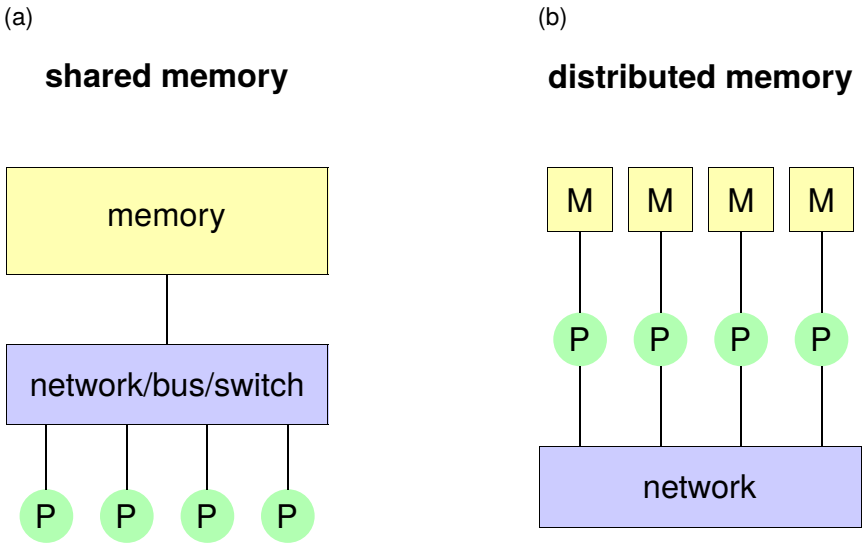

Figure 9.3.: Approaches to parallelization via (a) a shared memory (OpenMP) and (b) a distributed memory (MPI).[135]

Using OpenMP, all independent solutions in a Greedy step are calculated simultaneously. Since the code still holds parts that have to be handled sequentially, we analyze the scaling behavior and the time saving with respect to the number of cores. For this purpose, we perform several steps of

the implicit method within the electrolyte DMSO$^{Li^+}$ using a threshold of 1% for a varying number of cores P $=$ 1, 2, 4, 5, 10, 20, 25. The maximum number of provided cores is 32, however, due to the spatial resolution J = 100, the number of cores is chosen as a divider of the initial 100 parallelizable threads and limited to 25. Figure 9.4 shows the resulting scaling behavior in comparison to an ideal linear scaling. Although the applied parallelization shows a good scaling behavior and hence implies an enormous time saving, the sequential parts inhibit an ideal scaling, in particular the sequential input/output processing is seriously limiting.

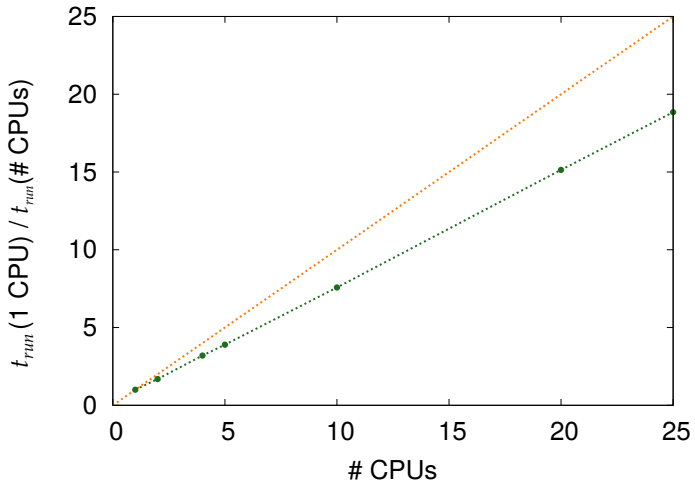

Figure 9.4.: Scaling behavior of the parallelized Greedy algorithm (green) for the implicit method in comparison to an ideal linear scaling (orange).

9.6. Comparison between the implicit and the explicit method

Continuous model The comparison between the implicit and the explicit method is carried out using DMSO$^{Li^+}$ as an exemplary electrolyte. Both methods are applied on four different numbers of space discretization points $J = 100$, 200, 300 and 400. The resulting growth profiles and the corresponding concentrations are shown in Figure 9.5 (a) for the implicit and (b) for the explicit method. The oxygen reservoir is located here and in the following on the left side. The applied time steps, which can be found in Table 9.1, are the largest time steps for which stability is not violated until the termination condition is achieved, but not larger than the spatial resolution Δz.

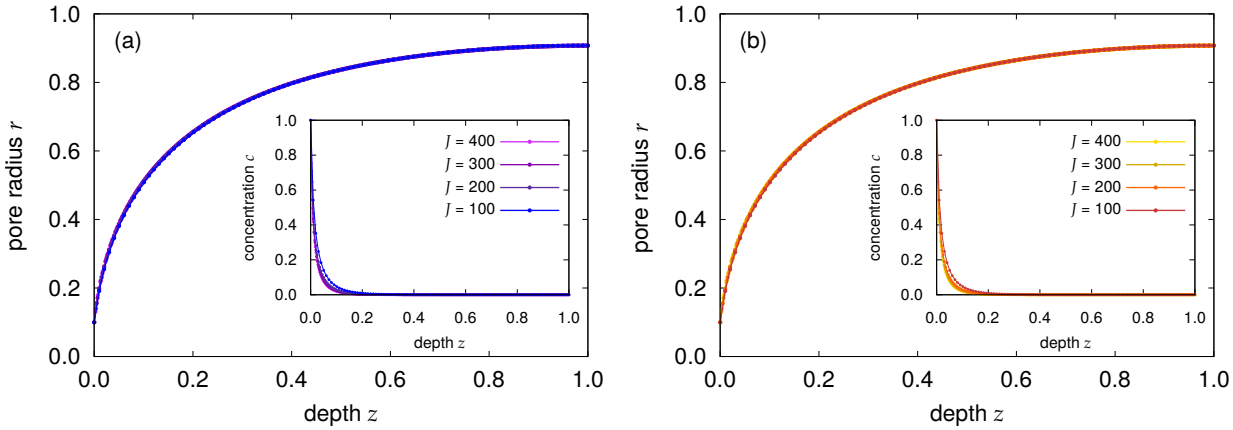

Figure 9.5.: Growth profiles and concentrations as inlays for (a) the implicit and (b) the explicit method for different numbers of space discretization points J.

Thereby, the stability is revised via the value of the normalized concentration at every time step instead of the computationally intensive stability criteria. As soon as the concentration exceeds the domain $c \in [0,1]$, the algorithm is stopped and the time step is decreased. Apart from the number of space and time discretization points, Table 9.1 shows the remaining free pore volume after pore clogging, the relative deviation

$$\sigma_{V_{free}} = \frac{\left| V_{free}^{exp} - V_{free}^{imp} \right|}{V_{free}^{exp}} ,$$

and the runtime t_{run} for the implicit and the explicit method.

Table 9.1.: Free pore volume, relative deviation, and runtime for the implicit and the explicit method.

J	$(\Delta t)^{-1}$		V_{free} / %		$\sigma_{V_{free}}$ / %	t_{run} / s	
	implicit	explicit	implicit	explicit		implicit	explicit
100	100	24000	61.6157	61.6152	0.0008	20.10	4762
200	200	92000	61.7067	61.7063	0.0006	82.01	37165
300	300	201000	61.7335	61.7332	0.0005	182.91	115751
400	400	352000	67.7460	61.7457	0.0004	326.21	268083

Pore clogging (termination condition) is defined as the point in time when the dimensionless pore radius r decreases below 0.1.

The relative deviation between the implicit and the explicit method is below 0.001 % and decreases even further with increasing number of space discretization points, while the runtime

increases enormously. The time evolution in the pore clogging and the concentration drop are visualized in Figure 9.6 for the implicit and the explicit method for a space discretization of J = 100.

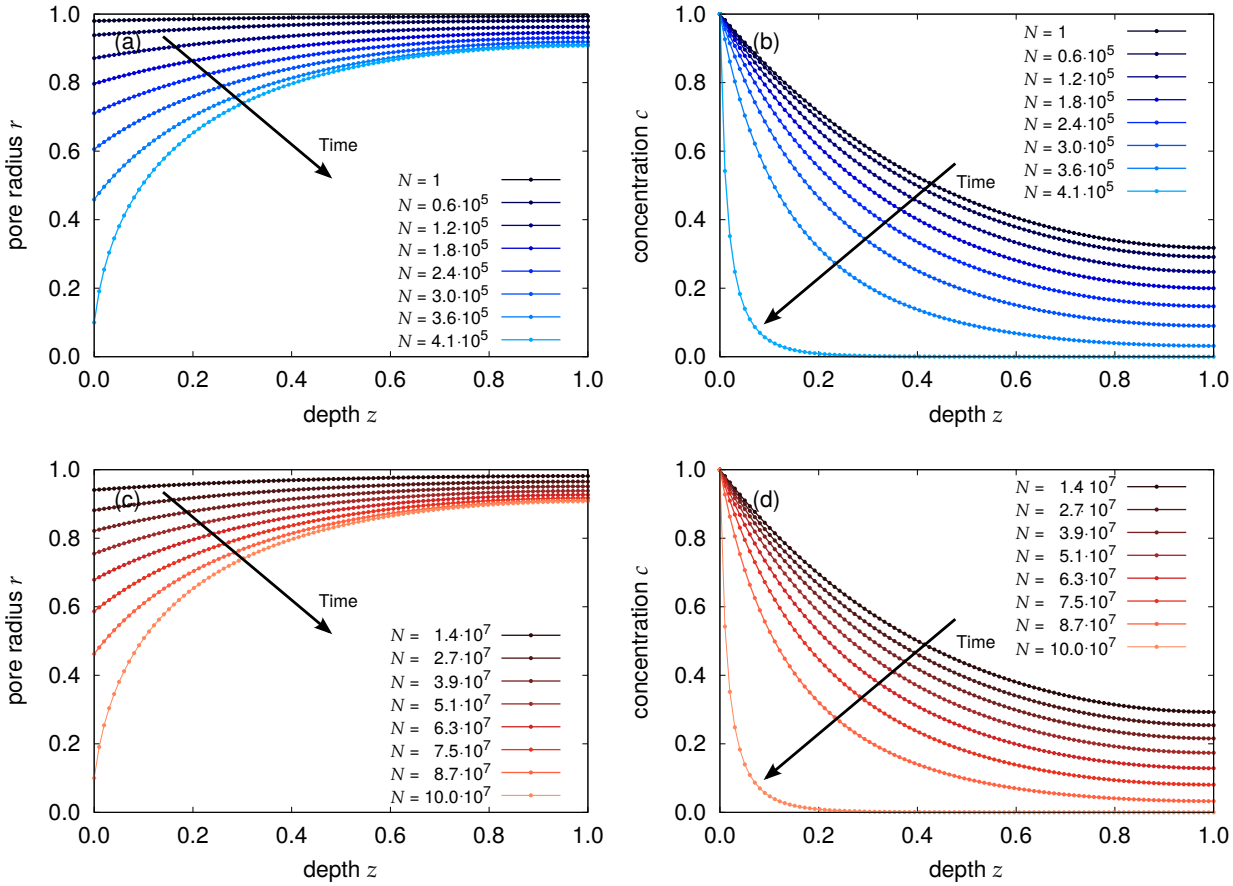

Figure 9.6.: Time evolution in (a) the growth and (b) the concentration for the implicit (blue) and (c) the growth and (d) the concentration for the explicit (red) method for a space discretization of J = 100. Screenshots of the progression are taken every N time steps.

Thus, in the present continuous model of growth no disadvantages arise from the use of the implicit method for the determination of the free pore volume. For the analysis of the actual runtime with respect to J we fit the time of each method via the function $t_{run}(J) = a_1 \cdot J^p + a_0$. Due to the few points an exact analysis of the scaling behavior is not possible, however, the applied regression analysis provides a very good estimation for the exponent p. The resulting scaling behavior with increasing J, as can be seen in the regression analysis in Figure 9.7, is quadratic in the case of the implicit method and cubic for the explicit one.

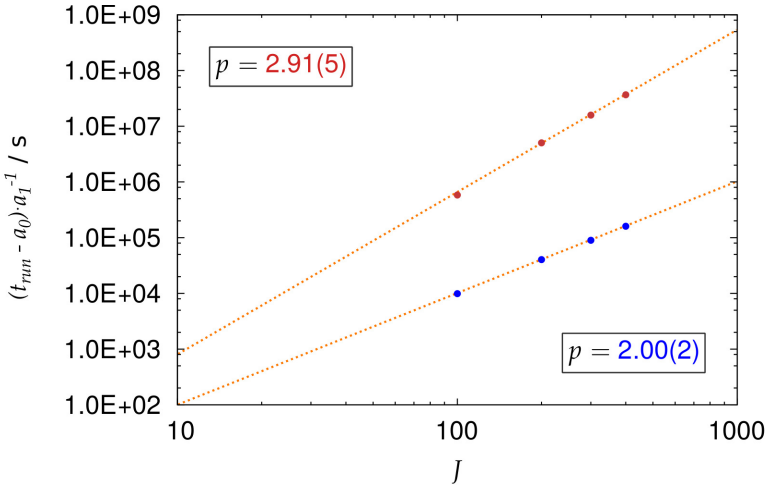

Figure 9.7.: Runtime with respect to the number of space discretization points for the implicit (blue) and the explicit (red) method with corresponding regression analysis (orange).

This behavior is also evident from theoretical considerations. In the explicit method according to equation (9.2) $\mathcal{O}(J)$ arithmetic operations are required for the direct computation of the concentration at every time step at every point $j = 1, \cdots, J$. If we refine the space discretization, simultaneously the time step is decreasing quadratically, i. e., the last stability criterion in Section 9.2, equation (9.10) is dominated by the dependency

$$\frac{1}{\Delta t} \propto \frac{1}{(\Delta z)^2} = \mathcal{O}(J^2) \; .$$

Thus, the overall computational effort for the explicit method is of the order $\mathcal{O}(J^3)$.

In the implicit method the concentration is not accessible directly but requires the solution of a system of equations. Inverting the coefficient matrix causes a computational effort of the order $\mathcal{O}(J^3)$ at every time step. However, the applied LU decomposition as well as the tridiagonal form of the coefficient matrix reduce the computational effort significantly. The LU decomposition of a $J \times J$ matrix is dominated by the $(J-k)^2$ multiplications and subtractions for every elimination step k, i. e.,

$$\sum_{k=1}^{J-1} (J-k)^2 = \sum_{i=1}^{J-1} i^2 = \frac{1}{2}(J-1)J(2(J-1)+1) = \mathcal{O}(J^3) \; .$$

The solution of the system of equations via Gaussian elimination is only of subordinate order $\mathcal{O}(J^2)$.[136] In the case of band matrices with bandwidths q and p the computational effort is reduced to $\mathcal{O}(J \cdot p \cdot q)$. Consequently, in the particular case of tridiagonal matrices with $p = q = 1$ we obtain a linear scaling behavior $\mathcal{O}(J)$. Considering again the stability criteria in Section 9.2,

equation (9.9)

$$\frac{1}{\Delta t} \propto \frac{1}{\Delta z} = \mathcal{O}(J) \ ,$$

the overall computational effort is of the order $\mathcal{O}(J^2)$ and hence in very good agreement with the simulation results.

In a last step we analyze the benefit of a finer spatial resolution. Based on the free pore volumes in Table 9.1, we calculate the relative deviation between the free pore volumes for J = 100 and J = 400 according to

$$s_{V_{free}} = \frac{\left|V_{free}(J = 400) - V_{free}(J = 100)\right|}{V_{free}(J = 400)} \ .$$

The relative deviation is about $s_{V_{free}}$ = 0.21 % for the explicit as well as for the implicit method. Taking into account the enlarged computational effort with decreasing spatial resolution (even for the implicit method we observe a quadratic increase in runtime), an increase in the number of discretization points for a continuous model is of no benefit for the here-required accuracy.

Discrete model To model the catalytically-induced growth of Li_2O_2 on selected sites along the pore surface, the decrease of free pore volume in equation (9.1) is modified by a catalytic function according to equation (9.6). The effect of the catalytic function is to switch on ($cat_j^n = 1$) or off ($cat_j^n = 0$) the Li_2O_2 growth at position j in the pore at a given time n. Smooth growth of discharge product is realized via a threshold, as illustrated in Section 9.1.

Here, we first study eight different thresholds 1 - 7 % and 10 % in a pore with a single catalyst placed at the center of the cathode length. This is done in order to *(i)* study the different growth mechanisms (island vs layer-by-layer growth) with respect to the chosen threshold parameter and *(ii)* optimize this parameter for the discrete catalyst model.

Figure 9.8 (b) shows the growth resulting from the applied model using $DMSO^{Li^+}$ and a threshold of 6 %. Initially the discharge product grows solely at the catalytic site. Once the threshold is reached, growth starts also at the neighboring sites (schematically shown in Figure 9.8 (a) with decreasing brightness). Since oxygen enters the pore from the left, oxygen concentration and deposition rate are higher on the left than on the right side of the initial catalytic site. Consequently, the threshold is reached earlier at the pore entrance side and facilitates the spread of new growth centers towards this direction, leading to an asymmetric growth profile.

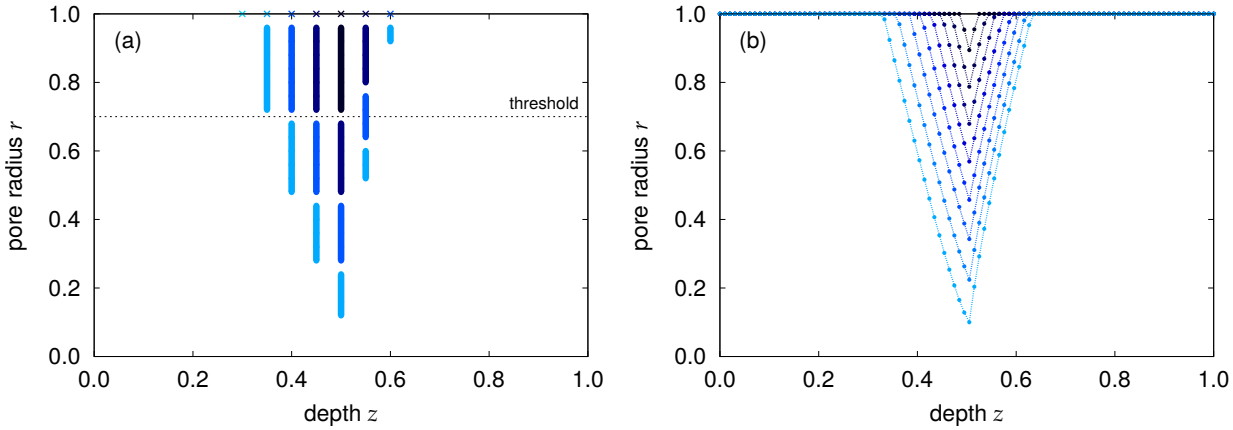

Figure 9.8.: Growth profiles of Li_2O_2 in the presence of a single catalyst at the pore center. (a) Scheme of the employed propagation strategy for the catalytic function towards neighbor sites. (b) Simulation results until pore clogging with a threshold of 6 % in $DMSO^{Li^+}$. The time evolution of the profiles is represented with colors ranging from dark to light blue.

Figure 9.9 shows the growth profiles obtained after pore clogging using a single catalyst and different thresholds. The applied thresholds lead to different rates of growth along the pore axis which correspond to different growth mechanisms, from an island formation for large thresholds (Volmer-Weber growth) to a layer-by-layer growth for small thresholds (Frank-van-der-Merwe growth). However, the choice of the threshold value is constrained by the stability criteria. In particular, since pore radius and concentration at every time step and discretization point are dependent on the chosen threshold, time step and spatial resolution have to be adjusted according to its value. The validity of the stability criteria is thus a severe constraint on the type of growth that can be considered in the present model. The morphology of lithium peroxide deposition observed

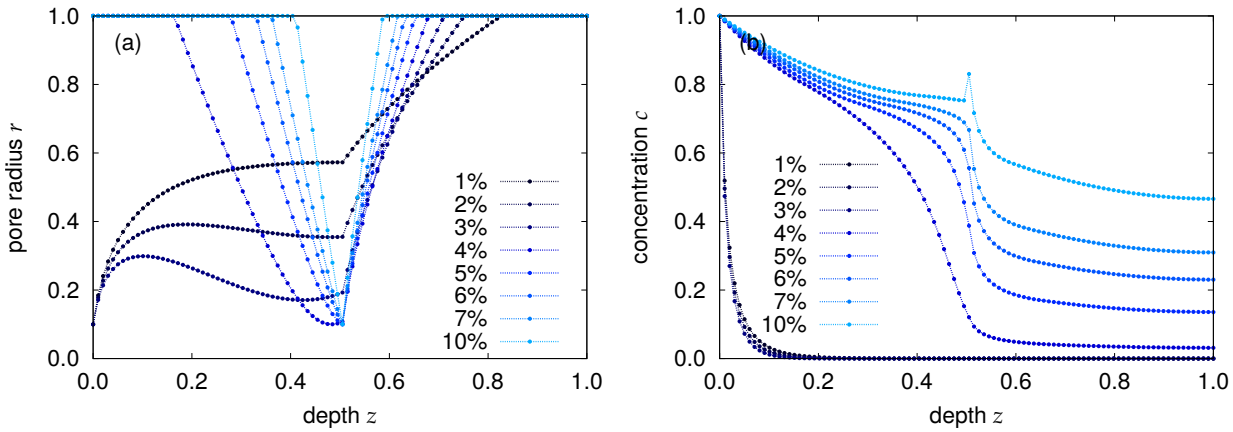

Figure 9.9.: (a) Growth profiles of Li_2O_2 and (b) oxygen concentration after pore clogging in the presence of a single catalyst at the pore center for different thresholds and in $DMSO^{Li^+}$.

experimentally on cathode surfaces is mainly governed by the applied current density. While at low current densities of a few μA cm^{-2} the formation of toroidal-shaped lithium peroxide particles takes place,[17,137,138] uniform thin film growth has been reported by Adams et al.[16] at current densities larger than 50 μA cm^{-2}. In the present work we use a current density of 100 μA cm^{-2}, which corresponds to a thin film growth. High threshold values are thus not representative of the real deposition mechanisms. However, to allow for a certain degree of discrete growth, very low values are also not appropriate, and the following simulations will be restricted to a threshold range of 4 - 6 % of the initial pore radius.

The results of the iterative minimization procedure in the Greedy algorithm for the case of the DMSO$^{Li^+}$ electrolyte and a threshold of 6 % are shown exemplary in Figure 9.10 (a) for the implicit and (b) for the explicit method. The space discretization is set to J = 100 possible catalyst

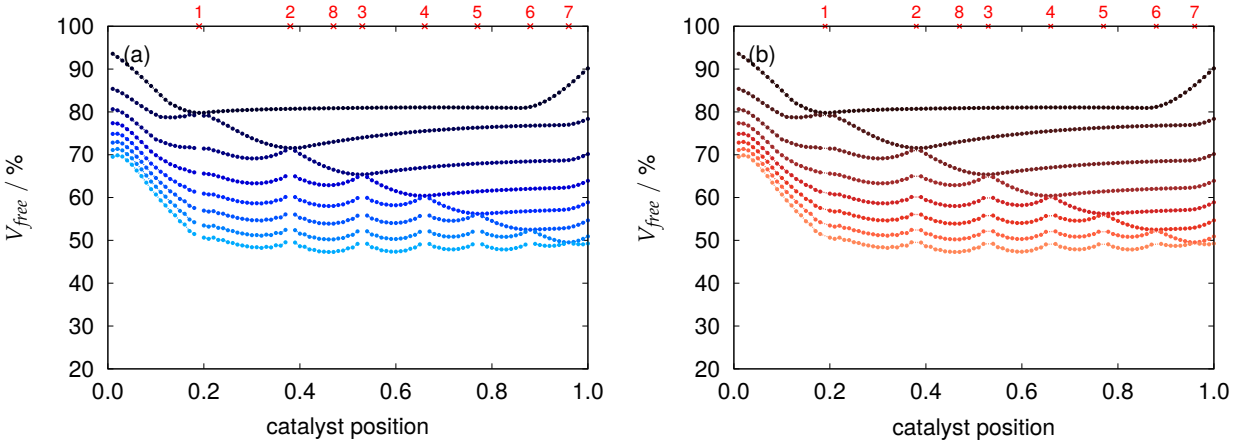

Figure 9.10.: Free pore volume with respect to the catalyst position during the first eight steps of the Greedy algorithm for (a) the implicit (blue) and (b) the explicit (red) method in DMSO$^{Li^+}$ for a threshold of 6 %. The positions of minimum free volume determined after each step are labeled with corresponding red numbers.

positions along the pore length. The figure represents the calculated free pore volume V_{free} after pore clogging for every catalyst position screened in each of the first eight Greedy steps. The positions of the successively individuated minima of V_{free} are marked with red numbers indicating the corresponding Greedy step, i. e., the order in which the catalysts are placed. Discrete growth and concentration profiles resulting from the implicit and the explicit calculation differ only slightly. The deviation between both methods has no influence on the optimization procedure. Catalyst positions as well as the order of placement are identical for the implicit and the explicit method. Furthermore, we note that the progressive placement of catalysts does not proceed from the end of the pore towards the pore entrance, as one may have intuitively expected.

In summary, we choose the implicit finite difference method for further analysis of pore clogging in different electrolytes, since this method provides the significantly shorter runtime with simultaneously a negligible relative deviation of the free pore volume between the two methods. Furthermore, the number of discretization points is set to $J = 100$, since no considerable advantage arises from an increase of J in the continuous model. In the case of a discrete growth we assume $J = 100$ possible catalyst positions as appropriate to determine a catalyst distribution along the pore and to state differences between the five solvent environments.

CHAPTER 10

RESULTS

In the following chapter we present the results of the pore clogging analysis carried out in five different electrolytes. The issue of pore clogging is studied first in a continuous growth model for a one-sided and a two-sided oxygen supply into the pore. Subsequently, the discrete growth model based on the Greedy algorithm is applied on the one-sided pore, and the optimal catalyst number and positioning are determined using the free pore volume as an objective function. Finally, three additional pore geometries are studied in the continuous and in the discrete growth model and discussed with regard to the standard cylindric pore.

10.1. Continuous growth

Assuming every discretization point along the pore axis as a site for Li_2O_2 deposition, the discrete mathematical model presented in the previous chapter is solved for a one-sided and a two-sided pore and for all five electrolytes PC^{Li^+}, $TEGDME^{Li^+}$, $DMSO^{Li^+}$ and DME^{Li^+} until clogging of the pore. To ensure stability, the time step is adjusted in order to keep the concentration in a reasonable range of $c \in [0, 1]$. Figures 10.1 (a) and (c) show the final growth profiles as a function of cathode depth for a one-sided and a two-sided pore respectively and Figures 10.1 (b) and (d) their corresponding concentrations. The resulting free pore volumes V_{free} and the corresponding times until pore clogging are listed in Table 10.1. V_{free} varies between 30 % for DME^{Li^+} to 92 % for PC^{Li^+} for the one-sided and between 17 % for DME^{Li^+} to 84 % for PC^{Li^+} for the two-sided pore, depending on the combination of oxygen diffusivity and solubility.

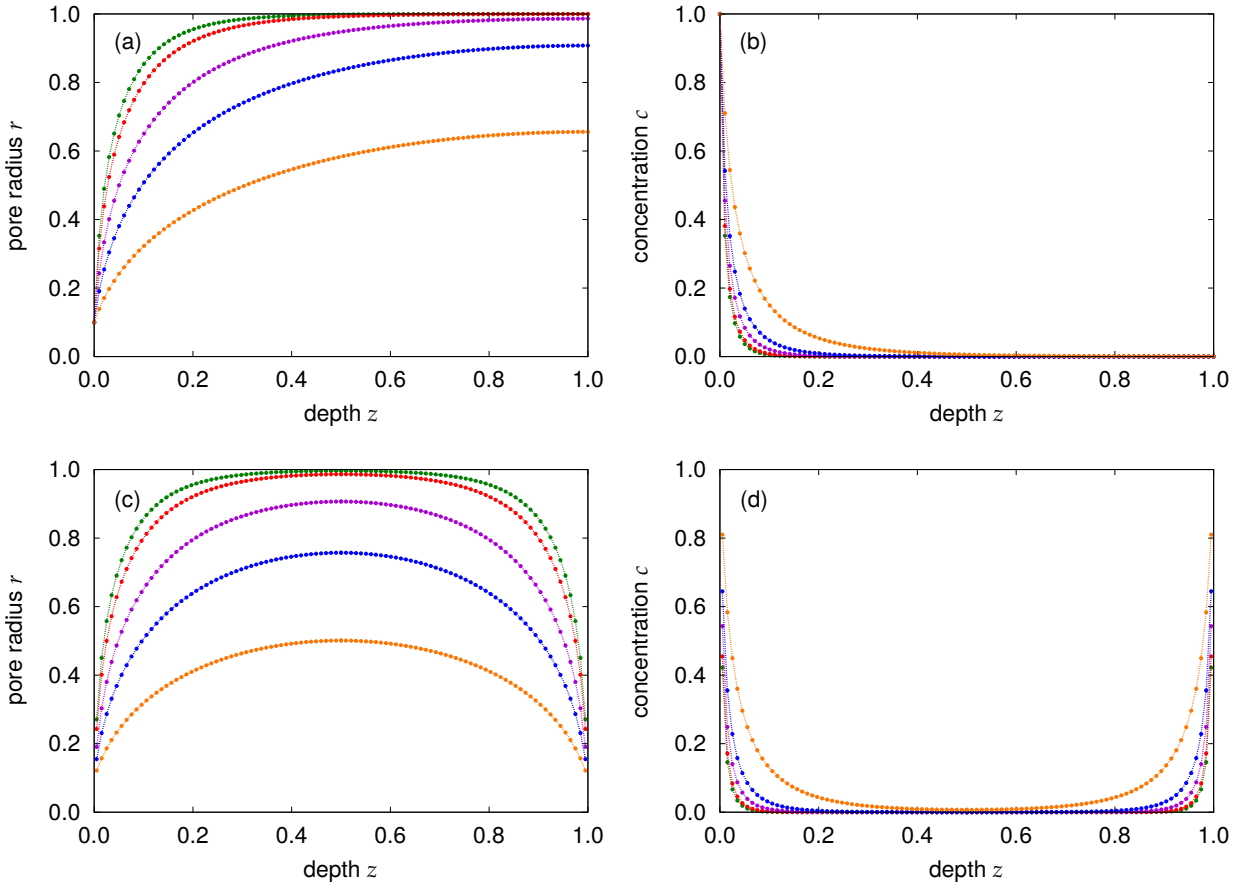

Figure 10.1.: Continuous growth profiles of Li_2O_2 after pore clogging for the electrolytes PC^{Li^+} (green), $TEGDME^{Li^+}$ (red), SL (purple), $DMSO^{Li^+}$ (blue) and DME^{Li^+} (orange) for (a) a one-sided and (c) a two-sided pore with corresponding concentrations in (b) and (d). Oxygen molecules enter the pore from the left side in the case of the one-sided pore.

Table 10.1.: Free pore volume and time until pore clogging for a one- and two-sided open pore.

	V_{free} / %		t_p / h	
	one-sided	two-sided	one-sided	two-sided
PC^{Li^+}	92.02	84.44	83	321
$TEGDME^{Li^+}$	89.44	79.32	109	426
SL	79.29	61.44	213	802
$DMSO^{Li^+}$	61.62	40.84	399	1271
DME^{Li^+}	30.13	17.33	771	1914

Due to the poor mass diffusivity and the small oxygen solubility in PC^{Li^+} and $TEGDME^{Li^+}$, the free pore volumes after pore clogging remain at 80 % and above the initial value for the one-sided as well as for the two-sided pore. Despite the high mass diffusivity of $DMSO^{Li^+}$, the lowest free pore volumes and the longest times until pore clogging are achieved for DME^{Li^+}. At this point the about four times higher oxygen solubility combined with a good mass diffusivity is dominating the delay of pore clogging. For all electrolytes, two-sided pores show a decrease in free pore volume between 7.51 % and 21 % and about 2.5 to 4 longer times until pore clogging. The highest decrease in free pore volume from one-sided to two-sides pores is achieved for $DMSO^{Li^+}$ and can be explained by the high oxygen mass diffusivity. Nonetheless, mass diffusivity and solubility have to be considered together to obtain a good utilization of the cathode volume.

10.2. Optimal number and distribution of catalysts

In this section we aim to estimate the optimal number and distribution of catalysts that lead to the minimum free pore volume after clogging, i. e., to maximal utilization of the cathode capacity. The optimization is carried out using a Greedy algorithm with the free volume V_{free} of a single pore after clogging as the objective function. The algorithm is based on an iterative search scheme in which at each iteration step a new single catalyst is placed in the pore, and its position is optimized, while the previously set catalysts remain fixed at their already optimized positions. Namely, at each iteration step a new single catalyst is placed at every position j not yet occupied by previously set catalysts, and the deposition of Li_2O_2 is carried out as described in the previous chapter until pore clogging. The position that leads to the minimum free pore volume is then chosen and fixed, before adding a new catalyst and repeating the procedure until no further decrease of free pore volume occurs with increasing number of new catalysts. This algorithm is implemented in parallel, assigning to each computing core several positions j within the same iteration step, as illustrated in Chapter 9.

The evolution of the minimum free volume obtained in every Greedy step is shown in Figure 10.2 (a) for the example of the electrolyte $DMSO^{Li^+}$ and a threshold of 6 %. The minimum free volume decreases rapidly in the first steps and then more slowly until the optimal value is reached, in this case after placement of 43 catalysts. Increasing the number of catalysts after this point results in an increase of the free volume which eventually converges to the value obtained with the continuous growth mechanism, proving the consistency of the method. The number of catalysts corresponding to the maximum pore filling (43) as well as to 90 % and 99 % of the optimal filling are highlighted in red. The actual distribution of catalysts along the pore axis corresponding to

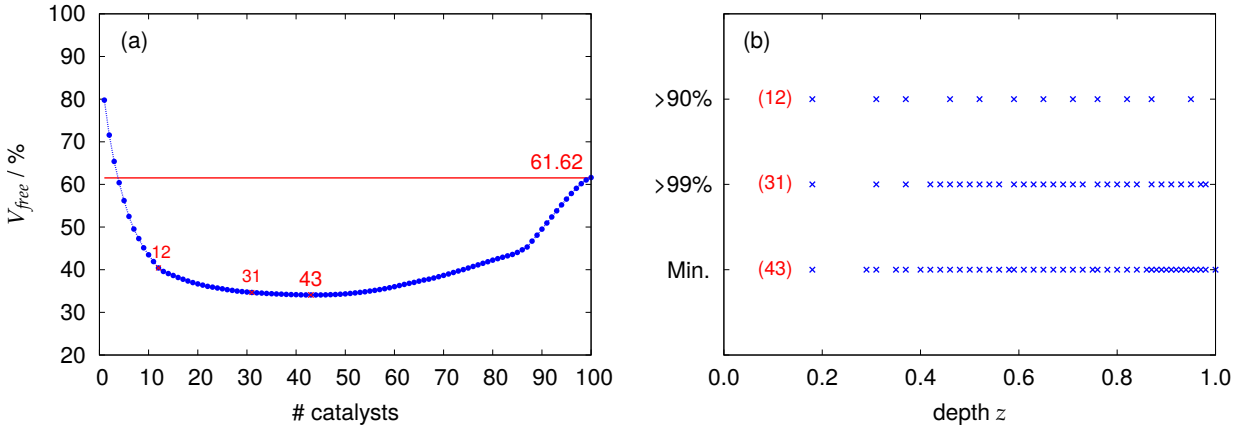

Figure 10.2.: (a) Evolution of the minimum free volume after pore clogging as a function of the number of placed catalysts along the pore axis in $DMSO^{Li^+}$ for a threshold of 6 %. The red line indicates the minimum free volume obtained with the continuous growth model. The numbers of catalysts corresponding to 90 %, 99 %, and 100 % of the final occupied volume are marked in red. (b) Optimal distributions of catalysts along the pore axis corresponding to the three different cases marked in (a).

these three filling volumes are reported in Figure 10.2 (b). According to expectation, the closed side of the pore is occupied more densely with catalysts, while no catalysts are placed close to the pore entrance. A similar behavior can be observed for the three different thresholds considered as well as for the five electrolytes and is summarized in Figure 10.3 (a). Figure 10.3 (b) shows the profiles of the discharge product deposition for the optimal distributions of catalysts corresponding to the five electrolytes for the exemplary threshold of 6 %.

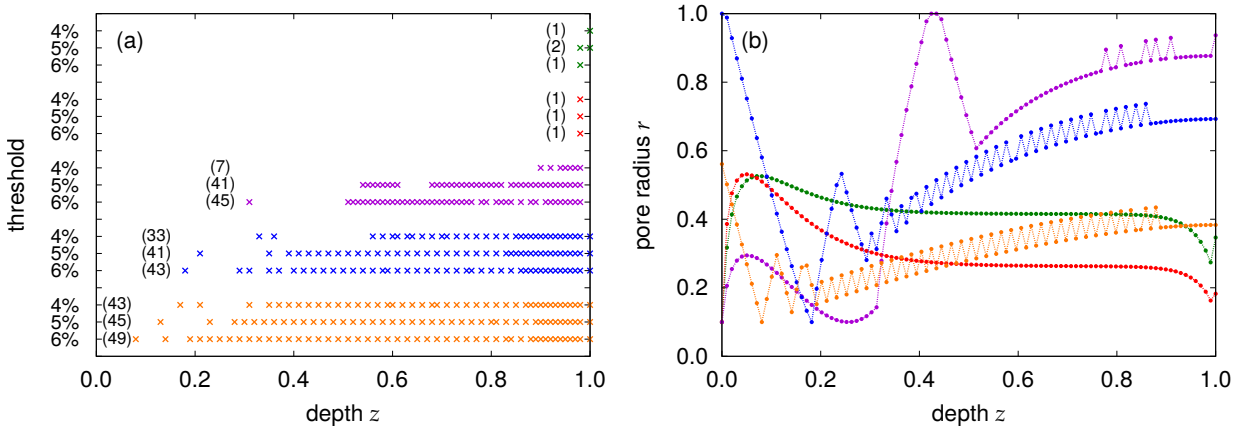

Figure 10.3.: (a) Optimal distributions of catalysts along the pore axis for thresholds of 4, 5, and 6 % for the electrolytes PC^{Li^+} (green), $TEGDME^{Li^+}$ (red), SL (purple), $DMSO^{Li^+}$ (blue) and DME^{Li^+} (orange). The numbers of placed catalysts are shown in parenthesis in each case. (b) Growth profiles of Li_2O_2 after pore clogging for all electrolytes and a threshold of 6 %.

The final minimum free volumes after pore clogging for all electrolytes and thresholds are listed in Table 10.2 in comparison with the values relative to a continuous growth.

Table 10.2.: Free pore volume for the continuous model and for the discrete catalyst model for thresholds of 4, 5, and 6 %.

	V_{free} / %			
	cont.	4 %	5 %	6 %
PC^{Li^+}	92.02	18.36	25.21	33.82
$TEGDME^{Li^+}$	89.44	9.63	23.17	23.17
SL	79.29	5.70	21.58	44.07
$DMSO^{Li^+}$	61.62	34.08	33.20	24.61
DME^{Li^+}	30.13	10.36	12.75	14.81

In a last step we apply both the continuous growth model and the discrete Greedy optimization algorithm on three additional pore geometries, a bullet-shaped, a funnel-shaped, and a reverse funnel-shaped pore. The initial pore entrance radius is chosen to be equal for all geometries. The Li_2O_2 profiles resulting from continuous growth in the three cases are shown in Figure 10.4 (a)-(c). The final optimal number and positioning of catalysts in the discrete model are shown in Figure 10.4 (d). The corresponding free volumes after pore clogging for the continuous model and for the discrete model for all four considered geometries are summarized in Table 10.3.

Table 10.3.: Free pore volume for the continuous model and for the discrete catalyst model for all four pore geometries cylindric, bullet-shaped, funnel-shaped, and reverse funnel-shaped for a threshold of 6 %.

	V_{free} / % (continuous)				V_{free} / % (discrete)			
	cylindric	bullet	funnel	rev. funnel	cylindric	bullet	funnel	rev. funnel
PC^{Li^+}	92.02	88.44	84.26	93.47	18.36	62.44	83.81	58.19
$TEGDME^{Li^+}$	89.44	84.82	80.25	91.26	9.63	55.11	79.83	62.37
SL	79.29	73.62	69.30	83.57	44.07	35.91	67.47	58.81
$DMSO^{Li^+}$	61.62	54.30	52.48	67.51	34.08	18.26	50.75	24.55
DME^{Li^+}	30.13	20.60	19.98	35.98	10.36	11.49	20.86	12.85

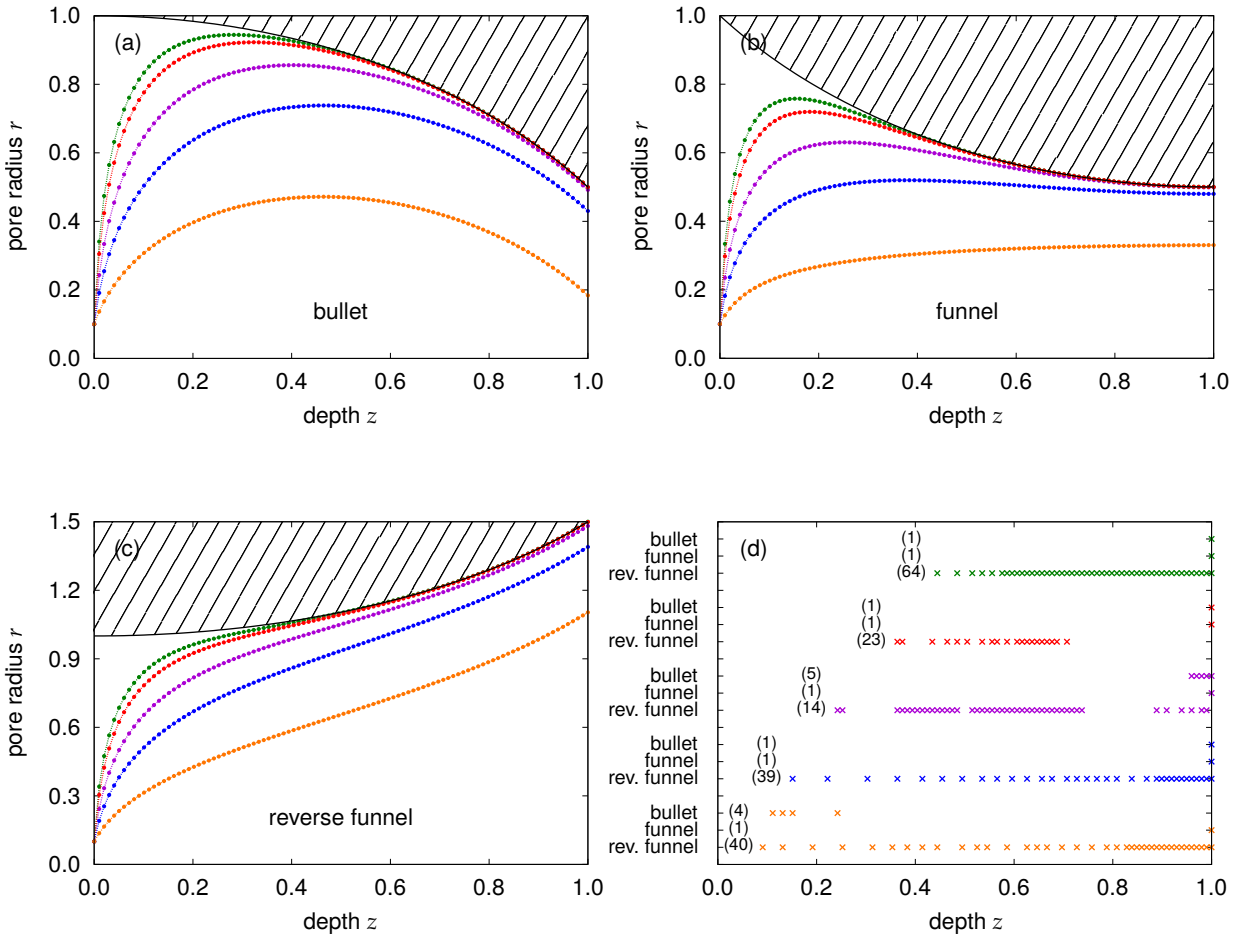

Figure 10.4.: Continuous growth profiles of Li_2O_2 after pore clogging for (a) a bullet-shaped, (b) a funnel-shaped and (c) a reverse funnel-shaped pore and (d) optimal distributions of catalysts along the pore axis for a threshold of 6 %, for all four pore geometries and for the electrolytes PC^{Li^+} (green), $TEGDME^{Li^+}$ (red), SL (purple), $DMSO^{Li^+}$ (blue) and DME^{Li^+} (orange).

In the continuous growth model the reverse funnel-shaped pore provides the worst performance due to the unsuitable widening of the pore towards the closed side. However, a discrete optimized positioning of catalysts results in a significant improvement of the relative pore volume utilization, in particular for the favored electrolytes $DMSO^{Li^+}$ and DME^{Li^+}. It should be noted that the absolute pore volume and hence the amount of deposited Li_2O_2 is larger compared to the standard cylindric pore. Some of the optimal distributions of catalysts are comparable to the distributions obtained from a cylindric pore, i. e., a dense catalyst occupation at the closed side and less dense towards the pore entrance. However, for the $TEGDME^{Li^+}$ electrolyte the distribution is far from intuitive and is clustered in the central region of the pore. The bullet-shaped pore also shows an improvement in the pore volume utilization for an optimized discrete positioning of catalysts using only a few

catalysts. Although the improvement is comparable to a cylindric and a reverse funnel-shaped pore for the electrolytes $DMSO^{Li^+}$ and DME^{Li^+}, the benefit is lower taken into account the decreased absolute volume of the bullet shape. In the case of a funnel-shaped pore a discrete catalyst distribution has virtually no effect on the utilization of the pore volume due to the strong tapering of the pore. The algorithm stops after setting only one catalyst at the far pore end, resulting in pore volume utilizations very similar to the continuous case.

CHAPTER 11

DISCUSSION

Many approaches have been proposed to overcome the oxygen starvation of the cathode in Li/air batteries which strongly limits their capacity. Several experimental[37,109] and theoretical[116,127,139] studies have shown that the specific capacity increases with decreasing current density due to transport limitations of oxygen into the cathode. However, a high current density is desired to increase the battery performance and decrease the charging time. This has motivated in-depth studies into the optimization of the oxygen transport properties which are influenced by the cathode thickness and porosity as well as by the oxygen solubility and diffusivity in the electrolyte.[114,140] For example, Li et al.[127] has shown in a theoretical study that a linear increase of the porosity towards the oxygen supplying side preserves oxygen transport tunnels and simultaneously increases the discharge capacity. The search for suitable electrolytes with high oxygen solubility and diffusivity has been rather difficult because of limitations set by the required high electrochemical stability and system safety.[1] Therefore, as mentioned in the introduction, recent effort has been devoted to optimize the activity and distribution of catalytic centers at the cathode surface with the aim of maximizing the volume occupied by the discharge products before passivation or pore clogging takes place.[115,116]

In this part we have presented an efficient numerical solution of the reaction-diffusion equation governing the deposition of Li_2O_2 in porous cathodes during the battery discharge process on the basis of a previously suggested model.[44] We have then implemented a Greedy optimization algorithm that has allowed us to determine the optimal number and position of catalysts within the cathode pores for a given electrolyte characterized by its oxygen solubility $c_{O_2,0}$ and diffusivity D_{O_2}. Particular attention has been paid to ensure numerical stability of the employed algorithms by accurate determination of the discrete time step Δt and spatial resolution Δz (equations (9.8)

and (9.9)).

In our current implementation, the nucleation of Li_2O_2 at a specific position is defined by a binary function that either allows or prevents its deposition. The lateral growth of the so-formed nucleus is then modeled by a simple propagation procedure of the catalytic function towards neighbor sites based on an arbitrary deposition threshold. However, we note that the implementation of more complex nucleation and growth mechanisms, such as the definition of position-dependent fractional reaction probabilities or time-dependent growth kinetics, is readily possible and shall be investigated in future, possibly more realistic studies. Also the extension of the algorithm to three-dimensional porosity models is in principle possible, although associated with a greatly increased computational effort, especially if optimization of catalyst distributions are sought for.

However, even in its current implementation, the outcome of our simulations allows us to compare the performance of different electrolytes. Considering homogeneous Li_2O_2 deposition at the whole pore surface, about 90 % of the initial pore volume remains free after pore clogging for the case of PC^{Li^+} and $TEGDME^{Li^+}$, mostly due to their poor mass diffusivity and small oxygen solubility (see Table 10.2). Instead, the high diffusivity and high oxygen solubility of DME^{Li^+} lead to a much better pore utilization with a remaining free volume of about 30 %. It is important to note that efficient utilization of the cathode volume requires not only a high diffusivity, but also, concomitantly, a high solubility of molecular oxygen. Indeed, despite its high mass diffusivity, $DMSO^{Li^+}$ is considerably less efficient than DME^{Li^+} because of its lower oxygen solubility.

In the presence of catalysts the dominant factor determining a maximal pore utilization becomes the distribution of the individual catalyst positions. Namely, the distributions obtained with the help of our Greedy optimization algorithm results in similar final free volumes after pore clogging for all five electrolytes (see Figure 10.3 and Table 10.2), although with very different number and positions of catalysts.

A visual comparison of the specific capacities per mass of carbon averaged over the three thresholds correspondent to the five electrolytes is shown in Figure 11.1. The calculation is based on the volume of discharge product after pore clogging and an initial cathode porosity of $\epsilon_0 = 73\,\%$:

$$c_{spec} = \frac{2F\rho_{Li_2O_2}\epsilon_0(1 - V_{free})}{M_{Li_2O_2}\rho_C(1 - \epsilon_0)} \,. \tag{11.1}$$

All electrolytes show a high improvement in discharge capacity moving from a continuous growth (limited by the intrinsic electrolyte properties) to a catalyzed, discrete growth (limited by the positioning of the catalysts). The improvement is particularly evident for PC^{Li^+} and $TEGDME^{Li^+}$, whose initially poor performances can be compensated by a small number of catalysts placed far from the oxygen entrance side. Because of the low oxygen diffusivities in these two cases, the

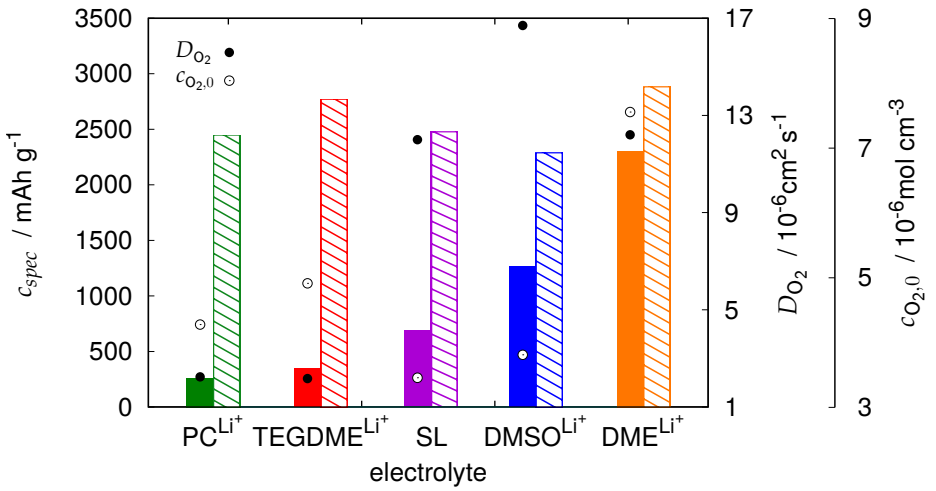

Figure 11.1.: Specific capacities per mass of carbon (ρ_C = 2.3 g cm^{-3} [94]) for a continuous growth (solid) and a discrete catalyst growth averaged over thresholds of 4, 5, and 6 % (striped) after pore clogging in the five considered electrolytes. The correspondent oxygen solubilities and diffusivities are shown with empty and filled circle symbols, respectively.

lateral spread of the initially formed nuclei is faster than their vertical growth, since the incoming oxygen molecules are consumed by the ORR before reaching the far end of the pore. Overall, the highest specific capacity is still presented by DME$^{Li^+}$ which is indeed among the most widely used electrolytes along with DMSO$^{Li^+}$ whose advantage is the electrochemical stability especially towards species being formed during the discharge.

CHAPTER 12

CONCLUSION AND PERSPECTIVE

The realization of an established and commercially available Li/air battery is facing many challenges and is still at the beginning of research. Although no long-term stability with a high energy per mass ratio has yet been accomplished, the Li/air battery remains nonetheless of a matchless attractiveness due to its theoretical expectations regarding the specific energy, in particular for electric vehicles. The issues in enabling an operating full-battery-cell design are addressed to the protection of the metallic Li anode via a Solid Electrolyte Interface and the percolation of oxygen from ambient air with no simultaneous evaporation of the electrolyte via a selective membrane which also provides the mechanical flexibility to deal with the occurring large volume changes in the battery cycle.

However, the precondition for this is a working cathode half-cell, in which the main chemical processes take place. To establish a truly reversible chemistry, the identification of the actual reaction mechanisms of the charge and discharge process is essential, considering the enormous impact of the morphology of the electrochemically grown Li_2O_2 on the discharge potential and particularly on the charge process and the charge potential. Furthermore, without knowledge of the processes and their intermediate species only a few suggestions can be done concerning the stability of all participating agents (most of all the electrolyte, but also the separator and the cathode itself). Thus, we have dedicated the first part of the present thesis to the charge process in Li/air batteries. By means of an unbiased technique as first principles molecular dynamics based on density functional theory without requirements of empirical data and approximative models, we have gained insight into electronic structures and chemical reaction pathways and the involved intermediates, comparable to experimental in situ measurements. The proposed two-stage process for the decomposition of amorphous Li_nO_n clusters based on our simulation results contributes to

the clarification of possible reaction pathways in the decomposition of Li_2O_2 which deposits on the cathode surface as amorphous thin film at large current densities.[16] Particular attention has been paid to a realistic environment (within the capability of DFT-based simulations) to study the impact of a solvent on the reaction pathway. In doing so, we have shown that a possible reaction mechanism in the charge process is first a peroxide-to-superoxide transition of the amorphous clusters at low potentials followed by a release of O_2 (with or without Li^+) at higher potentials, while Li^+ detachment from the cluster occurred only as a compound structure with O_2, and no preceding delithiation process could be observed in our simulations. However, the recently proposed and currently discussed delithiation during the charge process is usually referred to crystalline bulk Li_2O_2, which represents the main part of the toroidal Li_2O_2 particles grown at low current densities.[11–15] A next step that we would propose regarding the investigation of the charge process in Li/air batteries is hence the decomposition of crystalline Li_2O_2 in the presence of a solvent to study a possible delithiation process and its specific reaction pathway. By this means, we could establish an overall image of the charge process and the decomposition of Li_2O_2 with its complex structure composed of crystalline, amorphous, and superoxide-like species.

However, this is only one direction of the (ideally) reversible process in Li/air batteries. The analysis of the discharge process with particular attention paid to nucleation, crystal growth and morphology is inevitable, but could go beyond the scope of DFT-based simulations. Furthermore, the oxidation of molecular dioxygen on the carbon matrix is not a simple task from a computational point of view due to the delocalization of the electrons. An alternative for the analysis of crystal growth is provided by the reactive force field (ReaxFF) method which allows large system sizes as well as longer simulation times in terms of the reaction coordinate.[141] However, this method should be treated with caution while modeling an unknown crystal growth mechanism. Apart from molecular dynamics simulations, another approach to dissolution and growth of Li_2O_2 discharge product could be represented by Monte Carlo simulations, in particular kinetic Monte Carlo, which, however, have to be parametrized, for example, by means of DFT-based simulations, to obtain the kinetic parameters.[142,143] Finally, the passivation of the cathode surface should not be disregarded. Based on the results on morphology and growth mechanisms, which could be obtained from the above simulations, the effect of dopants, vacancies, surface conduction, impact of crystallographic directions, and layer thickness could be studied.[21,144] A potentially suitable technique for the analysis of band structures and electron transport is offered by the DFTB$^+$ (Density Functional based Tight Binding) code based on a Green's function formalism.[145]

Concomitant with simulations, an experimental study of discharge product morphologies and composition is necessary and planed at the Fraunhofer IFAM* to identify the factors determining the discharge process, such as current density, electrolyte and cathode materials, and in so doing to figure out dependencies on the resulting morphologies of discharge product. This has to be followed subsequently be a similar analysis on charge to define dependencies on the reaction pathway(s) also on the reverse process between external factors and the actual discharge product. Schwager et al.[146] developed at the Carl von Ossietzky University in Oldenburg in cooperation with the Fraunhofer IFAM* an in-situ detection of dioxygen permeation through a gas diffusion electrode (GDE) in Li^+-based organic electrolyte via a positionable microelectrode. Thereby, the authors detected also soluble ORR products, which they assigned to superoxide species. Although this method presents a powerful tool to distinguish between soluble and insoluble discharge product species, in particular in a Li^+ environment, on time and size scales considered in chemical reactions, exact predictions of reaction products and pathways as well as their intermediates in the charge/discharge cycle are only possible by combining both experimental expertise and DFT-based or beyond DFT simulations.

Once a reversible chemistry is established, the next challenge is the maximization of the battery capacity. Apart from the mentioned passivation effect, the deposition and yield of discharge product is critical to achieve a maximum cathode utilization and capacity, since pore clogging and poor oxygen transport restrict a full cathode volume access significantly. In this study we have presented a first step in controlling the discharge product deposition via an optimized discrete catalyst distribution. By this means, we have improved the battery capacity and achieved a comparable performance for electrolytes with initially widely varying capacities. Nonetheless, the model has been kept simple to examine the possibilities of heuristic optimization applied on diffusion-based growth models. A next step in the analysis and control of discharge product deposition should address the combination of optimization methods with more sophisticated models describing transport phenomena. These have been already established in the modeling of Li-ion batteries based on Newman models[45,46] and transfered to Li/air batteries.[44,115,116] In this way, we can take into account the electrolyte phase and the corresponding lithium ion concentration, electrostatic potential effects as well as the impact of resistivity of grown discharge product.[115,116] Furthermore, it would be interesting to study the effect of partial wettability in comparison to fully flooded cathodes as well as the impact of active cathode surface, pore radius, and in particular pore geometry.[107] The study of an appropriate pore geometry, however, should be carried out in higher-dimensional models than the, so far, broadly used one-dimensional pores

*Fraunhofer Institute for Manufacturing Technology and Advanced Materials, Project Group for Electrical Energy Storage, Oldenburg, Germany

to prevent the violation of the assumptions of angular symmetry and constant concentration in the radial direction. On the basis of these two or three dimensional models including the above enhancements, the initially basic model can be extended to a pore network to mimic a macroscopic cathode structure which contains macroscopic oxygen transport tunnels as well as meso- and micropores.Thus, an advanced cathode model could be established to understand the complex processes taking place during discharge of the Li/air battery and provide the opportunity to support an electrode design of maximum capacity gain. However, as already implied in the motivation of this thesis, a macroscopic model has to be provided with empirical and experimental data and/or results from atomistic simulations. Since the experimental analysis of morphology and growth mechanisms of the discharge product Li_2O_2 in the porous structure is a challenging issue, growth mechanisms gathered from atomistic simulations could help to derive a more realistic discharge product propagation scheme in a catalyst induced growth than the one that has been used in the present thesis. Furthermore, classical molecular dynamics can be applied to determine required dynamical constants, such as diffusion constants, or to support the understanding of complex formation of lithium ions and electrolyte salt anions even in a more realistic setup of potential-driven dynamics.

On the experimental side of cathode investigation first steps toward catalysis as well as analysis of pore clogging in different GDE structures have already been taken. An intensive study on the catalytic activity of manganese oxides, which have a considerable advantage in cost over the broadly used noble metals, has been performed by Augustin et al.[43,147] at the Fraunhofer IFAM*. In Cyclic Voltammetry measurements in a LiTFSI/DMSO electrolyte the authors observed a significant increase in peak potential during the ORR and hence a decreased overall overpotential for α-Mn_2O_3, indicating a strong catalytic activity of the molecule. This is ascribed to an alternative reaction pathway of the rate-determining one-electron reduction of oxygen during the discharge process, which is now taking place at the catalyst particle surface, such that the discharge process is primary limited by the oxygen diffusion toward the cathod surface. Electocatalytic activity as well as a modification of the cathode surface with catalyst particles have been shown in the above studies. However, since we aim not only to enhance the electrochemical reaction during discharge but also to benefit from this quality by controlling the discharge product deposition, in a next step based on the already established and available infrastructure a mechanism has to be developed to control the catalyst distribution along the cathode. Moreover, the advantage of catalytic active sides can be utilized only for an appropriate choice of the porous carbon cathode. Bardenhagen et al.[112] investigated at the University of Bremen in cooperation with the Fraunhofer IFAM* different GDE designs containing macro- and mesopores in a LiTFSI/DMSO electrolyte.

By in situ Electrochemical Impedance Spectroscopy in a three electrode setup the authors could separate the different transport and electrochemical processes at the anode and the cathode in terms of time and space, identifying pore clogging as one of the main limiting factors in the discharge of Li/air batteries. Furthermore, in macroporous materials (Freudenberg GDE) a planar-surface-like behavior has been observed, and the ORR are limited by passivation of the cathode surface due to a thin Li_2O_2 film growth. On the other hand, mesoporous cathodes (xerogel GDE) have demonstrated the highest specific capacity among the investigated GDEs and a long and constant oxygen reduction due to a high storage capability and a large specific surface area but, however, suffer from pore clogging. In a further study,[148] the same group analyzed the distribution and composition of discharge products along the cathode as a function of pore size by X-ray Photoelectron Spectroscopy. This study revealed that marcroporous cathodes provide a homogeneous discharge product deposition, while mesoporous cathodes show a high amount of discharge product at the interfaces and a concentration drop toward the inner parts. This is due to the large oxygen transport tunnels in a macroporous structure and an impeded diffusion of Li^+ and O_2 in mesopores. For the same reason discharge product composition varies widely in mesoporous structures. At the electrolyte facing side deposition of the desired Li_2O_2 discharge product can be observed until a lack of replenishment of both components occurs, while at the oxygen supplying side Li_2CO_3 represents the main part of the solid discharge product due to a decreased lithium ion concentration. In the central region of the cathode both Li^+ and O_2 concentrations are low, such that less discharge product is observed.

These findings, namely time and space resolution of the processes during discharge and discharge product distribution along the cathode as a function of two different sizes of pores, provide the opportunity to modify influencing and limiting factors in the present model in a more realistic manner and to verify the new settings within a LiTFSI/DMSO test system for two different GDEs. On this basis a geometry optimization can be proceeded to identify the optimal porous network for a maximized cathode capacity without a costly experimental setup. In a last step both experimental studies from Augustin et al. and Bardenhagen et al. can be combined, using an optimal catalyst positioning obtained from simulations. Preliminary, applying catalytically active sides on the porous cathode, the mechanism of catalysis and the concomitant growth mechanism have to be adopted by the model, such that more reliable predictions about the performance of different electrolytes can be done. In summary, in future work the wide range of simulation methods on different time and size scales as well as experimental studies have to be combined to achieve a broad understanding of the promising Li/air battery and hence to establish a long-term working, reversible and efficient alternative to present energy storage concepts.

Bibliography

[1] J. Christensen, P. Albertus, R. S. Sanchez-Carrera, T. Lohmann, B. Kozinsky, R. Liedtke, J. Ahmed, A. Kojic, A Critical Review of Li/Air Batteries, Journal of the Electrochemical Society 159 (2012) R1–R30. doi:10.1149/2.086202jes.

[2] P. G. Bruce, S. A. Freunberger, L. J. Hardwick, J.-M. Tarascon, Li-O_2 and Li-S Batteries with High Energy Storage, Nature Materials 11 (1) (2012) 19–29. doi:10.1038/nmat3191.

[3] P. Hartmann, C. L. Bender, M. Vračar, A. K. Dürr, A. Garsuch, J. Janek, P. Adelhelm, A Rechargeable Room-Temperature Sodium Superoxide (NaO_2) Battery, Nature Materials 12 (2013) 228–232. doi:10.1038/nmat3486.

[4] T. Zhang, N. Imanishi, Y. Takeda, O. Yamamoto, Aqueous Lithium/Air Rechargeable Batteries, Chemistry Letters 40 (7) (2011) 668–673. doi:10.1246/cl.2011.668.

[5] E. Peled, The Electrochemical Behavior of Alkali and Alkaline Earth Metals in Nonaqueous Battery Systems - The Solid Electrolyte Interphase Model, Journal of the Electrochemical Society 126 (1979) 2047–2051. doi:10.1149/1.2128859.

[6] D. Aurbach, Review of Selected Electrode-Solution Interactions Which Determine the Performance of Li and Li Ion Batteries, Journal of Power Sources 89 (2) (2000) 206–218. doi:http://dx.doi.org/10.1016/S0378-7753(00)00431-6.

[7] C. O. Laoire, S. Mukerjee, K. M. Abraham, E. J. Plichta, M. A. Hendrickson, Influence of Nonaqueous Solvents on the Electrochemistry of Oxygen in the Rechargeable Lithium-Air Battery, The Journal of Physical Chemistry C 114 (19) (2010) 9178–9186. doi:10.1021/jp102019y.

[8] C. O. Laoire, S. Mukerjee, K. M. Abraham, E. J. Plichta, M. A. Hendrickson, Elucidating the Mechanism of Oxygen Reduction for Lithium-Air Battery Applications, The Journal of Physical Chemistry C 113 (46) (2009) 20127–20134. doi:10.1021/jp908090s.

[9] Z. Peng, S. A. Freunberger, L. J. Hardwick, Y. Chen, V. Giordani, F. Bardé, P. Novák, D. Graham, J.-M. Tarascon, P. G. Bruce, Oxygen Reactions in a Non-Aqueous Li^+ Electrolyte, Angewandte Chemie International Edition 50 (28) (2011) 6351–6355. doi:10.1002/anie.201100879.

[10] V. Viswanathan, K. S. Thygesen, J. S. Hummelshøj, J. K. Nørskov, G. Girishkumar, B. D. McCloskey, A. C. Luntz, Electrical Conductivity in Li_2O_2 and Its Role in Determining Capacity Limitations in Non-Aqueous Li-O_2 Batteries, The Journal of Chemical Physics 135 (21). doi:10.1063/1.3663385.

[11] B. M. Gallant, D. G. Kwabi, R. R. Mitchell, J. Zhou, C. V. Thompson, Y. Shao-Horn, Influence of Li_2O_2 Morphology on Oxygen Reduction and Evolution Kinetics in Li-O_2 Batteries, Energy & Environmental Science 6 (2013) 2518–2528. doi:10.1039/C3EE40998H.

[12] S. Ganapathy, B. D. Adams, G. Stenou, M. S. Anastasaki, K. Goubitz, X.-F. Miao, L. F. Nazar, M. Wagemaker, Nature of Li_2O_2 Oxidation in a Li-O_2 Battery Revealed by Operando X-Ray Diffraction, Journal of the American Chemical Society 136 (46) (2014) 16335–16344. doi:10.1021/ja508794r.

[13] C. Xia, M. Waletzko, L. Chen, K. Peppler, P. J. Klar, J. Janek, Evolution of Li_2O_2 Growth and Its Effect on Kinetics of Li-O_2 Batteries, ACS Applied Materials & Interfaces 6 (15) (2014) 12083–12092. doi:10.1021/am5010943.

[14] X.-h. Yang, P. He, Y.-y. Xia, Preparation of Mesocellular Carbon Foam and Its Application for Lithium/oxygen Battery, Electrochemistry Communications 11 (6) (2009) 1127–1130. doi:10.1016/j.elecom.2009.03.029.

[15] R. Black, J.-H. Lee, B. Adams, C. A. Mims, L. F. Nazar, The Role of Catalysts and Peroxide Oxidation in Lithium-Oxygen Batteries, Angewandte Chemie International Edition 52 (1) (2013) 392–396. doi:10.1002/anie.201205354.

[16] B. D. Adams, C. Radtke, R. Black, M. L. Trudeau, K. Zaghib, L. F. Nazar, Current Density Dependence of Peroxide Formation in the Li-O_2 Battery and Its Effect on Charge, Energy & Environmental Science 6 (2013) 1772–1778. doi:10.1039/C3EE40697K.

[17] R. R. Mitchell, B. M. Gallant, C. V. Thompson, Y. Shao-Horn, All-Carbon-Nanofiber Electrodes for High-energy Rechargeable Li-O_2 Batteries, Energy & Environmental Science 4 (2011) 2952–2958. doi:10.1039/C1EE01496J.

[18] J. S. Hummelshøj, J. Blomqvist, S. Datta, T. Vegge, J. Rossmeisl, K. S. Thygesen, A. C. Luntz, K. W. Jacobsen, J. K. Nørskov, Communications: Elementary Oxygen Electrode Reactions in the Aprotic Li-Air Battery, The Journal of Chemical Physics 132 (7). doi:10.1063/1.3298994.

[19] P. Albertus, G. Girishkumar, B. McCloskey, R. S. Sánchez-Carrera, B. Kozinsky, J. Christensen, A. C. Luntz, Identifying Capacity Limitations in the Li/Oxygen Battery using Experiments and Modeling, Journal of the Electrochemical Society 158 (2011) A343–A351. doi:10.1149/1.3527055.

[20] S. Meini, M. Piana, H. Beyer, J. Schwämmlein, H. A. Gasteiger, Effect of Carbon Surface Area on First Discharge Capacity of Li-O_2 Cathodes and Cycle-Life Behavior in Ether-Based Electrolytes, Journal of the Electrochemical Society 159 (2012) A2135–A2142. doi:10.1149/2.011301jes.

[21] M. D. Radin, J. F. Rodriguez, F. Tian, D. J. Siegel, Lithium Peroxide Surfaces are Metallic, while Lithium Oxide Surfaces are not, Journal of the American Chemical Society 134 (2) (2012) 1093–1103. doi:10.1021/ja208944x.

[22] B. D. McCloskey, R. Scheffler, A. Speidel, G. Girishkumar, A. C. Luntz, On the Mechanism of Nonaqueous Li-O_2 Electrochemistry on C and Its Kinetic Overpotentials: Some Implications for Li-Air Batteries, The Journal of Physical Chemistry C 116 (45) (2012) 23897–23905. doi:10.1021/jp306680f.

[23] F. Mizuno, S. Nakanishi, Y. Kotani, S. Yokoishi, H. Iba, Rechargeable Li-Air Batteries with Carbonate-Based Liquid Electrolytes, Electrochemistry 78 (5) (2010) 403–405. doi:10.5796/electrochemistry.78.403.

[24] W. Xu, K. Xu, V. V. Viswanathan, S. A. Towne, J. S. Hardy, J. Xiao, Z. Nie, D. Hu, D. Wang, J.-G. Zhang, Reaction Mechanisms for the Limited Reversibility of Li-O_2 Chemistry in Organic Carbonate Electrolytes, Journal of Power Sources 196 (22) (2011) 9631–9639. doi:10.1016/j.jpowsour.2011.06.099.

[25] S. A. Freunberger, Y. Chen, Z. Peng, J. M. Griffin, L. J. Hardwick, F. Bardé, P. Novák, P. G. Bruce, Reactions in the Rechargeable Lithium-O_2 Battery with Alkyl Carbonate Electrolytes, Journal of the American Chemical Society 133 (20) (2011) 8040–8047. doi:10.1021/ja2021747.

[26] J. Xiao, J. Hu, D. Wang, D. Hu, G. L. Xu, Wu Graff, Z. Nie, J. Liu, J.-G. Zhang, Investigation of the Rechargeability of Li-O_2 Batteries in Non-Aqueous Electrolyte, Journal of Power Sources 196 (13) (2011) 5674–5678. doi:10.1016/j.jpowsour.2011.02.060.

[27] G. M. Veith, N. J. Dudney, J. Howe, J. Nanda, Spectroscopic Characterization of Solid Discharge Products in Li-Air Cells with Aprotic Carbonate Electrolytes, The Journal of Physical Chemistry C 115 (29) (2011) 14325–14333. doi:10.1021/jp2043015.

[28] B. D. McCloskey, D. S. Bethune, R. M. Shelby, G. Girishkumar, A. C. Luntz, Solvents' Critical Role in Nonaqueous Lithium-Oxygen Battery Electrochemistry, The Journal of Physical Chemistry Letters 2 (10) (2011) 1161–1166. doi:10.1021/jz200352v.

[29] S. A. Freunberger, Y. Chen, N. E. Drewett, L. J. Hardwick, F. Bardé, P. G. Bruce, The Lithium-Oxygen Battery with Ether-Based Electrolytes, Angewandte Chemie International Edition 50 (37) (2011) 8609–8613. doi:10.1002/anie.201102357.

[30] F. S. Gittleson, R. C. Sekol, G. Doubek, M. Linardi, A. D. Taylor, Catalyst and Electrolyte Synergy in Li-O_2 Batteries, Physical Chemistry Chemical Physics 16 (2014) 3230–3237. doi:10.1039/C3CP54555E.

[31] M. M. Ottakam Thotiyl, S. A. Freunberger, Z. Peng, Y. Chen, Z. Liu, P. G. Bruce, A Stable Cathode for the Aprotic Li-O_2 Battery, Nature Materials 12 (2013) 1050–1056. doi:10.1038/nmat3737.

[32] M. J. Trahan, S. Mukerjee, E. J. Plichta, M. A. Hendrickson, K. M. Abrahama, Studies of Li-Air Cells Utilizing Dimethyl Sulfoxide-Based Electrolyte, Journal of the Electrochemical Society 160 (2013) A259–A267. doi:10.1149/2.048302jes.

[33] Z. Peng, S. A. Freunberger, Y. Chen, P. G. Bruce, A Reversible and Higher-Rate Li-O_2 Battery, Science 337 (6094) (2012) 563–566. doi:10.1126/science.1223985.

[34] D. G. Kwabi, T. P. Batcho, C. V. Amanchukwu, N. Ortiz-Vitoriano, P. Hammond, C. V. Thompson, Y. Shao-Horn, Chemical Instability of Dimethyl Sulfoxide in Lithium-Air Batteries, The Journal of Physical Chemistry Letters 5 (16) (2014) 2850–2856. doi:10.1021/jz5013824.

[35] C. Tran, X.-Q. Yang, D. Qu, Investigation of the Gas-Diffusion-Electrode used as Lithium/air Cathode in Non-Aqueous Electrolyte and the Importance of Carbon Material Porosity, Journal

of Power Sources 195 (7) (2010) 2057–2063. doi:10.1016/j.jpowsour.2009.10.012.

[36] G. Q. Zhang, J. P. Zheng, R. Liang, C. Zhang, B. Wang, M. Au, M. Hendrickson, E. J. Plichta, α-MnO_2/Carbon Nanotube/Carbon Nanofiber Composite Catalytic Air Electrodes for Rechargeable Lithium-Air Batteries, Journal of the Electrochemical Society 158 (2011) A822–A827. doi:10.1149/1.3590736.

[37] D. Zhang, Z. Fu, Z. Wei, T. Huang, A. Yu, Polarization of Oxygen Electrode in Rechargeable Lithium Oxygen Batteries, Journal of the Electrochemical Society 157 (2010) A362–A365. doi:10.1149/1.3298450.

[38] A. Débart, J. Bao, G. Armstrong, P. G. Bruce, An O_2 Cathode for Rechargeable Lithium Batteries: the Effect of a Catalyst, Journal of Power Sources 174 (2) (2007) 1177–1182, 13th International Meeting on Lithium Batteries. doi:10.1016/j.jpowsour.2007.06.180.

[39] H. Cheng, K. Scott, Selection of Oxygen Reduction Catalysts for Rechargeable Lithium-Air Batteries - Metal Or Oxide?, Applied Catalysis B: Environmental 108-109 (0) (2011) 140–151. doi:10.1016/j.apcatb.2011.08.021.

[40] A. K. Thapa, T. Ishihara, Mesoporous α-MnO_2/Pd Catalyst Air Electrode for Rechargeable Lithium-Air Battery, Journal of Power Sources 196 (16) (2011) 7016–7020, 15th International Meeting on Lithium Batteries (IMLB). doi:10.1016/j.jpowsour.2010.09.112.

[41] Y.-C. Lu, H. A. Gasteiger, M. C. Parent, V. Chiloyan, Y. Shao-Horn, The Influence of Catalysts on Discharge and Charge Voltages of Rechargeable Li-Oxygen Batteries, Electrochemical and Solid-State Letters 13 (2010) A69–A72. doi:10.1149/1.3363047.

[42] Y.-C. Lu, H. A. Gasteiger, E. Crumlin, R. McGuire Jr., Y. Shao-Horn, Electrocatalytic Activity Studies of Select Metal Surfaces and Implications in Li-Air Batteries, Journal of the Electrochemical Society 157 (2010) A1016–A1025. doi:10.1149/1.3462981.

[43] M. Augustin, O. Yezerska, D. Fenske, I. Bardenhagen, A. Westphal, M. Knipper, T. Plaggenborg, J. Kolny-Olesiak, J. Parisi, Mechanistic Study on the Activity of Manganese Oxide Catalysts for Oxygen Reduction Reaction in an Aprotic Electrolyte, Electrochimica Acta 158 (2015) 383–389. doi:10.1016/j.electacta.2015.01.163.

[44] S. S. Sandhu, J. P. Fellner, G. W. Brutchen, Diffusion-Limited Model for a Lithium/Air Battery with an Organic Electrolyte, Journal of Power Sources 164 (1) (2007) 365–371. doi:10.1016/j.jpowsour.2006.09.099.

[45] M. Doyle, J. Newman, The Use of Mathematical Modeling in the Design of Lithium/Polymer Battery Systems, Electrochimica Acta 40 (13–14) (1995) 2191–2196, international Symposium on Polymer Electrolytes. doi:10.1016/0013-4686(95)00162-8.

[46] T. Fuller, M. Doyle, J. Newman, Simulation and Optimization of the Dual Lithium Ion Insertion Cell, Journal of The Electrochemical Society 141 (1994) 1–10. doi:10.1149/1.2054684.

[47] T. Dabrowski, L. Colombi Ciacchi, Atomistic modeling of the charge process in lithium/air batteries, The Journal of Physical Chemistry Cdoi:10.1021/acs.jpcc.5b09002.

[48] T. Dabrowski, A. Struck, D. Fenske, P. Maaß, L. Colombi Ciacchi, Optimization of Catalytically Active Sites Positioning in Porous Cathodes of Lithium/Air Batteries Filled with Different Electrolytes, ECS Journal of The Electrochemical Societydoi:10.1149/2.0861514jes.

[49] C. O. Laoire, S. Mukerjee, E. J. Plichta, M. A. Hendrickson, K. M. Abraham, Rechargeable Lithium/TEGDME-$LiPF_6$/O_2 Battery, Journal of the Electrochemical Society 158 (2011) A302–A308. doi:10.1149/1.3531981.

[50] S. Kang, Y. Mo, S. P. Ong, G. Ceder, A Facile Mechanism for Recharging Li_2O_2 in Li-O_2 Batteries, Chemistry of Materials 25 (16) (2013) 3328–3336. doi:10.1021/cm401720n.

[51] Y. Mo, S. P. Ong, G. Ceder, First-Principles Study of the Oxygen Evolution Reaction of Lithium Peroxide in the Lithium-Air Battery, Physical Review B 84 (2011) 205446. doi:10.1103/PhysRevB.84.205446.

[52] J. S. Hummelshøj, A. C. Luntz, J. K. Nørskov, Theoretical Evidence for Low Kinetic Overpotentials in Li-O_2 Electrochemistry, The Journal of Chemical Physics 138 (3). doi:10.1063/1.4773242.

[53] Y.-C. Lu, Y. Shao-Horn, Probing the Reaction Kinetics of the Charge Reactions of Nonaqueous Li-O_2 Batteries, The Journal of Physical Chemistry Letters 4 (1) (2013) 93–99. doi:10.1021/jz3018368.

[54] K. C. Lau, L. A. Curtiss, J. Greeley, Density Functional Investigation of the Thermodynamic Stability of Lithium Oxide Bulk Crystalline Structures as a Function of Oxygen Pressure, The Journal of Physical Chemistry C 115 (47) (2011) 23625–23633. doi:10.1021/jp206796h.

[55] J. Read, Ether-Based Electrolytes for the Lithium/Oxygen Organic Electrolyte Battery, Journal of the Electrochemical Society 153 (2006) A96–A100. doi:10.1149/1.2131827.

[56] D. Marx, J. Hutter, Ab Initio Molecular Dynamics: Theory and Implementation, in: Modern Methods and Algorithms of Quantum Chemistry, 1st Edition, NIC Series, John von Neumann Institute for Computing, Jülich, 2000, pp. 301–449.

[57] K. Burke, The ABC of DFT, Department of Chemistry, University of California, Irvine, 2007. URL http://dft.uci.edu/research.php#theabcofdft

[58] W. Koch, M. C. Holthausen, A Chemist's Guide to Density Functional Theory, 2nd Edition, Wiley-VCH, 2000.

[59] M. Born, R. Oppenheimer, Zur Quantentheorie der Molekeln, Annalen der Physik 389 (20) (1927) 457–484. doi:10.1002/andp.19273892002.

[60] R. Car, M. Parrinello, Unified Approach for Molecular Dynamics and Density-Functional Theory, Physical Review Letters 55 (1985) 2471–2474. doi:10.1103/PhysRevLett.55.2471.

[61] J. VandeVondele, A. De Vita, First-Principles Molecular Dynamics of Metallic Systems, Physical Review B 60 (1999) 13241–13244. doi:10.1103/PhysRevB.60.13241.

[62] M. Stengel, A. De Vita, First-Principles Molecular Dynamics of Metals: A Lagrangian Formulation, Physical Review B 62 (2000) 15283–15286. doi:10.1103/PhysRevB.62.15283.

[63] P. Hohenberg, W. Kohn, Inhomogeneous Electron Gas, Physical Review 136 (1964) B864–B871. doi:10.1103/PhysRev.136.B864.

[64] W. Kohn, L. J. Sham, Self-Consistent Equations Including Exchange and Correlation Effects, Physical Review 140 (1965) A1133–A1138. doi:10.1103/PhysRev.140.A1133.

[65] A. Phusittrakool, DFT: Basic Idea and Practical Calculations, accessed: 2015-07-16.
URL http://www.lsr.nectec.or.th/index.php/File:DFT_lecture_abinitworkshop.pdf

[66] Hartree-Fock Method, accessed: 2015-07-16.
URL https://en.wikipedia.org/wiki/Hartree%E2%80%93Fock_method

[67] D. M. Ceperley, B. J. Alder, Ground State of the Electron Gas by a Stochastic Method, Physical Review Letters 45 (1980) 566–569. doi:10.1103/PhysRevLett.45.566.

[68] A. D. Becke, Density-Functional Exchange-Energy Approximation with Correct Asymptotic Behavior, Physical Review A 38 (1988) 3098–3100. doi:10.1103/PhysRevA.38.3098.

[69] J. P. Perdew, K. Burke, M. Ernzerhof, Generalized Gradient Approximation Made Simple, Physical Review Letters 77 (1996) 3865–3868. doi:10.1103/PhysRevLett.77.3865.

[70] J. P. Perdew, Y. Wang, Accurate and Simple Analytic Representation of the Electron-Gas Correlation Energy, Physical Review B 45 (1992) 13244–13249. doi:10.1103/PhysRevB.45.13244.

[71] N. W. Ashcroft, N. D. Mermin, Festkörperphysik, 2nd Edition, Oldenbourg, 2005.

[72] F. D. Murnaghan, The Compressibility of Media under Extreme Pressures, Proceedings of the National Academy of Sciences 30 (9) (1944) 244–247.

[73] W. Quester, Pseudopotential, accessed: 2015-07-16.
URL https://en.wikipedia.org/wiki/Pseudopotential

[74] D. Vanderbilt, Soft Self-Consistent Pseudopotentials in a Generalized Eigenvalue Formalism, Physical Review B 41 (1990) 7892–7895. doi:10.1103/PhysRevB.41.7892.

[75] P. E. Blöchl, Projector Augmented-Wave Method, Physical Review B 50 (1994) 17953–17979. doi:10.1103/PhysRevB.50.17953.

[76] A. De Vita, G. Galli, A. Canning, F. Mauri, F. Gygi, R. Car, Quantum Molecular Dynamics on Massively Parallel Computers, EPFL Supercomputing Review 6.

[77] R. F. W. Bader, Atoms in Molecules: A Quantum Theory, International series of monographs on chemistry, Clarendon Press, 1990.

[78] J. M. G. Cowie, P. M. Toporowski, Association in Binary Liquid System Dimethyl Sulphoxide-Water, Canadian Journal of Chemistry 39 (11) (1961) 2240–2243. doi:10.1139/v61-296.

[79] S. Plimpton, Fast Parallel Algorithms for Short-Range Molecular Dynamics, Journal of Computational Physics 117 (1) (1995) 1–19. doi:10.1006/jcph.1995.1039.

[80] M. L. Strader, S. E. Feller, A Flexible All-Atom Model of Dimethyl Sulfoxide for Molecular Dynamics Simulations, The Journal of Physical Chemistry A 106 (6) (2002) 1074–1080. doi:10.1021/jp013658n.

[81] L. B. Silva, L. C. G. Freitas, Structural and Thermodynamic Properties of Liquid Ethylene Carbonate and Propylene Carbonate by Monte Carlo Simulations, Journal of Molecular Structure: {THEOCHEM} 806 (1–3) (2007) 23–34. doi:10.1016/j.theochem.2006.10.014.

[82] W. Damm, A. Frontera, J. Tirado-Rives, W. L. Jorgensen, OPLS All-Atom Force Field for Carbohydrates, Journal of Computational Chemistry 18 (16) (1997) 1955–1970.
URL http://dx.doi.org/10.1002/(SICI)1096-987X(199712)18:16<1955::AID-JCC1>3.0.CO;2-L

[83] P. S. Charifson, R. G. Hiskey, L. G. Pedersen, Construction and Molecular Modeling of Phospholipid Surfaces, Journal of Computational Chemistry 11 (10) (1990) 1181–1186. doi:10.1002/jcc.540111010.

[84] O. N. Kalugin, A. K. Adya, M. N. Volobuev, Y. V. Kolesnik, Solvation of Solvophilic and Solvophobic Ions in Dimethyl Sulfoxide: Microscopic Structure by Molecular Dynamics Simulations, Physical Chemistry Chemical Physics 5 (2003) 1536–1546. doi:10.1039/B212269C.

[85] J.-P. Bouanich, Site-Site Lennard-Jones Potential Parameters for N_2, O_2, H_2, CO and CO_2, Journal of Quantitative Spectroscopy and Radiative Transfer 47 (4) (1992) 243–250. doi:10.1016/0022-4073(92)90142-Q.

[86] A. Hull, A New Method of X-Ray Crystal Analysis, Physical Review 10 (1917) 661–696. doi:10.1103/PhysRev.10.661.

[87] A. Lazicki, C.-S. Yoo, W. Evans, W. Pickett, Pressure-Induced Antifluorite-To-Anticotunnite Phase Transition in Lithium Oxide, Physical Review B 73 (2006) 672–676. doi:10.1103/PhysRevB.73.184120.

[88] F. A. Shunk, M. Hansen, K. Anderko, I. R. Institute, Constitution of Binary Alloys, 2nd Edition, McGraw-Hill, 1969.

[89] H. Föppl, Die Kristallstrukturen der Alkaliperoxyde, Zeitschrift für Anorganische und Allgemeine Chemie 291 (1–4) (1957) 12–50. doi:10.1002/zaac.19572910104.

[90] L. G. Cota, P. De La Mora, On the Structure of Lithium Peroxide, Li_2Oi_2, Acta Crystallographica Section B 61 (2) (2005) 133–136. doi:10.1107/S0108768105003629.

[91] M. K. Y. Chan, E. L. Shirley, N. K. Karan, M. Balasubramanian, Y. Ren, J. P. Greeley, T. T. Fister, Structure of Lithium Peroxide, The Journal of Physical Chemistry Letters 2 (19) (2011) 2483–2486. doi:10.1021/jz201072b.

[92] S. Hull, T. W. D. Farley, W. Hayes, M. T. Hutchings, The Elastic Properties of Lithium Oxide and Their Variation with Temperature, Journal of Nuclear Materials 160 (2–3) (1988) 125–134. doi:10.1016/0022-3115(88)90039-6.

[93] M. W. J. Chase, N. I. of Standards, Technology, NIST-JANAF Thermochemical Tables, Journal of Physical and Chemical Reference Data Monographs 9.

[94] D. R. Lide, CRC Handbook of Chemistry and Physics, 90th Edition, Taylor & Francis, 2009.

[95] T. Tanifuji, S. Nasu, Heat Capacity and Thermal Decomposition of Lithium Peroxide, Journal of Nuclear Materials 87 (1) (1979) 189–195. doi:10.1016/0022-3115(79)90138-7.

[96] D. T. Sawyer, G. Chiericato, C. T. Angelis, E. J. Nanni, T. Tsuchiya, Effects of Media and Electrode Materials on the Electrochemical Reduction of Dioxygen, Analytical Chemistry 54 (11) (1982) 1720–1724. doi:10.1021/ac00248a014.

[97] T. Laino, A. Curioni, A New Piece in the Puzzle of Lithium/Air Batteries: Computational Study on the Chemical Stability of Propylene Carbonate in the Presence of Lithium Peroxide, Chemistry - A European Journal 18 (12) (2012) 3510–3520. doi:10.1002/chem.201103057.

[98] CP2K, accessed: 2015-06-24.
URL http://www.cp2k.org/

[99] A. Luzar, D. Chandler, Structure and Hydrogen Bond Dynamics of Water-Dimethyl Sulfoxide Mixtures by Computer Simulations, The Journal of Chemical Physics 98 (10) (1993) 8160–8173. doi:10.1063/1.464521.

[100] T. Megyes, I. Bakó, T. Radnai, T. Grósz, T. Kosztolányi, B. Mroz, M. Probst, Structural Investigation of Lithium Iodide in Liquid Dimethyl Sulfoxide: Comparison between Experiment and Computation, Chemical Physics 321 (1–2) (2006) 100–110. doi:10.1016/j.chemphys.2005.08.002.

[101] E. Westphal, J. R. Pliego, Absolute Solvation Free Energy of Li^+ and Na^+ Ions in Dimethyl Sulfoxide Solution: A Theoretical Ab Initio and Cluster-Continuum Model Study, The Journal of Chemical Physics 123 (7). doi:10.1063/1.2001632.

[102] U. Onthong, T. Megyes, I. Bakó, T. Radnai, K. Hermansson, M. Probst, Molecular Dynamics Simulation of Lithium Iodide in Liquid Dimethylsulfoxide, Chemical Physics Letters 401 (1–3) (2005) 217–222. doi:10.1016/j.cplett.2004.11.005.

[103] T. Fujinaga, K. Izutsu, T. Adachi, Polarographic Studies of Dissolved Oxygen in DMSO-Water Mixtures, Bulletin of the Chemical Society of Japan 42 (1) (1969) 140–145. doi:10.1246/bcsj.42.140.

[104] E. Cebe, D. Kaltenmeier, H. G. Hertz, A Study Concerning Self-Association in Mixtures of Cyclohexane, Benzene and DMSO with CCl_4 by the Nuclear Magnetic Relaxation Method, Zeitschrift für Physikalische Chemie 140 (2011) 181–189. doi:10.1524/zpch.1984.140.2.181.

[105] R. Semino, G. Zaldívar, E. J. Calvo, D. Laria, Lithium Solvation in Dimethyl Sulfoxide-Acetonitrile Mixtures, The Journal of Chemical Physics 141 (21). doi:10.1063/1.4902837.

[106] K. C. Lau, R. S. Assary, P. Redfern, J. Greeley, L. A. Curtiss, Electronic Structure of Lithium Peroxide Clusters and Relevance to Lithium-Air Batteries, The Journal of Physical Chemistry C 116 (45) (2012) 23890–23896. doi:10.1021/jp306024f.

[107] I. Bardenhagen, W. Dreher, D. Fenske, A. Wittstock, M. Bäumer, Fluid Distribution and Pore Wettability of Monolithic Carbon Xerogels Measured by 1H {NMR} Relaxation, Carbon 68 (2014) 542–552. doi:10.1016/j.carbon.2013.11.033.

[108] K. M. Abraham, Z. Jiang, A Polymer Electrolyte-Based Rechargeable Lithium/Oxygen Battery, Journal of the Electrochemical Society 143 (1996) 1–5. doi:10.1149/1.1836378.

[109] J. Read, Characterization of the Lithium/Oxygen Organic Electrolyte Battery, Journal of the Electrochemical Society 149 (2002) A1190–A1195. doi:10.1149/1.1498256.

[110] T. Kuboki, T. Okuyama, T. Ohsaki, N. Takami, Lithium-Air Batteries using Hydrophobic Room Temperature Ionic Liquid Electrolyte, Journal of Power Sources 146 (1-2) (2005) 766–769. doi:10.1016/j.jpowsour.2005.03.082.

[111] W. Xu, V. V. Viswanathan, D. Wang, S. A. Towne, J. Xiao, Z. Nie, D. Hu, J.-G. Zhang, Investigation on the Charging Process of Li_2O_2-Based Air Electrodes in Li-O_2 Batteries with Organic Carbonate Electrolytes, Journal of Power Sources 196 (8) (2011) 3894–3899. doi:10.1016/j.jpowsour.2010.12.065.

[112] I. Bardenhagen, O. Yezerska, M. Augustin, D. Fenske, A. Wittstock, M. Bäumer, In Situ Investigation of Pore Clogging during Discharge of a Li/O_2 Battery by Electrochemical Impedance Spectroscopy, Journal of Power Sources 278 (2015) 255–264. doi:10.1016/j.jpowsour.2014.12.076.

[113] C. K. Park, S. B. Park, S. Y. Lee, H. Lee, H. Jang, W. I. Cho, Electrochemical Performances of Lithium-Air Cell with Carbon Materials, Korean Chemical Society 31 (11) (2010) 3221–3224.

[114] J. Read, K. Mutolo, M. Ervin, W. Behl, J. Wolfenstine, A. Driedger, D. Foster, Oxygen Transport Properties of Organic Electrolytes and Performance of Lithium/Oxygen Battery, Journal of the Electrochemical Society 150 (2003) A1351–A1356. doi:10.1149/1.1606454.

[115] R. E. Williford, J.-G. Zhang, Air Electrode Design for Sustained High Power Operation of Li/air Batteries, Journal of Power Sources 194 (2) (2009) 1164–1170. doi:10.1016/j.jpowsour.2009.06.005.

[116] P. Andrei, J. P. Zheng, M. Hendrickson, E. J. Plichta, Some Possible Approaches for Improving the Energy Density of Li-Air Batteries, Journal of the Electrochemical Society 157 (2010) A1287–A1295. doi:10.1149/1.3486114.

[117] C. Großmann, H.-G. Roos, Numerik Partieller Differentialgleichungen, 2nd Edition, Teubner, 1994.

[118] M. Aigner, Discrete Mathematics, 2nd Edition, Series in Discrete Mathematics and Theoretical Computer Science, American Mathematical Society, 2007.

[119] P. Atkins, J. de Paula, Atkins' Physical Chemistry, 9th Edition, OUP Oxford, 2010.

[120] K. A. Connors, Chemical Kinetics: The Study of Reaction Rates in Solution, 1st Edition, VCH, 1990.

[121] W. Demtröder, Experimentalphysik 1, 3rd Edition, Experimentalphysik, Springer, 2002.

[122] S. Arrhenius, Über die Reaktionsgeschwindigkeit bei der Inversion von Rohrzucker durch Säuren, Zeitschrift für Physikalische Chemie 4 (1889) 226–248.

[123] C. E. Mortimer, U. Müller, Chemie: Das Basiswissen der Chemie ; 126 Tabellen, 6th Edition, Georg Thieme, 1996.

[124] D. A. G. Bruggeman, Berechnung Verschiedener Physikalischer Konstanten von Heterogenen Substanzen. I. Dielektrizitätskonstanten und Leitfähigkeiten der Mischkörper aus Isotropen Substanzen, Annalen der Physik 416 (7) (1935) 636–664. doi:10.1002/andp.19354160705.

[125] E. M. LaBolle, J. Quastel, G. E. Fogg, Diffusion Theory for Transport in Porous Media: Transition-Probability Densities of Diffusion Processes corresponding to Advection-Dispersion Equations, Water Resources Research 34 (7) (1998) 1685–1693. doi:10.1029/98WR00319.

[126] E. E. Petersen, Diffusion in a Pore of Varying Cross Section, AIChE Journal 4 (3) (1958) 343–345. doi:10.1002/aic.690040322.

[127] X. Li, A. Faghri, Optimization of the Cathode Structure of Lithium-Air Batteries Based on a Two-Dimensional, Transient, Non-Isothermal Model, Journal of the Electrochemical Society 159 (2012) A1747–A1754. doi:10.1149/2.043210jes.

[128] J. Xiao, D. Wang, W. Xu, R. E. Williford, J. Liu, J.-G. Zhang, Optimization of Air Electrode for Li/Air Batteries, Journal of Electrochemical Society 157 (2010) A487–A492. doi:10.1149/1.3314375.

[129] A. A. Samarskii, The Theory of Difference Schemes, 1st Edition, Monographs and Textbooks in Pure and Applied Mathematics, Taylor & Francis, 2001.

[130] J. W. Thomas, Numerical Partial Differential Equations: Finite Difference Methods, 1st Edition, Vol. 1 of Graduate Texts in Mathematics, Springer Science & Business Media, 1995.

[131] S. Larsson, V. Thomée, M. Krieger-Hauwede, Partielle Differentialgleichungen und Numerische Methoden, 1st Edition, Springer-Lehrbuch Masterclass, 2005.

[132] Finite Difference Method, accessed: 2014-05-05.
URL https://en.wikipedia.org/wiki/Finite_difference_method

[133] P. D. Lax, R. D. Richtmyer, Survey of the Stability of Linear Finite Difference Equations, Communications on Pure and Applied Mathematics 9 (2) (1956) 267–293. doi:10.1002/cpa.3160090206.

[134] OpenMP Architecture Review Board, OpenMP application program interface version 3.0.
URL http://www.openmp.org

[135] L. Nerger, H. Stüben, Workshop: Parallel Programming with MPI and OpenMP (January 2014).

[136] H. R. Schwarz, N. Köckler, Numerische Mathematik, 5th Edition, Teuber, 2004.

[137] R. R. Mitchell, B. M. Gallant, Y. Shao-Horn, C. V. Thompson, Mechanisms of Morphological Evolution of Li_2O_2 Particles during Electrochemical Growth, The Journal of Physical Chemistry Letters 4 (7) (2013) 1060–1064. doi:10.1021/jz4003586.

[138] S. H. Oh, R. Black, E. Pomerantseva, J.-H. Lee, L. F. Nazar, Synthesis of a Metallic Mesoporous Pyrochlore as a Catalyst for Lithium-O_2 Batteries, Nature Chemistry 4 (2012) 1004–1010. doi:10.1038/nchem.1499.

[139] U. Sahapatsombut, H. Cheng, K. Scott, Modelling the Micro-Macro Homogeneous Cycling Behaviour of a Lithium-Air Battery, Journal of Power Sources 227 (0) (2013) 243–253. doi:10.1016/j.jpowsour.2012.11.053.

[140] Y. Wang, S. C. Cho, Analysis of Air Cathode Perfomance for Lithium-Air Batteries, Journal of the Electrochemical Society 160 (2013) A1847–A1855. doi:10.1149/2.092310jes.

[141] A. C. T. van Duin, S. Dasgupta, F. Lorant, W. A. Goddard, ReaxFF: A Reactive Force Field for Hydrocarbons, The Journal of Physical Chemistry A 105 (41) (2001) 9396–9409. doi:10.1021/jp004368u.

[142] A. P. J. Jansen, An Introduction To Monte Carlo Simulations Of Surface Reactions. URL http://arxiv.org/abs/cond-mat/0303028

[143] A. Luttge, R. S. Arvidson, Reactions at Surfaces: A New Approach Integrating Interferometry and Kinetic Simulations, Journal of the American Ceramic Society 93 (11) (2010) 3519–3530. doi:10.1111/j.1551-2916.2010.04141.x.

[144] J. S. G. Myrdal, T. Vegge, Selective Poisoning of Li-Air Batteries for Increased Discharge Capacity, RSC Advances 4 (2014) 15671–15674. doi:10.1039/C3RA47390B.

[145] DFTB$^+$, accessed: 2015-08-07. URL http://www.dftb-plus.info/

[146] P. Schwager, D. Fenske, G. Wittstock, Scanning Electrochemical Microscopy of Oxygen Permeation Through Air-Electrodes in Lithium-Air Batteries, Journal of Electroanalytical Chemistry 740 (2015) 82–87. doi:10.1016/j.jelechem.2014.12.040.

[147] M. Augustin, D. Fenske, I. Bardenhagen, A. Westphal, M. Knipper, T. Plaggenborg, J. Kolny-Olesiak, J. Parisi, Manganese Oxide Phases and Morphologies: A Study on Calcination Temperature and Atmospheric Dependence, Beilstein Journal of Nanotechnology 6 (2015) 47–59. doi:10.3762/bjnano.6.6.

[148] I. Bardenhagen, M. Fenske, D. Fenske, A. Wittstock, M. Bäumer, Distribution of Discharge Products Inside of the Lithium/Oxygen Battery Cathode, Journal of Power Sources 299 (2015) 162–169. doi:10.1016/j.jpowsour.2015.08.089.

[149] O. N. Kalugin, A. K. Adya, M. N. Volobuev, Y. V. Kolesnik, Solvation of Solvophilic and Solvophobic Ions in Dimethyl Sulfoxide: Microscopic Structure by Molecular Dynamics Simulations, Physical Chemistry Chemical Physics 5 (2003) 1536–1546. doi:10.1039/B212269C.

[150] N. Seriani, Ab Initio Thermodynamics of Lithium Oxides: From Bulk Phases to Nanoparticles, Nanotechnology 20 (44) (2009) 445703. doi:10.1088/0957-4484/20/44/445703.

[151] G. Fischer, Lineare Algebra, Grundkurs Mathematik, Vieweg, 2002.

[152] R. J. Valenza, Linear Algebra: An Introduction to Abstract Mathematics, 1st Edition, Undergraduate Texts in Mathematics, Springer New York, 1993.

[153] W. Greiner, J. Reinhardt, Field Quantization, 1st Edition, Springer Berlin Heidelberg, 1996. doi:10.1007/978-3-642-61485-9.

[154] R. Schaback, H. Wendland, Numerische Mathematik, 5th Edition, Springer, 2004.

[155] O. Forster, Analysis 1, 4th Edition, Analysis, Vieweg, 2001.

In der vorliegenden Arbeit sind Ergebnisse enthalten, die im Rahmen der Betreuung folgender studentischer Arbeiten entstanden sind:

Ingmar Bösing, *Quantenmechanische Simulation von Lithiumperoxid-Oberflächen für die Anwendung in Lithium-Luft Batterien*, 2013

The studies of Li_2O_2 surfaces with different terminations and the determination of corresponding surface energies in the Appendix B, Figure B.1 and Table B.1 have been performed by Ingmar Bösing in his outstanding bachelor thesis in April 2013 in the Hybrid Materials Interfaces Group (HMI) at the Faculty of Production Engineering, University of Bremen.

APPENDIX A

PARAMETERS FOR CLASSICAL MOLECULAR DYNAMICS SIMULATIONS

Table A.1.: Simulation parameters for the classical MD simulations (see equation (4.1)) for DMSO,[80] Li^+,[149] and O_2.[85]

atom/ion	ϵ_{ii} / eV	σ_{ii} / Å	q_i / e	m / g mol^{-1}
S	0.015050	3.563595	0.312	32.065
O	0.005160	3.029056	-0.556	15.999
C	0.003354	3.634867	-0.148	12.011
H	0.001032	2.387609	0.090	1.008
Li^+	0.000703	2.073000	1.000	6.941
O (from O_2)	0.004619	2.960000	0.000	15.999
bond	k_b / eV Å^{-2}	b_0 / Å		
S−O	23.220	1.53		
S−C	10.320	1.80		
C−H	13.846	1.11		
O−O (from O_2)	20.000	1.21		
angle	k_θ / eV rad^{-1}	θ_0 / deg		
O−S−C	1.4620	95.00		
C−S−C	3.3970	106.75		
S−C−H	1.9823	111.30		
H−C−H	1.5265	108.40		
dihedral	k_Φ / eV	n		d / deg
O−S−C−H	0.0086	3		0
C−S−C−H	0.0086	3		0

Table A.2.: Simulation parameters for the classical MD simulations for PC with ϵ_{ii}, σ_{ii}, and q_i (see equation (4.1)) from ref. 81. All other parameters are taken from ref. 82 unless otherwise specified. Labels are given in Figure A.1.

atom/ion	ϵ_{ii} / eV	σ_{ii} / Å	q_i / e	m / g mol^{-1}
O	0.009030	2.96	-0.510	15.999
OS1	0.007310	3.00	-0.484	
OS2			-0.442	
C	0.004515	3.75	0.857	12.011
C1	0.002838	3.50	0.166	
C2			0.401	
C3			-0.362	
H1			0.030	
H2	0.000645	2.42	0.002	1.008
H3			0.104	
bond	k_b / eV Å^{-2}	b_0 / Å		
O−C	13.760	1.202[81]		
C−OSn	13.760	1.380		
OS−Cn	13.760	1.410		
Cn−Cm	11.524	1.529		
Cn−Hn	14.620	1.090		
angle	k_θ / eV rad^{-1}	θ_0 / deg		
O−C−OSn	3.56900[83]	123.4[83]		
OSn−C−OSm	3.98180	111.5		
C−OSn−Cn	2.58000	109.5		
OSn−Cn−Cm	2.15000	109.5		
OSn−Cn−Hn	1.50500	109.5		
Cn−Cm−Hn	1.61250	110.7		
C1−C2−C3	2.50905	112.7		
Hn−Cn−Hm	1.41900	107.8		
dihedral	K_1 / eV	K_2 / eV	K_2 / eV	K_4 / eV
C−OSn−Cn−Cm	0.027950	-0.010750	0.028810	0.000000
C−OSn−Cn−Hn	0.000000	0.000000	0.032680	0.000000
OSn−C1−C2−C3	-0.057448	0.000000	0.000000	0.000000
OSn−Cn−Cm−Hn	0.000000	0.000000	0.020124	0.000000
Cn−Cm−Ck−Hn	0.000000	0.000000	0.015738	0.000000
Hn−Cn−Cm−Hm	0.000000	0.000000	0.013674	0.000000

The OPLS dihedral style is based on the potential[79]

$$E = \frac{1}{2}K_1[1+\cos(\phi)] + \frac{1}{2}K_2[1-\cos(2\phi)] + \frac{1}{2}K_3[1+\cos(3\phi)] + \frac{1}{2}K_4[1-\cos(4\phi)] \ .$$

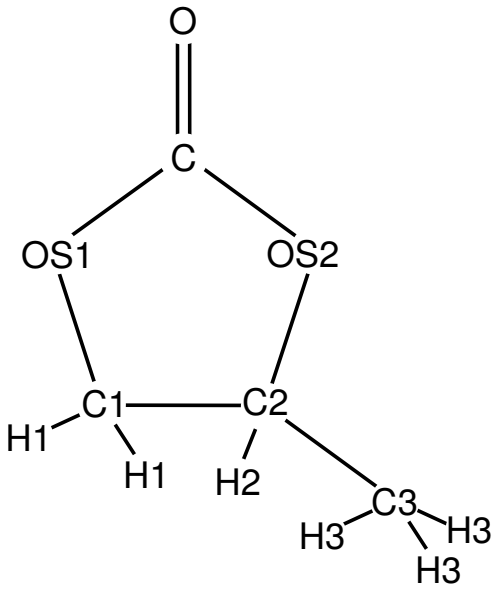

Figure A.1.: PC molecule with corresponding labels.

APPENDIX B

LITHIUM PEROXIDE SURFACES

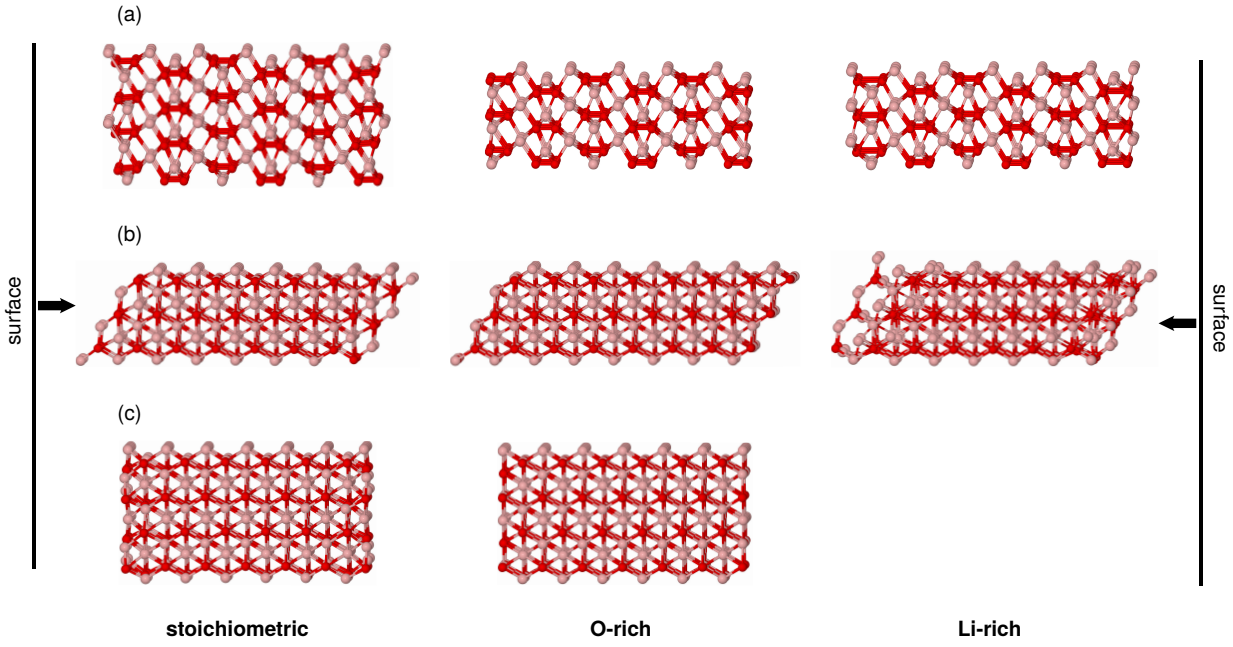

Figure B.1.: (a) (0001), (b) $(10\bar{1}0)$, and (c) $(11\bar{2}0)$ Li_2O_2 surfaces in the three terminations stoichiometric, O-rich, and Li-rich. In the case of a $(11\bar{2}0)$ surface no reasonable Li termination could be found.

Table B.1.: Surface energies in meV Å^{-1} for different Li_2O_2 surfaces and stoichiometries (stoichiometric, O-rich, and Li-rich).

surface	Boesing	Radin et al.[21]	Seriani[150]
(0001) stoi.	55.190	32	41
(0001) O-rich	12.557	6	45
(0001) Li-rich	149.048	—	138
$(10\bar{1}0)$ stoi.	40.157	34	52
$(10\bar{1}0)$ O-rich	23.898	31	43
$(10\bar{1}0)$ Li-rich	117.999	—	105
$(11\bar{2}0)$ stoi.	59.347	52	—
$(11\bar{2}0)$ O-rich	29.174	36	—

APPENDIX C

CLUSTER STRUCTURES AND ENERGIES

Li_2O_2

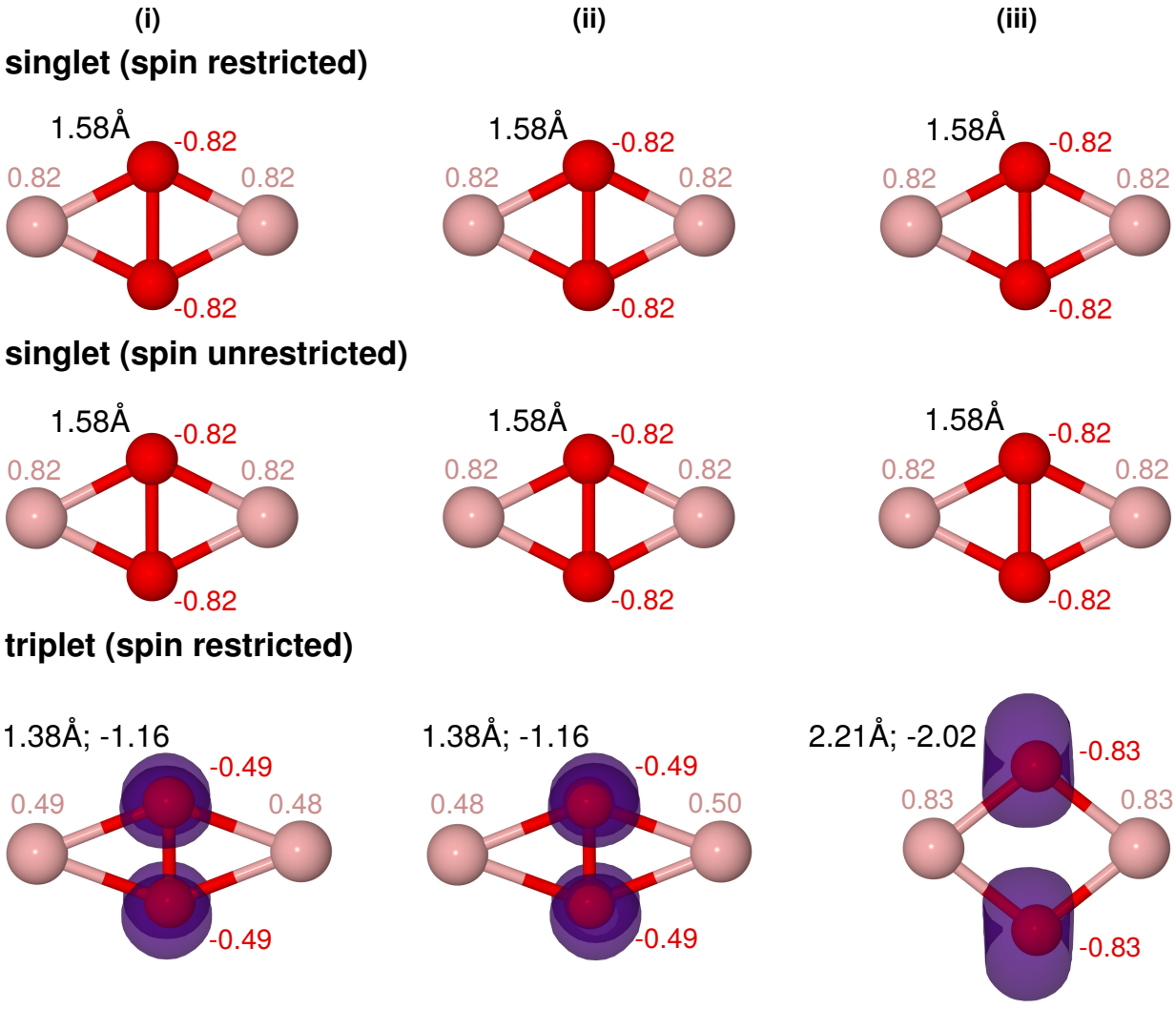

Figure C.1.: Li_2O_2 clusters in a singlet and a triplet state.

Li_4O_4

(i) **(ii)** **(iii)**

singlet (spin restricted)

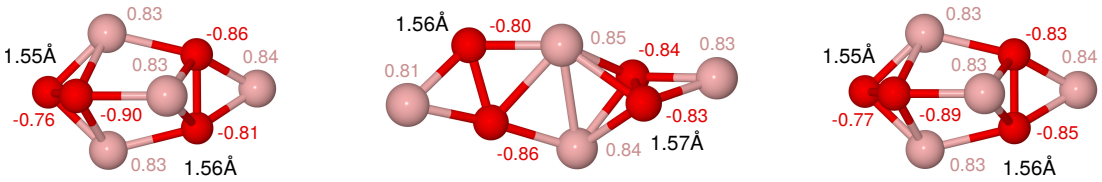

singlet (spin unrestricted)

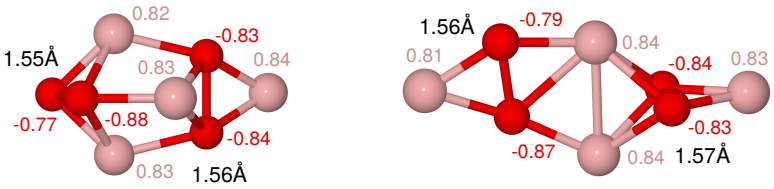

triplet (spin restricted)

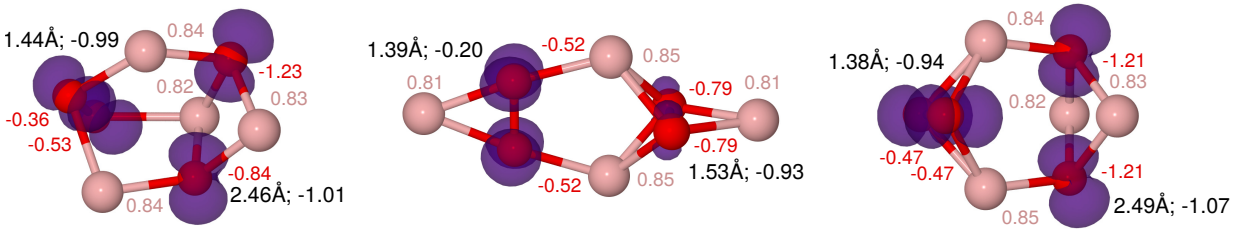

triplet (spin unrestricted)

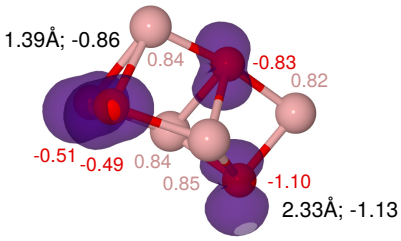

Figure C.2.: Li_4O_4 clusters in a singlet and a triplet state.

Li_6O_6

(i) **(ii)** **(iii)**

singlet (spin restricted)

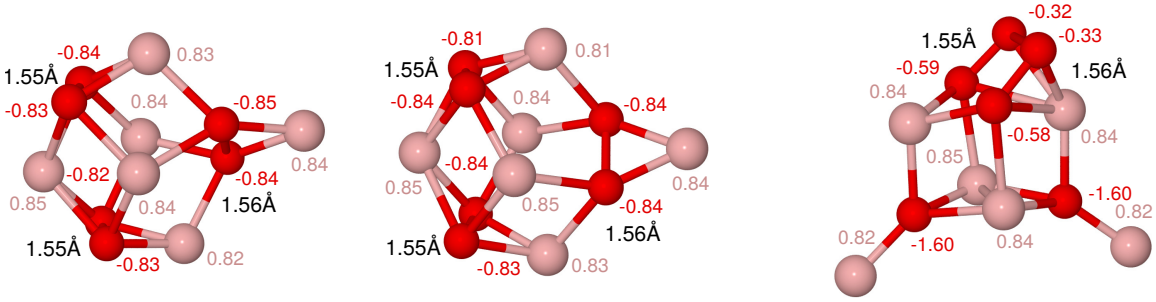

singlet (spin unrestricted)

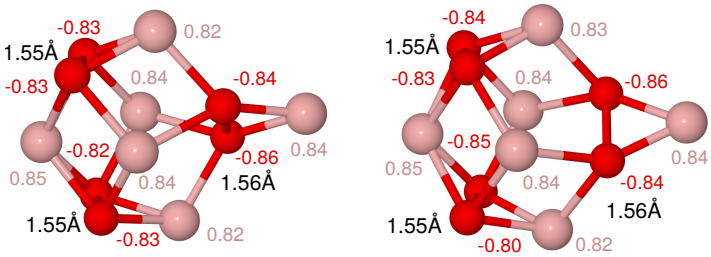

triplet (spin restricted)

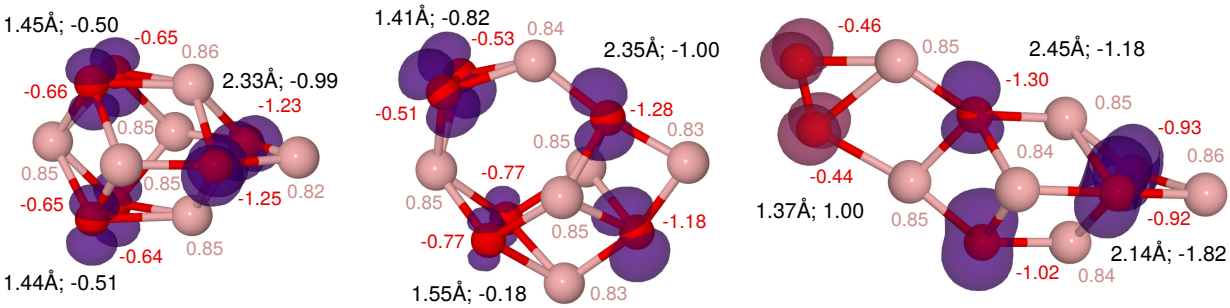

triplet (spin unrestricted)

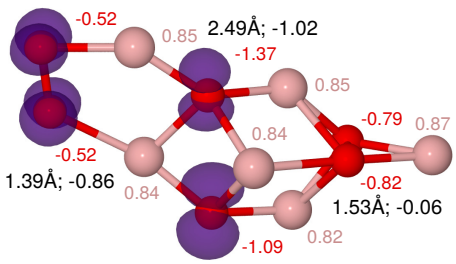

Figure C.3.: Li_6O_6 clusters in a singlet and a triplet state.

Li_8O_8

(i) **(ii)** **(iii)**

singlet (spin restricted)

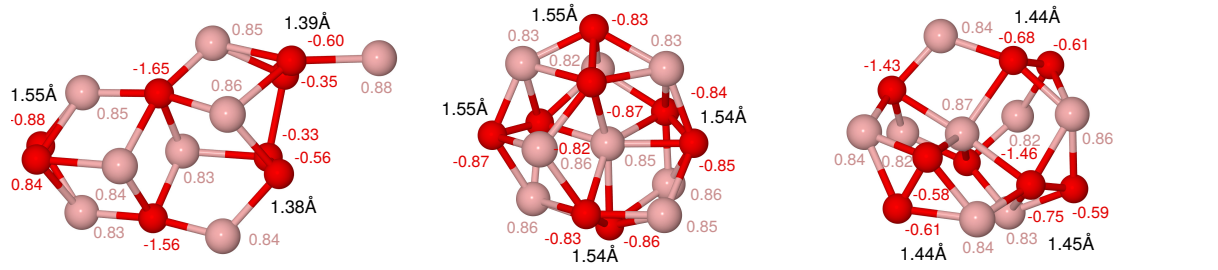

singlet (spin unrestricted)

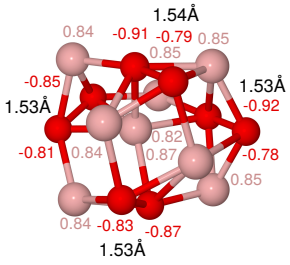

triplet (spin restricted)

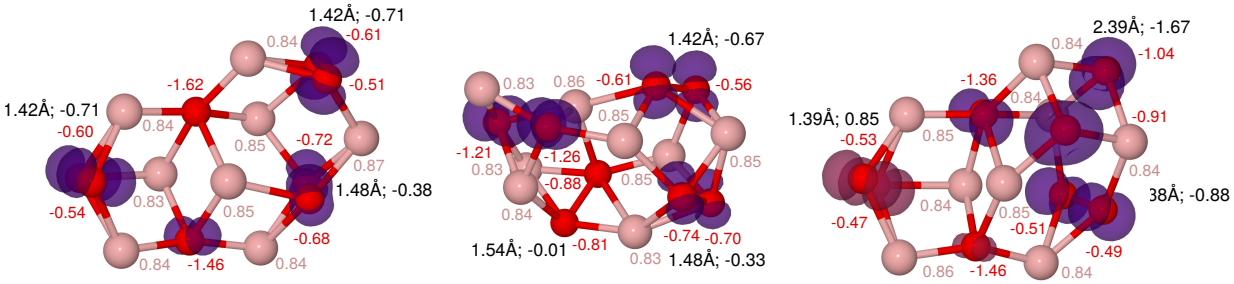

triplet (spin unrestricted)

Figure C.4.: Li_8O_8 clusters in a singlet and a triplet state.

Li_8O_8

(i) **(ii)** **(iii)**

quintet (spin restricted)

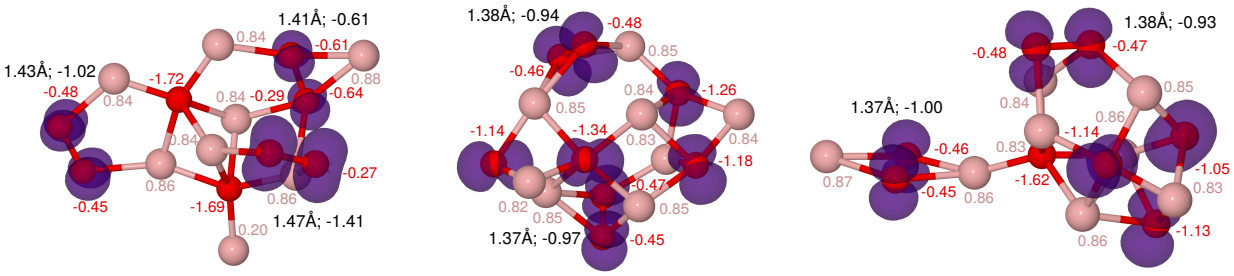

septet (spin restricted)

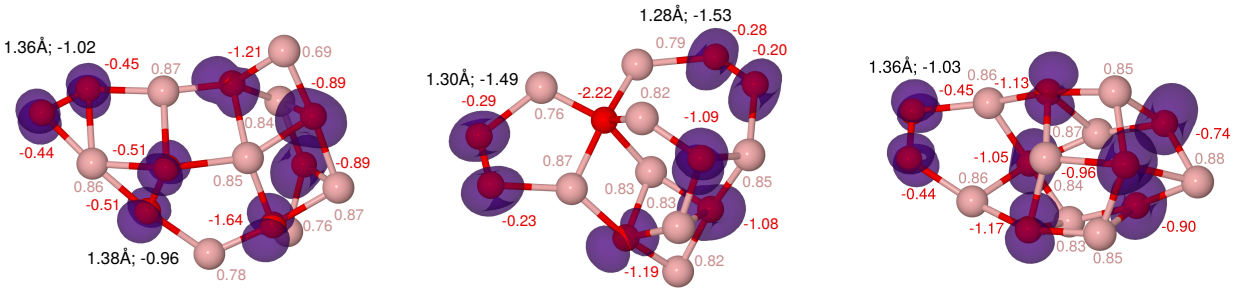

Figure C.5.: Li_8O_8 clusters in a quintet and a septet state.

Li_8O_4

(i) **(ii)** **(iii)**

singlet (spin unrestricted)

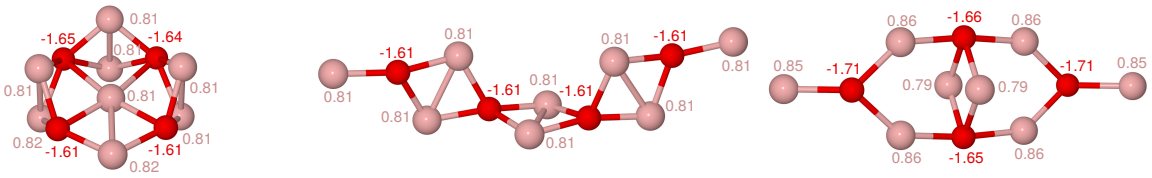

Figure C.6.: Li_8O_4 clusters in a singlet state.

Table C.1.: Cluster energies per Li_2O_2 unit with respect to the lowest energy for the particular Li_nO_n cluster(for singlet (red) and triplet (green) states, respectively). The (i) restricted Li_8O_8 cluster (gray) is not considered in the evaluation of the energy minimum of the peroxide-type clusters, since its structure does not form a closed Li_8O_8 cluster, and is assumed as an artifact of the initial conditions.

Gibbs free energy of formation / eV			
singlet		triplet	
Li_2O_2			
(i) restricted	0.0004	(i) restricted	1.9150
(ii) restricted	0.0012	(ii) restricted	1.9147
(iii) restricted	0.0028	(iii) restricted	0.9050
(i) unrestricted	0.0011		
(ii) unrestricted	0.0153		
(iii) unrestricted	0.0000		
Li_4O_4			
(i) restricted	0.0000	(i) restricted	0.1283
(ii) restricted	0.0698	(ii) restricted	0.6930
(iii) restricted	0.0002	(iii) restricted	0.0637
(i) unrestricted	0.0035	(iii) unrestricted	0.0840
(ii) unrestricted	0.0885		
Li_6O_6			
(i) restricted	0.2570	(i) restricted	0.2177
(ii) restricted	0.2645	(ii) restricted	0.2155
(iii) restricted	0.4711	(iii) restricted	0.5016
(i) unrestricted	0.2641	(iii) unrestricted	0.0000
(ii) unrestricted	0.2752		
Li_8O_8			
(i) restricted	0.0035	(i) restricted	0.0140
(ii) restricted	0.2085	(ii) restricted	0.1431
(iii) restricted	0.2878	(iii) restricted	0.3557
(ii) unrestricted	0.3049	(i) unrestricted	0.0000
		(iii) unrestricted	0.0140
quintet		septet	
(i) restricted	0.5263	(i) restricted	1.0371
(ii) restricted	0.2932	(ii) restricted	0.9341
(iii) restricted	0.2137	(iii) restricted	0.9341

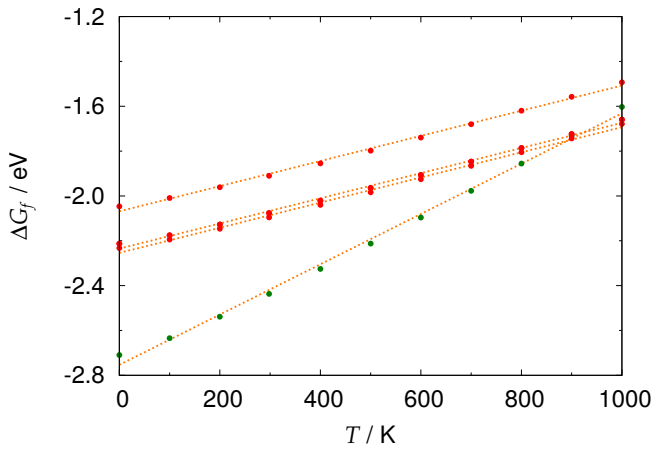

Table C.2.: Cluster energies of the Li_8O_4 clusters per Li atom with respect to the lowest energy for the Li_8O_8 clusters at 298 K.

Gibbs free energy of formation / eV Li_8O_4	
(i) unrestricted	0.5266
(ii) unrestricted	0.3410
(iii) unrestricted	0.3601

Figure C.7.: Gibbs free energy of formation per Li atom as a function of temperature for Li_8O_4 (red) and Li_8O_8 (green) clusters, and best-fit lines of the linear regression in orange (correlation coefficient is $r = 0.9984$).

APPENDIX D

BADER CHARGE DIFFERENCES

Table D.1.: Bader charge difference between the initial clusters before removal of electrons and the clusters after removal of electrons and an electron minimization (min.) and between the initial clusters before removal of electrons and the final clusters after removal of electrons and a MD simulation (MD) in vacuum and in DMSO.

	$\Delta q_{\text{-1e}^-}$ / e		$\Delta q_{\text{-2e}^-}$ / e		
	min.	MD	min.	MD	
in vacuum					
Li_8O_8	1.0000	1.0000	2.0001	1.9999	
O1−O2	0.2274	0.2420	0.4645	1.1701	
O3	0.0740	0.0144	0.1698	-0.0517	
O4	0.1540	0.0904	0.3164	-0.2771	
O5−O6	0.2229	0.4856	0.4321	0.5414	
O7−O8	0.2645	0.0371	0.4938	0.2205	
sum(oxygens)	0.9428	0.8879	1.8766	1.8312	
in DMSO					
DMSO	0.3829	0.3599	1.0808	0.3731	0.3660
Li_8O_8	0.6171	0.6479	0.9186	1.6261	1.6340
O1−O2	0.1714	0.2408	0.2190	0.3666	0.7016
O3	0.0633	-0.0029	0.0954	-0.0321	-0.0230
O4	0.1128	0.0825	0.1531	-0.0153	-0.0940
O5−O6	0.1723	0.2281	0.2195	0.6197	0.6988
O7−O8	0.1517	0.2731	0.1973	0.7163	0.3680
sum(oxygens)	0.5916	0.6404	0.8843	1.6552	1.6514

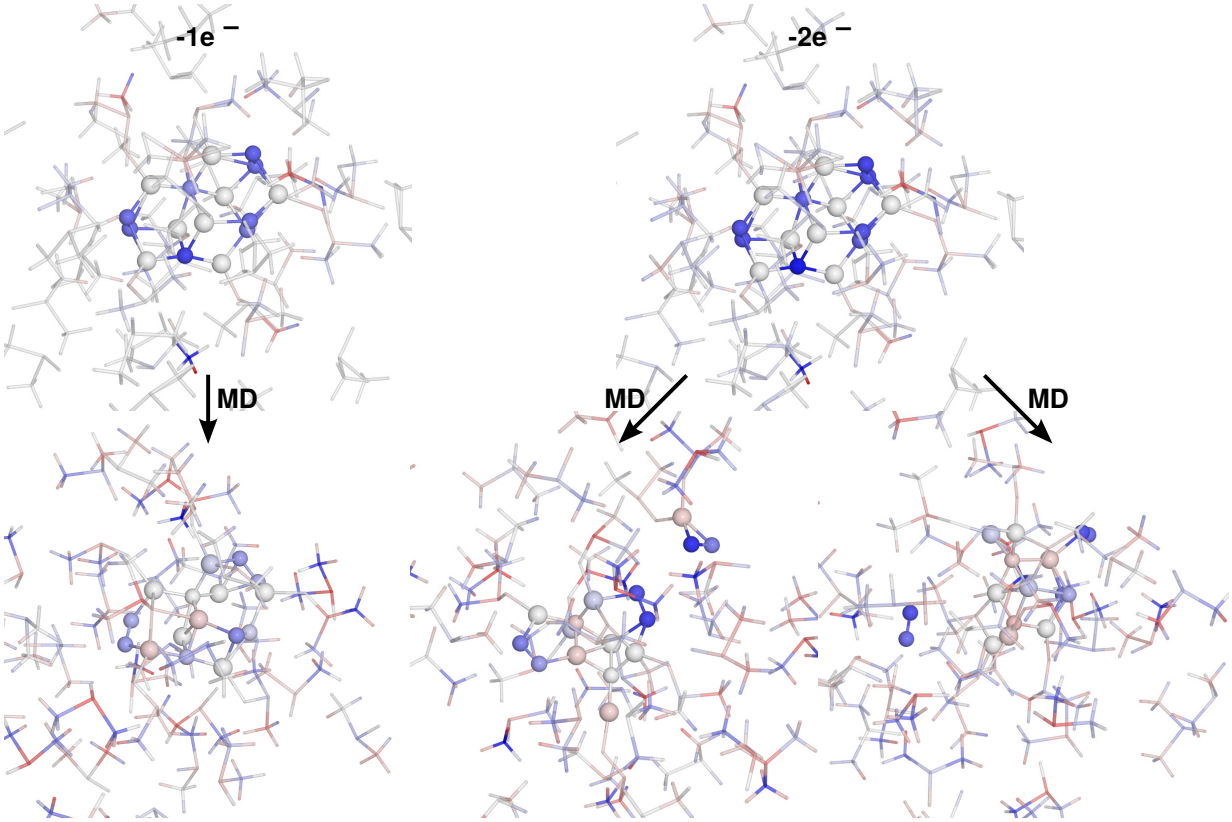

Figure D.1.: Visualization of the charge differences upon removal of electrons from negative (red) values to positive (blue) values in DMSO.

APPENDIX E

DENSITIES OF STATES

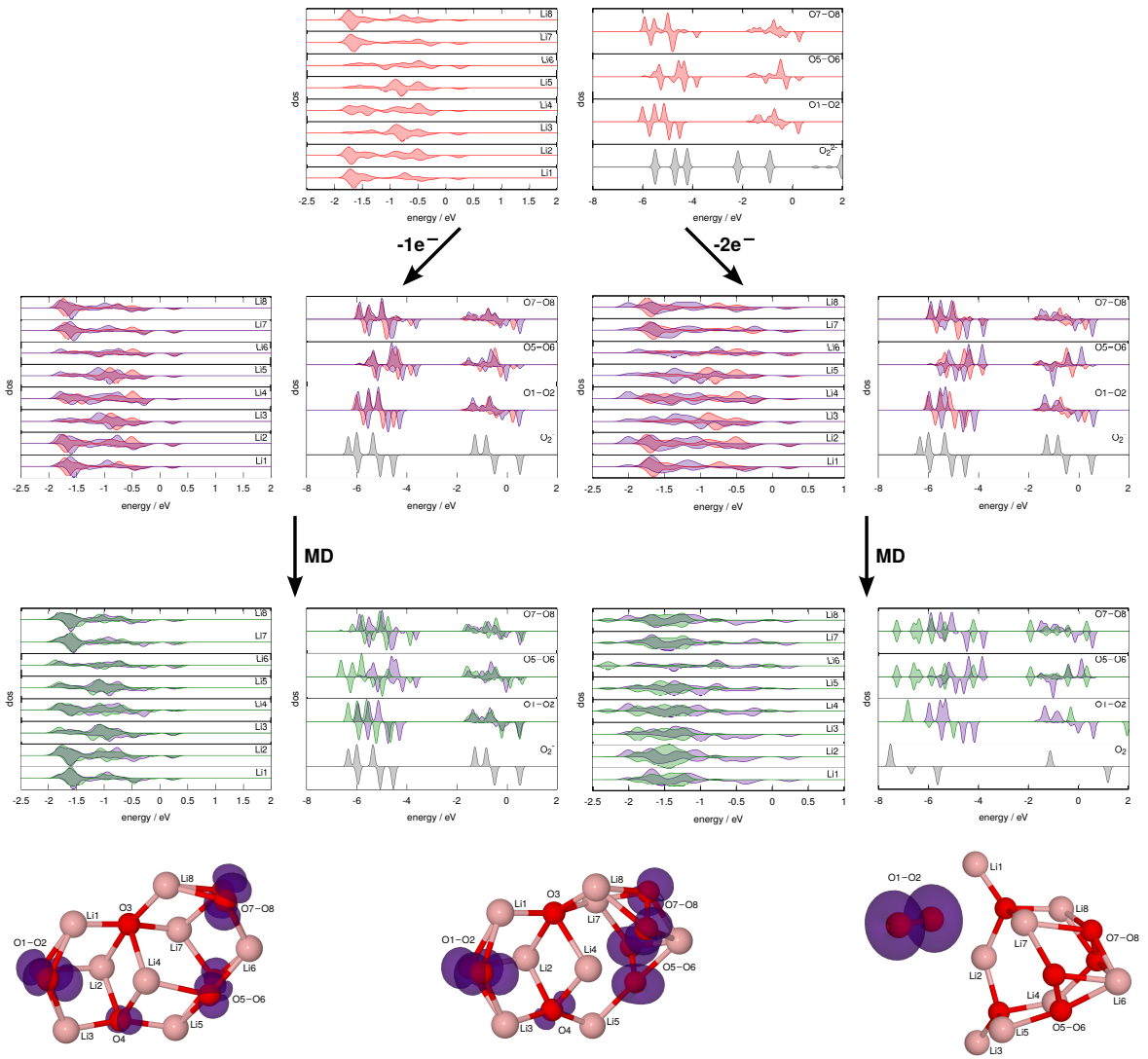

Figure E.1.: DOS for Li^+ and $O-O$ pairs in vacuo before removal of electrons (red), after removal of electrons and an electron minimization (purple), and after a MD simulation (green). The initial and final clusters with corresponding atom numbers are shown below the DOS. For comparison, the DOS of the spinpaired O_2^{2-} ion of a Li_2O_2 molecule, the O_2^- ion of a LiO_2 molecule, and the O_2 molecule are shown in gray.

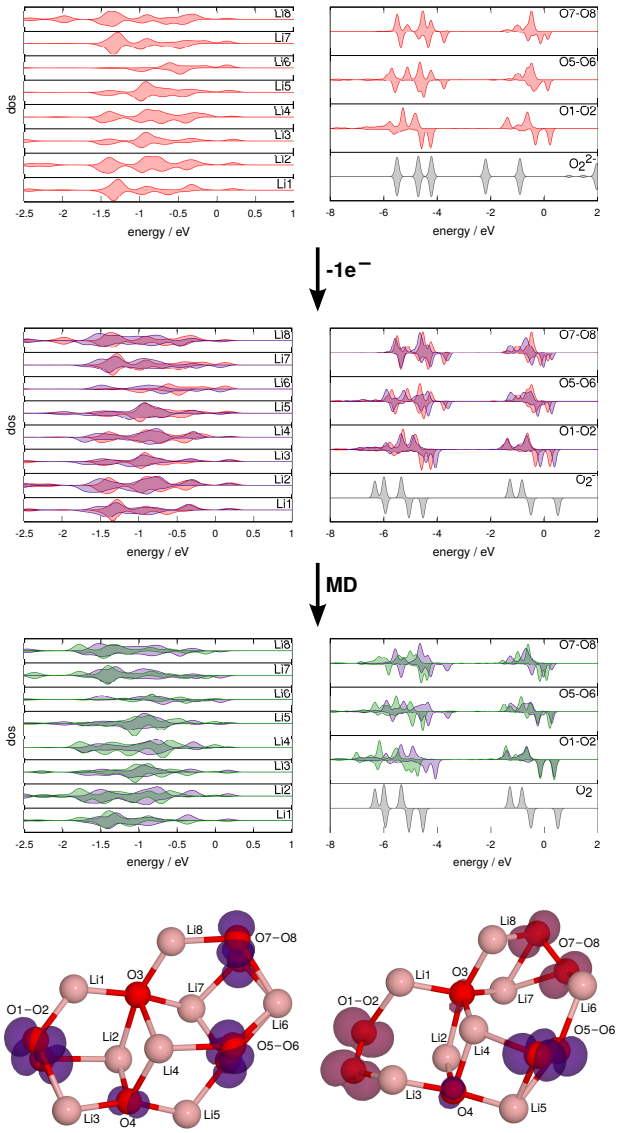

Figure E.2.: DOS for Li^+ and O−O pairs in DMSO, before removal of electrons (red), after removal of one electron and an electron minimization (purple), and after a MD simulation (green). The initial and the final cluster with corresponding atom number are shown below the DOS. For comparison, the DOS of the spinpaired O_2^{2-} ion of a Li_2O_2 molecule and the O_2^- ion of a LiO_2 molecule are shown in gray.

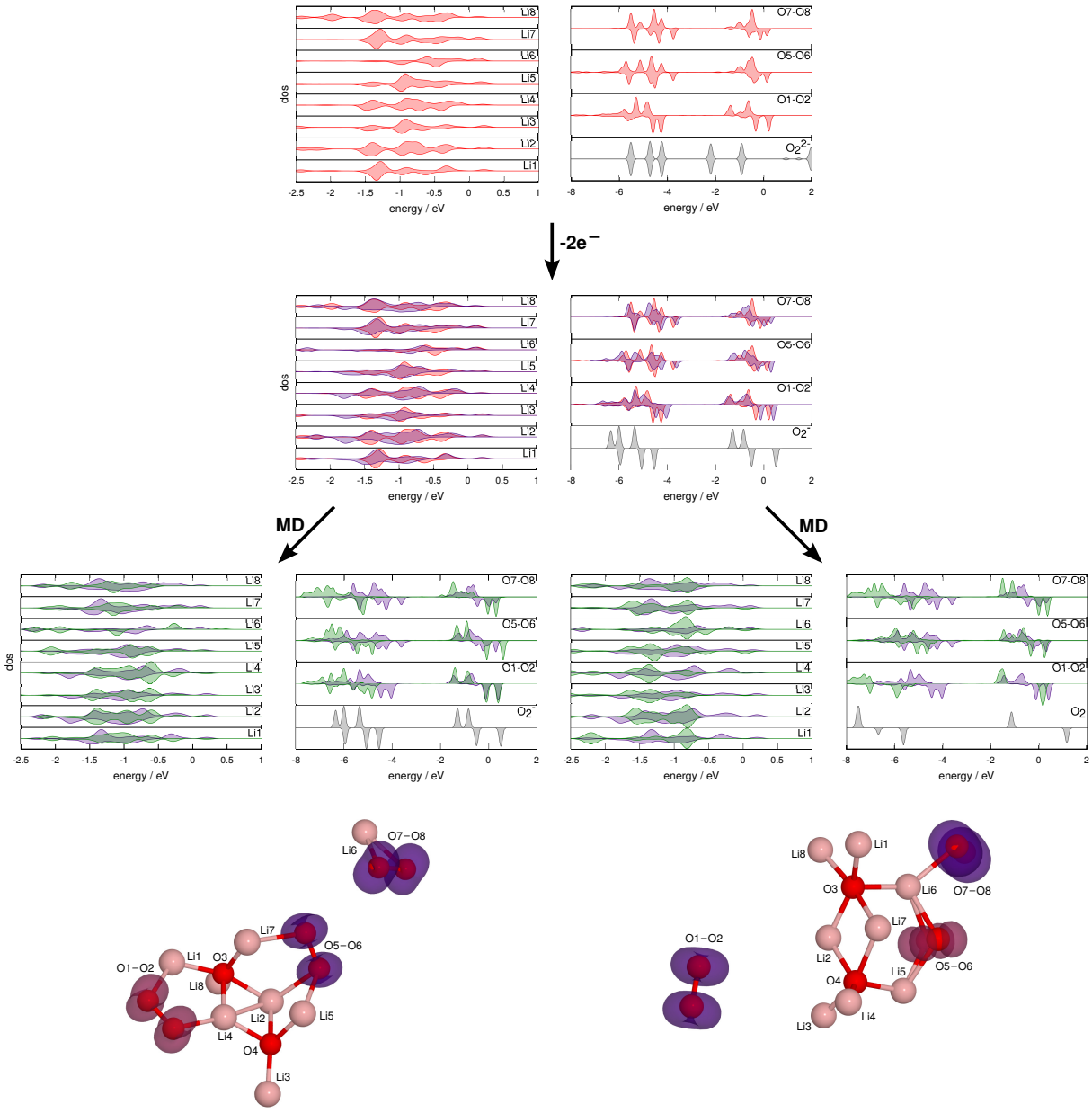

Figure E.3.: DOS for Li^+ and $O-O$ pairs in DMSO, before removal of electrons (red), after removal of two electrons and an electron minimization (purple), and after a MD simulation (green). The initial and both final clusters with corresponding atom number are shown below the DOS. For comparison, the DOS of the spinpaired O_2^{2-} ion of a Li_2O_2 molecule, the O_2^- ion of a LiO_2 molecule, and the O_2 molecule are shown in gray.

APPENDIX F

MATHEMATICAL THEOREMS AND DEFINITIONS

Definition F.1. *Matrix $A = (a_{ij}) \in \mathbb{C}^{n\times n}$ is called hermitian if*

$$a_{ij} = \bar{a}_{ji} \quad \textit{or} \quad A^T = \bar{A}\ .$$

[151]

Definition F.2. *Matrix $A = (a_{ij}) \in \mathbb{C}^{n\times n}$ is called unitary if*

$$A^* = \bar{A}^T = A^{-1}\ .$$

[151]

Theorem F.1. (Spectral theorem) *For every hermitian matrix A there is an orthonormal basis on $(\mathbb{C}^n, \langle\cdot,\cdot\rangle_{\mathbb{C}})$ which is composed solely of eigenvectors of A. In particular, there exists a unitary matrix U (Definition F.2) such that $\bar{U}\cdot A\cdot U$ has diagonal form.[152]*

Proof. See ref. 152. □

Definition F.3. *Let V be a $\mathbb{K}$-vector space, where $\mathbb{K} \in \{\mathbb{R}, \mathbb{C}\}$. A functional F is a mapping of the form $F\colon V \to \mathbb{K}$ such that $f \mapsto F[f]$.*
Usually $V = \{f(x)|x \in \mathbb{K}\}$ is referred to a function space.[153]

Definition F.4. *Let F be a functional as defined in F.3, then the functional derivative $\frac{\delta F[f]}{\delta f(x)}$ is defined as the function which fulfills*

$$\delta F[f] = \int \frac{\delta F[f]}{\delta f(x)}\delta f(x)\mathrm{d}x = \lim_{\epsilon\to 0}\frac{F[f+\delta f]-F[f]}{\epsilon}\ ,$$

where δf is the variation of the function f.[153]

Definition F.5. (Landau notation) *Let $f, g\colon \mathbb{R} \to \mathbb{R}$ be two functions, one writes*

- $f = \mathcal{O}(g)$ *if there are a constant $C > 0$ and a neighborhood $U = U(x_0)$ of x_0 such that $|f(x)| < C|g(x)|$ for all $x \in U$*
- $f = o(g)$ *if for every constant $\epsilon > 0$ there is a neighborhood $U = U(x_0)$ of x_0 such that $|f(x)| < \epsilon|g(x)|$ for all $x \in U$.*

[154]

Theorem F.2. (Taylor series) *Let $u : I \to \mathbb{R}$ be an $(n+1)$ times continuously differentiable function and $a \in I$, one writes for all $x \in I$*

$$u(x) = u(a) + \frac{u'(a)}{1!}(x-a) + \frac{u''(a)}{2!}(x-a)^2 + \cdots + \frac{u^n(a)}{n!}(x-a)^n + R_{n+1}(x)$$

and for the remainder

$$R_{n+1} = \frac{1}{n!}\int_a^x (x-t)^n u^{(n+1)}(t)\mathrm{d}t \ .$$

[155]

Proof. Proof by mathematical induction with respect to n.[155] □

Corollary F.1. (Lagrange form of the remainder) *The remainder in the Lagrange form is stated as*

$$\begin{aligned} u(x) &= \sum_{k=0}^{n} \frac{u^{(k)}(a)}{k!}(x-a)^k + \eta(x)(x-a)^n \\ &= \sum_{k=0}^{n} \frac{u^{(k)}(a)}{k!}(x-a)^k + \mathcal{O}(|x-a|^n) \ , \end{aligned}$$

where $\lim_{x\to a} \eta(x) = 0$.[155]

Proof. Proof by the mean value theorem for integration.[155] □

Definition F.6. *A matrix $A \in \mathbb{R}^{n\times n}$ is called*

(i) *L_0-matrix if $a_{ij} \leq 0 \ \forall \ i \neq j$*

(ii) *inverse monotone if there exists A^{-1} and $A^{-1} \geq 0$*

(iii) *M-matrix if the matrix is an inverse monotone L_0-matrix .*

[117]

Definition F.7. (Row-sum norm) *The row-sum norm of a matrix $A \in \mathbb{R}^{n\times n}$ is a matrix norm (derived from the max norm) stated as*

$$\|A\|_\infty = \max_{i=1,\dots,n} \sum_{j=1}^{n} |a_{ij}| \ .$$

[154]

Theorem F.3. *Let $A \in \mathbb{R}^{n\times n}$ be a strictly diagonally dominant matrix, i. e., $|a_{ii}| > \sum\limits_{\substack{j=1\\ j\neq i}}^{n} |a_{ij}|$ for $i = 1, \dots, n$, then A is invertible.*

Proof. Suppose that A is singular, this means $\exists\, \mathbb{R}^n \ni x \neq 0$ such that $Ax = 0$. Choose i_0 such that $|x_{i_0}| = \max\limits_i |x_i|$, consequently $|x_{i_0}| > 0$ (since $x \neq 0$). It follows from $Ax = 0$

$$\sum_{j=1}^{n} a_{i_0 j} x_j = 0 \quad \Leftrightarrow \quad a_{i_0 i_0} x_{i_0} = -\sum_{\substack{j=1\\ j\neq i_0}}^{n} a_{i_0 j} x_j$$

and hence

$$|a_{i_0 i_0}||x_{i_0}| \leq \Big| \sum_{\substack{j=1\\ j\neq i_0}}^{n} a_{i_0 j} x_j \Big| \leq \sum_{\substack{j=1\\ j\neq i_0}}^{n} |a_{i_0 j}||x_j| \underset{\text{choice of } i_0}{\leq} \sum_{\substack{j=1\\ j\neq i_0}}^{n} |a_{i_0 j}||x_{i_0}| \underset{\substack{\text{strictly}\\ \text{diagonally}\\ \text{dominant}}}{<} |a_{i_0 i_0}||x_{i_0}| \qquad \lightning$$

$\Rightarrow A$ is invertible.

□

Theorem F.4. (M-criterion) *Let $A \in \mathbb{R}^{n\times n}$ be a L_0-matrix, then A inverse monotone if and only if there exists a vector $\boldsymbol{e} \in \mathbb{R}^n$ and $\boldsymbol{e} > 0$ such that $A\boldsymbol{e} > 0$. Furthermore, using the row-sum norm in Definition F.7, we obtain the estimate*

$$\|A^{-1}\|_\infty \leq \frac{\|\boldsymbol{e}\|_\infty}{\min\limits_i (A\boldsymbol{e})_i} \ .$$

[117]

Proof. See ref. 117. □

Definition F.8. *Let E be a finite set and $U \subseteq \mathcal{B}(E)$ a family of subsets of E. The pair $M = (E, U)$ is called matroid, if following properties are fulfilled:*

(i) $\emptyset \in U$

(ii) $A \in U, A' \subseteq A \Rightarrow A' \in U$

(iii) $A, A' \in U, |A'| = |A| + 1 \Rightarrow \exists\, a \in A' \setminus A$ *such that* $A \cup \{a\} \in U$,

where $|\cdot|$ denotes the cardinality of a set.[118]

Definition F.9. (Trapezoidal rule) *The trapezoidal rule is an approximation of the integral*

$$\int_a^b f(x)\mathrm{d}x \approx Q(f)$$

by a Newton-Cotes formula $Q\colon \mathbb{R}^{[a,b]} \to \mathbb{R}$ regarding $x_0, \ldots, x_n \in [a, b]$ stated as

$$Q(f) = h\left(\frac{f(x_0) + f(x_n)}{2} + \sum_{i=1}^{n-1} f(x_i)\right) ,$$

where the grid spacing of the interval $[a, b]$ in n subintervals of length $h := \frac{b-a}{n}$ and the approximation of the integral of f in every subinterval $[x_i, x_{i+1}]$ is given by a trapezoid with vertices $(x_i, 0)$, $(x_{i+1}, 0)$, $(x_{i+1}, f(x_{i+1}))$ and $(x_i, f(x_i))$ for $i = 0, \ldots, n-1$.[154]

APPENDIX G

PROOF OF CONSISTENCY AND STABILITY OF THE APPLIED METHODS

Proof. (Consistency)
(i) Via the Taylor series (Theorem F.2) or the Lagrange remainder (Corollary F.1) we can write the differential operator in equation $\partial_t u = g$ as

$$\frac{u_j^{n+1} - u_j^n}{\Delta t} = \partial_t u|_{G_\Delta} + \mathcal{O}(\Delta t)$$

restricted on the grid $G_\Delta = \{(j \cdot \Delta x, n \cdot \Delta t) \mid n \in \{0, \dots, N\}, j \in \{0, \dots, J\}\}$, thus follows

$$\left\| D_n^+ u_j^n - \partial_t u|_{G_\Delta} \right\|_\infty = \mathcal{O}(\Delta t) \ .$$

(ii) For the partial differential equation $\partial_{xx} u + d\partial_x u - \partial_t u + fu = 0$ we analyze the differential operators separately and apply analogously to **(i)** the corollary of the Lagrange remainder

$$\begin{aligned}
\frac{u_j^{n+1} - u_j^n}{\Delta t} &= \partial_t u|_{G_\Delta} + \frac{1}{2}\Delta t \cdot \partial_{tt} u|_{G_\Delta} + \mathcal{O}\big((\Delta t)^2\big) \\
\frac{u_{j+1}^n - u_j^n}{\Delta x} &= \partial_x u|_{G_\Delta} + \mathcal{O}(\Delta x) \\
\frac{1}{\Delta x}\frac{u_{j+1}^{n+1} - u_{j+1}^n}{\Delta t} - \frac{1}{\Delta x}\frac{u_j^{n+1} - u_j^n}{\Delta t} &= \partial_{xt} u|_{G_\Delta} + \mathcal{O}(\Delta x + \Delta t) \ .
\end{aligned}$$

Hence the finite differences for the explicit and the implicit method can be written as

$$\sigma\frac{u_{j+1}^{n+1} - u_j^{n+1}}{\Delta x} + (1-\sigma)\frac{u_{j+1}^n - u_j^n}{\Delta x} = \partial_x u|_{G_\Delta} + \sigma\Delta t \cdot \partial_{xt} u|_{G_\Delta} + \mathcal{O}\big(\Delta x + (\Delta t)^2\big)$$

and

$$\begin{aligned}&\sigma\frac{u_{j-1}^{n+1}-2u_j^{n+1}+u_{j+1}^{n+1}}{(\Delta x)^2}+(1-\sigma)\frac{u_{j-1}^{n}-2u_j^{n}+u_{j+1}^{n}}{(\Delta x)^2}\\ =\;&\partial_{xx}u|_{G_\Delta}+\sigma\Delta t\cdot\partial_{xxt}u|_{G_\Delta}+\mathcal{O}\big((\Delta x)^2+(\Delta t)^2\big)\;.\end{aligned}$$

For the last term fu in the particular case of the Crank-Nicolson method we choose

$$u_j^{n+\frac{1}{2}}=u|_{G_\Delta}+\frac{1}{2}\Delta t\partial_t u|_{G_\Delta}+\mathcal{O}\big((\Delta t)^2\big)\;.$$

In summary, the resulting order of consistency is

$$\begin{aligned}&\big\|L_\Delta(u|_{G_\Delta})-(Lu)|_{G_\Delta}\big\|_\infty\\ =\;&\Big\|\sigma\Delta t\cdot\partial_t(\underbrace{\partial_{xx}+d\partial_x}_{=-e\partial_t-f})u|_{G_\Delta}+\frac{1}{2}\Delta te\partial_{tt}u|_{G_\Delta}+\frac{1}{2}\Delta tf\partial_t u|_{G_\Delta}\Big\|_\infty+\mathcal{O}\big(\Delta x+(\Delta t)^2\big)\\ =\;&\Big\|\Big(\sigma-\frac{1}{2}\Big)\Delta t(-e\partial_{tt}-f\partial_t)u|_{G_\Delta}\Big\|_\infty+\mathcal{O}\big(\Delta x+(\Delta t)^2\big)\\ =\;&\mathcal{O}\big(\Delta x+\Delta t\big)\end{aligned}$$

for all $\sigma\in[0,1]$ und $\sigma\neq\frac{1}{2}$. Only for the Crank-Nicolson method for $\sigma=\frac{1}{2}$ the order of consistency is

$$\big\|L_\Delta(u|_{G_\Delta})-(Lu)|_{G_\Delta}\big\|_\infty=\mathcal{O}\big(\Delta x+(\Delta t)^2\big)\;.$$

□

Remark. *Although $u\in C^{4,3}$ is assumed in the above proof, this assumption is solely necessary for the Crank-Nicolson method and can be reduced in all other cases.*

Proof. (Stability) W.l.o.g. we assume homogeneous Dirichlet boundary conditions (see remark). **(i)** The approximation in equation (8.23) in the discrete formulation $u_j^{n+1}=u_j^n+\Delta t g_j^n$ is estimated by

$$\max_j|u_j^{n+1}|\leq\max_j|u_j^n|+\Delta t\max_j|g_j^n|$$

for every time step n. Is the inequality carried on iteratively, we receive

$$\max_{j,n}|u_j^{n+1}|\leq\max_j|u_j^0|+\Delta t\sum_{k=0}^{n}\max_j|g_j^k|\;.$$

Using the number of time steps N and $u_j^0 \to u(x,0)$ for $\Delta t, \Delta x \to 0$ we obtain in particular

$$\max_{j,n} |u_j^n| \leq \max |u(x,0)| + \Delta t \sum_{k=0}^{n-1} \max_j |g_j^k| \leq \max |u(x,0)| + t_N \max_{j,n} |g_j^n| \ .$$

Thus the solution of the problem can be estimated using the initial values and the right-hand side independent of the discretization, hence the approximation is stable.
(ii) In the second case we follow a similar procedure. The approximation in equation (8.24)

$$\begin{aligned} 0 =& D_j^+ D_j^- \left(\sigma u_j^{n+1} + (1-\sigma) u_j^n\right) + d_j^n D_j^+ \left(\sigma u_j^{n+1} + (1-\sigma) u_j^n\right) + e_j^n D_n^+ u_j^n + f_j^n u_j^n \\ =& \frac{\sigma}{(\Delta x)^2} \left(u_{j-1}^{n+1} - 2u_j^{n+1} + u_{j+1}^{n+1}\right) + \frac{1-\sigma}{(\Delta x)^2} \left(u_{j-1}^n - 2u_j^n + u_{j+1}^n\right) \\ &+ \frac{\sigma \cdot d_j^n}{\Delta x} \left(u_{j+1}^{n+1} - u_j^{n+1}\right) + \frac{(1-\sigma) \cdot d_j^n}{\Delta x} \left(u_{j+1}^n - u_j^n\right) \\ &+ \frac{e_j^n}{\Delta t} \left(u_j^{n+1} - u_j^n\right) + f_j^n u_j^n \end{aligned}$$

is written as

$$\begin{aligned} & -\theta\sigma u_{j-1}^{n+1} + \left[-e_j^n + \theta\sigma(2 + d_j^n \Delta x)\right] u_j^{n+1} - \theta\sigma(1 + d_j^n \Delta x) u_{j+1}^{n+1} \\ =& \theta(1-\sigma) u_{j-1}^n + \left[-e_j^n - \theta(1-\sigma)(2 + d_j^n \Delta x) + f_j^n \Delta t\right] u_j^n + \theta(1-\sigma)(1 + d_j^n \Delta x) u_{j+1}^n \ , \end{aligned}$$

where $\theta = \frac{\Delta t}{(\Delta x)^2}$. In a condensed form using homogeneous Dirichlet boundary conditions the resulting solution scheme is

$$A\boldsymbol{u}^{n+1} = B\boldsymbol{u}^n \ ,$$

where the vector are stated as

$$\boldsymbol{u}^{n+1} = (u_1^{n+1}, \ldots, u_J^{n+1})^T \quad \text{und} \quad \boldsymbol{u}^n = (u_1^n, \ldots, u_J^n)^T \ .$$

Both matrices A and B are tridiagonal matrices and the matrix entries are given by

$$\begin{cases} a_{ii} = -e_j^n + \theta\sigma(2 + d_i^n \Delta x) & \text{for } i = 1, \ldots, J-1 \\ a_{ii+1} = -\theta\sigma(1 + d_i^n \Delta x) & \text{for } i = 1, \ldots, J-1 \\ a_{ii-1} = -\theta\sigma, & \text{for } i = 2, \ldots, J-1 \\ a_{JJ} = -e_j^n + \theta\sigma \end{cases}$$

and

$$\begin{cases} b_{ii} = -e_j^n - \theta(1-\sigma)(2 + d_i^n \Delta x) + f_i^n \Delta t & \text{for } i = 1, \ldots, J-1 \\ b_{ii+1} = \theta(1-\sigma)(1 + d_i^n \Delta x) & \text{for } i = 1, \ldots, J-1 \\ b_{ii-1} = \theta(1-\sigma), & \text{for } i = 2, \ldots, J-1 \\ b_{JJ} = -e_j^n - \theta(1-\sigma) + f_J^n \Delta t \end{cases}$$

The last entries $j = J$ are modified according to the applied Neumann boundary conditions and is illuminated in detail in Chapter 9. In the next step using the M-criterion F.4 we estimate the matrix A. Following assumption **(a)**, we conclude $1 + d_j^n \Delta x \geq 0$ and hence $a_{ij} \leq 0$ for $i \neq j$, i. e., A is an L_0-matrix. Furthermore, the matrix is strictly diagonally dominant for assumption **(b)**, since

$$|a_{ii}| = -e_i^n + \theta\sigma(2 + d_i^n \Delta x) > \theta\sigma(2 + d_i^n \Delta x) = \sum_{\substack{j=1 \\ j \neq i}}^{J} |a_{ij}| \quad \text{for} \quad i = 2, \ldots, J-1$$

and

$$|a_{11}| = -e_1^n + \theta\sigma(2 + d_1^n \Delta x) > \theta\sigma(1 + d_1^n \Delta x) = \sum_{\substack{j=1 \\ j \neq 1}}^{J} |a_{1j}|,$$

$$|a_{JJ}| = -e_J^n + \theta\sigma > \theta\sigma = \sum_{\substack{j=1 \\ j \neq J}}^{J} |a_{Jj}| \, .$$

Thus, A is regular according to Theorem F.3. Using the M-criterion in Theorem F.4 anew and the vector $\boldsymbol{e} = (1, \ldots, 1)^T > 0$ such that

$$(A\boldsymbol{e})_i = \left\{ \begin{array}{ll} -e_j^n & \text{for } i = 2, \ldots, J \\ -e_j^n + \underbrace{\theta\sigma}_{\geq 0} & \text{for } i = 1 \end{array} \right\} > 0$$

we identify A as an M-matrix and the inverse is

$$\|A^{-1}\|_\infty \leq \frac{\|\boldsymbol{e}\|_\infty}{\min\limits_i (A\boldsymbol{e})_i} \leq 1 \, . \tag{G.1}$$

Finally, we need the estimation of matrix B. Since $\theta > 0$ and $0 \leq \sigma \leq 1$, the super- and subdiagonal are positive according to assumption **(a)** and so is the main diagonal according to **(d)**

and we can state

$$\begin{aligned}\|B\|_\infty &= \max_i \sum_{j=1}^{n} |b_{ij}| = \max_i \left\{ \begin{array}{ll} |-e_j^n + f_i^n \Delta t| & \text{for } i = 2,\dots,J \\ |-e_j^n - \underbrace{\theta(1-\sigma)}_{\geq 0} + f_i^n \Delta t| & \text{for } i = 1 \end{array} \right\} \\ &= |-e_j^n + f_i^n \Delta t| \leq 1 \,. \end{aligned} \tag{G.2}$$

The estimation in the last step is based on the assumptions **(c)** and **(d)**. In summery, we obtain for the estimation of the solution $\boldsymbol{u}^{n+1}$

$$\begin{aligned}\|\boldsymbol{u}^{n+1}\|_\infty &= \|A^{-1}A\boldsymbol{u}^{n+1}\|_\infty \leq \|A^{-1}\|_\infty \|A\boldsymbol{u}^{n+1}\|_\infty \\ &\underset{\text{eq. (G.1)}}{\leq} \|B\boldsymbol{u}^n\|_\infty \leq \|B\|_\infty \|\boldsymbol{u}^n\|_\infty \\ &\underset{\text{eq. (G.2)}}{\leq} \|\boldsymbol{u}^n\|_\infty \,, \end{aligned}$$

thus the solution of the problem can be estimated using the initial values and the right-hand side independent of the discretization as in **(i)**, hence the approximation is stable. □

Remark. *W.l.o.g. we are allowed to assume Dirichlet boundary conditions, since inhomogeneous boundary conditions can be transformed in homogeneous ones. Let $Lu = g$ on Ω, where $u : \Omega \to \mathbb{R}$ and L is a linear differential operator, and $u = u_0 \neq 0$ on the boundary $\partial\Omega$. We construct a function $\bar{u} : \Omega \to \mathbb{R}$, where $\bar{u} = u_0$ on $\partial\Omega$ and $\bar{u}$ sufficiently smooth. In that case the homogeneous problem is written as*

$$Lv = \bar{g} \;\; \text{on} \;\; \Omega \quad \text{and} \quad v = 0 \;\; \text{on} \;\; \partial\Omega \,,$$

where $v = u - \bar{u}$. Furthermore, $u = v + \bar{u}$ is a solver of the original problem, since

$$Lu = L(v + \bar{u}) = Lv + L\bar{u} = \bar{g} + L\bar{u} = g - L\bar{u} + L\bar{u} = g \;\; \text{on} \;\; \Omega$$

and

$$u = v + \bar{u} = 0 + u_0 \;\; \text{on} \;\; \partial\Omega \,.$$

Erklärung

Hiermit erkläre ich, dass ich

1. die Arbeit ohne unerlaubte fremde Hilfe angefertigt habe,
2. keine anderen als die von mir angegebenen Quellen und Hilfsmittel benutzt habe und
3. die den benutzten Werken wörtlich oder inhaltlich entnommenen Stellen als solche kenntlich gemacht habe.

Bremen, 15.05.2016

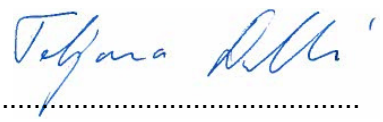

.....

Tatjana Dabrowski